T.C.
BİNGOL UNIVERSITY
INSTITUTE OF SCIENCE

SYNTHESIS OF NEW HYDRAZIDE-BASED PHENOLPHTHALEIN AND RHODAMINE B DERIVATIVES AND INVESTIGATION OF THEIR PHOTOPHYSICAL PROPERTIES

PhD THESIS

Abdullah Saleh Hussein

HUSSEIN

CHEMISTRY DEPARTMENT

SUPERVISOR
Prof. Dr. Mahmut TOPRAK

2nd SUPERVISOR
Assoc. Prof. Dr. Sinan BAYINDIR

BİNGÖL–2024

REPUBLIC OF TURKEY
BİNGÖL UNIVERSITY
INSTITUTE OF SCIENCE

SYNTHESIS OF NEW HYDRAZIDE-BASED PHENOLPHTHALEIN AND RHODAMINE B DERIVATIVES AND INVESTIGATION OF THEIR PHOTOPHYSICAL PROPERTIES

This dissertation, created by Abdullah Saleh Hussein HUSSEIN under the supervision of Prof. Dr. Mahmut TOPRAK and 2nd supervision of Assoc. Prof. Dr. Sinan BAYINDIR was accepted as a PhD thesis in the Department of Chemistry by the following committee on 22/07/2024 with the vote unity.

Head of examining committee:	Prof. Dr. Ahmet ÇETİN	Signature*:*
Member	: Prof. Dr. Ebru BOZKURT	*Signature* :
Member	: Prof. Dr. Mahmut TOPRAK	*Signature* :
Member	: Assoc. Prof. Dr. Ece A. ŞAHİN	*Signature* :
Member	: Asst. Prof. Dr. Ferruh LAFZİ	*Signature* :

This result has been approved on .... / …… /........ with the decision of ………. /………… by Board of Directors of the Science Institute.

Prof. Dr. Zafer ŞİAR
Director of the institute

This study was supported within the scope of Bingöl University Scientific Research Coordination Unit (BÜBAP).
Project No: BAP-FEF.2023.001

FOREWORD

I would like to express my heartfelt gratitude to my thesis advisors Prof. Dr. Mahmut TOPRAK and Assoc. Prof. Dr. Sinan BAYINDIR, for their academic guidance and contributions to my development through valuable discussions during my thesis research.

I also thank the Bingöl University Research Projects Coordination Unit (BÜBAP) for supporting this thesis work (BAP–FEF.2023.001).

I am grateful to Asst. Prof. Dr. Ferruh LAFZİ for his scientific support during the thesis study. Additionally, I would like to thank all the faculty members of the Department of Chemistry at Bingöl University and Assoc. Prof. Dr. Haydar KILIÇ.

Finally, I express my heartfelt thanks to my family, who supported me under all circumstances, and especially to my dear spouse and children, who brought happiness and positive energy into my life.

Abdullah Saleh Hussein HUSSEIN
Bingöl 2024

CONTENTS

LIST OF SYMBOLS AND ABBREVIATIONS

^{13}C HNR	: Carbon-13 Nuclear Magnetic Resonance
^{1}H HMR	: Proton nuclear magnetic resonance (proton NMR, hydrogen-1)
AIE	: aggregation-induced emission
bd	: Broad doublet
bs	: Broad singlet
d	: Doublet
DCM	: Dichloromethane
DFT	: Density Functional Theory
DMF	: Dimethylformamide
DMSO	: Dimethyl sulfoxide
EDTA	: Ethylenediaminetetraacetic acid
EPA	: Environmental Protection Agency
FT-IR	: Fourier Transform Infrared Spectroscopy (cm^{-1})
HEPES	: 4-(2-Hydroxyethyl) piperazine-1-ethane-sulfonic
HMTA	: Hexamethylenetetramine
HMTA	: Hexamethylenetetramine
HOMO	: Highest Occupied Molecular Orbital
Hz	: Hertz
ICT	: Intramolecular Charge Transfer
K_a	: Association Constant (Binding constants)
LOD	: Limit of Detection
LOQ	: Limit of Quantification
LUMO	: Lowest Unoccupied Molecular Orbital
m	: Multiplet
MHz	: Megahertz
p	: Pentet
pH	: Acidity number
PP	: Phenolphthalein

ppm : Part per million

q : Quartet

qd : Quasi doublet

QTOF : Quadrupole time-of-flight

RhB : Rhodamine B

RSD : Relative Standard Deviation

s : Singlet

SD : Standard Deviation

t : Triplet

TD-DFT : Time-Dependent Density Functional Theory

TFA : Trifluoroacetic acid

THF : Tetrahydrofuran

TLC : Thin-layer chromatography

TPE : Tetraphenylethene

Tris : 2-Amino-2-(hydroxymethyl) propane-1,3-diol

TSC : Thiosmicarbazide

U.S. EPA : United States Environmental Protection Agency

UV–Vis : Ultraviolet–Visible Spectrophotometry

WHO : World Health Organization

δ : Delta

LIST OF FIGURES

LIST OF TABLES

SYNTHESIS OF NEW HYDRAZIDE-BASED PHENOLPHTHALEIN AND RHODAMINE B DERIVATIVES AND INVESTIGATION OF THEIR PHOTOPHYSICAL PROPERTIES

ABSTRACT

This thesis focused on the synthesis of novel organic probes based on phenolphthalein (PP) and rhodamine B (RhB), evaluating their interactions with various ions. The study employed techniques like colorimetric analysis, UV-vis/fluorescence spectroscopy, FT-IR, mass, and ^{1}H-NMR spectroscopy, along with theoretical calculations, to understand the binding mechanisms. Optimization of conditions (solvent, pH and time) revealed specific ion affinities influenced by these variables. For instance, PP-1 interacted with multiple ions at different pH levels, while PP-2 and PP-3 showed selective responses towards specific ions. Rhodamine-based probes also demonstrated selective ion interactions, particularly in mixing water organic solvents and buffer solutions. Quantitative analysis involved calculating the limit of detection (LOD), limit of quantification (LOQ), and binding constants (K_a) for each probe-ion interaction. These results suggest that probes with LOD values ranging from 23 nM to 554 nM for Al^{3+} could be effective for detecting aluminum in wastewater samples. Similarly, it was determined that the LOD values for other ions changed from 1.01 mM to 334 nM for Hg^{2+}, from 64 nM to 550 nM for Zn^{2+}, and from 15 nM to 551 nM for Cd^{2+}. Additionally, the LOD value of PP-3 for Cu^{2+} was calculated as 1.56 mM. The probes exhibited sensitivity within WHO limits for detecting ions in environmental samples. Additionally, reversibility studies indicated the potential for probe reuse and application in real-world scenarios, including water samples and cigarette smoke. In general, the synthesized probes proved effective for detecting environmental pollutants (Al^{3+}, Hg^{2+}, Cu^{2+}, Cd^{2+}, Zn^{2+}) and the biological agent GSH, showcasing potential for environmental and biological monitoring.

Keywords: Phenolphthalein, rhodamine, sensor, tetraphenylethene, aluminum, cadmium, copper, mercury, zinc.

YENİ HİDRAZİT TEMELLİ FENOLFTALEİN VE RHODAMİN B TÜREVLERİNİN SENTEZİ VE FOTOFİZİKSEL ÖZELLİKLERİNİN ARAŞTIRILMASI

ÖZET

Bu tez çalışmasında, fenolftalein (PP) ve rhodamin B (RhB) bazlı yeni organik problar sentezlendi ve bunların çeşitli iyonlarla etkileşimleri incelenildi. Propların metal iyonları ile etkileşim mekanizmalarını anlamak için kolorimetrik analiz, UV-vis/floresan spektroskopisi, FT-IR, kütle ve ^{1}H-NMR spektroskopisi gibi tekniklerin yanı sıra teorik hesaplamalar kullanıldı. Çözücü, pH ve zaman gibi faktörler kullanırak probların spesidik iyonlara ilgileri ortaya çıkarılarak optimisazyon koşulları belirlendi. Sonuçlarda PP-1 farklı pH seviyelerinde birden fazla iyonla etkileşime girerken, PP-2 ve PP-3 belirli iyonlara karşı seçici tepkiler gösterdi. Rhodamin bazlı problarda ise özellikle sudaki organik çözücüler ve tampon çözeltilerinin karıştırılmasında seçici iyon etkileşimleri gösterdi. Her bir probun iyonlar için tespit limitinin (LOD), miktar belirleme limitinin (LOQ) ve bağlanma sabitleri (K_a) hesaplanarak kantitaif analiz yapıldı. Sonuçlarda probların Al^{3+} için LOD değerleri 23 nM ile 554 nM arasında değiştiği ve atık su numunelerindeki alüminyumun tespitinde etkili olabileceği belirlendi. Benzer şekilde diğer iyonlar için LOD değerleri Hg^{2+} için 1,01 mM'den 334 nM'ye değiştiği, Zn^{2+} için 64 nM'den 550 nM'ye değiştiği, Cd^{2+} için 15 nM'den 551 nM'ye değişti belirlendi. Ayrıca, PP-3'ün Cu^{2+} için LOD değeri 1,56 mM olarak hesaplanıldı. Problar, çevresel numunelerdeki iyonları tespit etmek için WHO limitleri dahilinde hassasiyet sergiledi. Ek olarak, tersine çevrilebilirlik çalışmaları, su numuneleri ve sigara dumanı da dahil olmak üzere gerçek numuneler üzerinde probun yeniden kullanım ve uygulama potansiyeli incelendi. Elde edilen sonuçlarda probların gerçek numunelerde kullanılabileceği görüldü. Genel olarak, sentezlenen probların çevresel kirleticileri (Al^{3+}, Hg^{2+}, Cu^{2+}, Cd^{2+}, Zn^{2+}) ve biyolojik ajan GSH'yi tespit etmede etkili olduğu, çevresel ve biyolojik izleme potansiyeline sahip olduğu ortaya çıkarıldı.

Anahtar Kelimeler: Fenolftalein, rhodamin, sensor, tetrafeniletilen, alüminyum, bakır, civa, kadmiyum, çinko.

1. INTRODUCTION

1.1. General Information

Fluorogenic physical sensors stand out among the various types of chemical sensors due to their selective properties, high sensitivity, and efficiency. Their significance stems from their ability to provide important information in the field of environmental or chemical elements analysis. These sensors have gained prominence in chemical laboratories, industrial laboratories, and medical laboratories over the years, thanks to their simplicity, rapid analysis, and effectiveness compared to traditional methods (Yuan et al., 2019; Xu et al., 2020). Extensive studies have explored the possibility of fluorogenic Physical sensors detecting various metals and anions using spectroscopic and colorimetric techniques. These sensors, which detect cations and anions, are essential in medical, industrial, agricultural, and biological processes. Developing chemical sensors with desirable properties such as selectivity, sensitivity, and reusability is essential. Therefore, the identification of cations and anions is crucial in many physical, chemical, and biological processes and is essential in medical, biological, industrial, and environmental research (Bayindir et al., 2016; Toprak and Kollur, 2021; Hussein et al. 2023).

Maintaining a healthy lifestyle necessitates vigilant monitoring of mineral and anion levels across various concentrations in the body. These elements play critical roles in numerous physiological processes, such as enzyme function, nerve transmission, and fluid balance. Imbalances, whether deficiencies or excesses, can lead to significant health issues. Given the critical importance of these elements, it is necessary to use methods that can accurately and sensitively detect metals and anions at different concentrations. Traditional detection methods often involve sophisticated and expensive instruments, which may not be available for routine monitoring (Dinatale et al., 2006; Sikdar et al., 2018). Detection methods for heavy metals and anions often depend on advanced and expensive instruments. Techniques such as atomic absorption spectroscopy and atomic emission spectroscopy are commonly used. Additionally, inductively coupled plasma techniques, which include mass spectrometry, despite their widespread use, these techniques have limitations in sensitivity and selectivity. They may not detect low concentrations of certain elements or differentiate between similar ions effectively, necessitating the development of more efficient and cost-effective detection methods. Therefore, the development and identification of more effective and affordable, highly sensitive, and accurate methods for managing metal and anion levels are crucial (Dinatale et al., 2006; Sikdar et al., 2018; Chua et al., 2021).

Zinc, the second most abundant transition metal in the human body, plays a critical role in a multitude of physiological processes. It is integral to functional regulation, structural organization, and enzymatic catalysis. Despite its significance, an imbalance of zinc can contribute to various nerve-related diseases, including Parkinson's and Alzheimer’s. The concentration of zinc in blood plasma serves as a diagnostic indicator for numerous human diseases, including dwarfism. Zinc also participates in several physiological reactions, including those related to immunity, protein and enzyme synthesis, reproductive functions, and cellular growth and division. Within living organisms, zinc is essential for cellular activity, acting through catalytic, regulatory, and structural mechanisms in animal and plant cells alike. Its biochemical and physiological interactions have been extensively researched. Despite the importance of accurate zinc level diagnosis, many advanced methods encounter challenges in this area. Developing more precise diagnostic techniques for zinc levels is crucial for comprehending its impact on health and disease (Roohani et al., 2013; Duygu et al., 2021; Hussein et al., 2023). The world health organization WHO has indeed established guidelines for acceptable levels of zinc in various environments to ensure human health and environmental safety. These guidelines help regulate the use and disposal of materials containing zinc to prevent harmful effects on ecosystems and human health. However, the acceptable levels of zinc intake for humans are typically around 8-11 mg/day for adult males and 6-8 mg/day for adult females, as recommended by the (WHO). These values may vary depending on factors such as age, sex, and health status (Istitute of Medicine, 2001; World Health, 2004).

Aluminum, a lightweight and silvery metal, is abundant in the earth's crust. Its remarkable corrosion resistance, low density, and malleability make it highly valuable in various industries. The aerospace, automotive, packaging, and construction sectors extensively use aluminum due to its strength and versatility. However, despite its many benefits, excessive exposure to aluminum can pose health risks. Studies suggest a potential link between high aluminum exposure and neurological disorders like alzheimer's disease. Additionally, aluminum exposure has been associated with bone disorders, kidney problems, and respiratory issues. To mitigate these risks, it is crucial to manage aluminum exposure carefully. This includes implementing proper handling and disposal practices to minimize environmental contamination and human health impacts (Rosseland et al., 1990; Shi and Kim, 2012; Duygu and Alici, 2021). The world health organization has established guidelines for the average human intake of aluminum to be about 3-10 mg per day. Additionally, the permissible limit for the concentration of aluminum in drinking water is 5 mg/L (milligrams per liter), which is equivalent to 7.41 μM (micromoles per liter). These guidelines ensure that the water is safe for consumption and does not pose any health risks related to aluminum contamination. (World Health, 2008 and 2011).

Cadmium is a highly toxic heavy metal that poses serious health risks due to its tendency to accumulate in the body over time. Chronic exposure to cadmium has been linked to various health problems, including kidney damage, lung cancer, and cardiovascular disease. Smokers are particularly vulnerable to cadmium exposure because tobacco plants readily absorb cadmium from the soil, which then accumulates in the leaves. When tobacco is smoked, cadmium is released and inhaled into the lungs, leading to increased cadmium levels in the body (Kubier and Naila 2019). Cadmium is classified as a group 1 carcinogen by the international agency for research on cancer (IARC), indicating that it is known to cause cancer in humans. Its extensive distribution in the environment leads to severe and often irreversible damage to both human health and ecosystems. To mitigate the health risks associated with cadmium exposure, it is crucial to quit smoking or use alternative nicotine delivery methods that do not involve burning tobacco. Additionally, avoiding other sources of cadmium, such as certain foods and environmental contaminants, can further reduce overall cadmium intake. Regular monitoring of cadmium levels in individuals at risk of exposure, particularly smokers, may also be beneficial (Kalcher et al., 1993). The WHO has set the maximum permissible level of cadmium ions in drinking water at 3 µg/L or 27 nmol/L (Tsakilas et al., 2005; World Health, 2008). The cadmium content in cigarette tobacco averages between 0.6 and 3.6 mg/kg, making smoking one of the primary sources of cadmium exposure in humans. Mainstream smoke, which is the smoke inhaled directly by a smoker from a burning cigarette, contains about 5-10% of the total cadmium present (Kalcher et al., 1993; Piade et al., 2015).

When it comes to toxic liquid metals, ***mercury*** ranks prominently, after plutonium in its toxicity (Kollur et al., 2021). The prevalence of mercury in the environment has escalated over time due to its extensive utilization in industries such as paper manufacturing, mining, and hydroelectric power (Bernard et al., 2000; Yu et al., 2006; Momidia et al., 2016). Mercury in its elemental form presents a significant health hazard as it commonly enters the body through the skin. The DNA damage caused by elemental mercury results in various diseases affecting the kidneys, blood vessels, and heart (Clarkson, et al., 2006; Björkman L et al., 2007). As a result, it emphasizes the importance of developing efficient, swift, and affordable detection techniques for biological systems and the environment, while also advocating for the reduction of mercury levels in drinking water (Bayindir and Lafzi 2023). Exposure to mercury can lead to numerous health issues, emphasizing the importance of maintaining mercury levels in drinking water at or below two parts per billion, regulatory bodies like the environmental protection agency (EPA) and the WHO have delineated parameters for permissible mercury concentrations in potable water. The EPA has stipulated the highest allowable concentration of mercury in drinking water at 2 parts per billion (Bernard et al.,2000; Yu et al., 2006; World Health, 2008).

Copper, a crucial trace element, is essential for numerous physiological processes in the human body. It acts as a cofactor for various enzymes, aiding in critical functions such as energy production, iron metabolism, and the formation of connective tissue. However, when copper is dissolved in water, its ions can have significant impacts on both the environment and human health. In small amounts, copper is vital for maintaining health, supporting the immune system, and facilitating the absorption of iron. Nonetheless, when present in excessive levels in drinking water, copper can become toxic. Symptoms of copper toxicity include gastrointestinal distress, such as stomach cramps and nausea, as well as more severe conditions like liver and kidney damage. Unlike mercury, where even minimal exposure is hazardous, the primary issue with copper is the danger posed by its excessive levels. Recent years have seen a surge in research aimed at analyzing copper concentrations for field applications. Studies by (Zhang et al., 2018; Bayindir and Lafzi 2023) have contributed significantly to our understanding of copper's behavior and its detection in various environments. despite its essential role, copper is often found in excessive amounts in soil, water, and living organisms due to natural and anthropogenic activities (Tapiero et al., 2003; Elkhatat et al., 2021). Have documented the prevalence of copper in these mediums, highlighting the need for effective monitoring. To mitigate the health risks associated with high copper levels, regulatory agencies have established guidelines to ensure that copper concentrations in drinking water remain within safe limits. The world health organization has set the acceptable level of copper in drinking water at 2 mg/L, while the EPA in the United States has set it at 3 mg/L (Guidelineset al., 2017; Unitedet, 2020; Trevino et al., 2022). These standards are designed to protect public health and the environment.

Fluoride is a ubiquitous mineral in nature, with widespread presence in the environment (World Health Organization, 2011; D. Sukhvinder et al., 2020; Hussein et al., 2023). It serves a pivotal role in various scientific and daily life applications, including dental care treatments, psychiatric medications, and anesthetics (Ayoob et al., 2006; Liwei et al., 2020). While fluoride is beneficial in controlled amounts for dental health, excessive intake can lead to fluorosis, resulting in adverse health effects such as kidney failure, depression of thyroid activity, and bone disorders (Maguire et al., 2013). Acute fluoride poisoning poses a significant risk to human health, with higher doses potentially leading to fatalities and serious health issues, including plant damage, thyroid problems, brain damage, and dental abnormalities. The lethal dose of fluoride is approximately 2-5 grams, while dental problems can arise from concentrations of 2-5 mg/mL in liquids. Thyroid disorders can occur at concentrations of 50-100 mg/L in food or liquids, with (IQ) level decreases noted at 4-10 mg/L in liquids and neurological disorders at 8-50 mg/L in liquids (Maguire et al., 2012; Ali et al., 2016; Hussein et al., 2023). This highlights the multifaceted challenges associated with managing fluoride exposure and its impact on public health. The World Health Organization and the Environmental Protection Agency have established guidelines for safe fluoride levels in drinking water. The WHO recommends 0.5 to 1.5 mg/L, while the EPA specifies 4.0 mg/L (World Health Organization, 2011).

Cyanide refers to any chemical compound containing a cyano group (–C≡N). These compounds can be highly toxic, cyanide is utilized in electroplating metallurgy and the synthesis of organic chemicals. Sodium and potassium cyanide are specifically employed to extract gold and silver from ores. Cyanide inhibits cytochrome oxidase in the mitochondria, which obstructs cellular respiration and leads to cellular hypoxia (lack of oxygen). Severe poisoning can result in convulsions, coma, and death. An obsession and addiction to tobacco products increased to 22.3 % of overall global population (Hatsukami et al., 2008). A consumption of tobacco product always intertwined with the health disorders by the harmful chemicals inherent in it. Some of the highly destructive and toxic chemicals are nicotine, hydrogen cyanide, lead, arsenic, cadmium ions, formaldehyde, carbon monoxide and polyaromatic hydrocarbons (Morgan et al., 2017). In which, hydrogen cyanide is the major anion present in the tobacco products like cigar, cigarette etc. A pyrolysis of nitrogen containing organic compounds such as protein gives rise to cyanogen’s (Monago et al., 2005). Cyanide levels in smoke from U.S. commercial cigarettes range from 10 to 400 µg/cigarette for mainstream (inhaled) smoke and from 0.006 to 0.27 µg/cigarette for side stream (passive) smoke, the presence of cyanide in waste helps dissolve heavy metals such as mercury, lead and other toxic metals in the water (Undquist et al., 1978).

The majority of chemical sensors exhibit hydrophobic properties, thus restricting the detection process to be performed exclusively in a solution containing a large amount of organic solvent (Thakur et al., 2018). Chemical sensors in real samples present an enormous challenge, necessitating the development of chemical sensors that are highly sensitive and selective for both anions and cations in aqueous media (Gunnlaugsson et al., 2006; Thakur et al 2018). For this reason, detecting ions with high sensitivity and selectively, especially in aqueous solvent systems, without the need for any expensive equipment is very valuable and attracts the attention of scientists (Kim et al., 2012). Aqueous solutions play a crucial role in the determination and detection of ions using organic reagents. Their significance stems from several key factors. *Solubility***,** many organic reagents utilized in ion detection readily dissolve in water, facilitating the preparation of reagent solutions and their interaction with target ions. *Reaction medium***,** aqueous solutions provide an ideal medium for the reactions between organic reagents and ions. Water molecules assist in facilitating these reactions, leading to the formation of complexes or precipitates that aid in the detection process. *Compatibility***,** aqueous solutions are compatible with numerous analytical instruments and techniques employed in ion detection, such as spectrophotometry or chromatography. This compatibility allows for the seamless integration of aqueous samples into analytical workflows. *Environmental relevance,* since many ions of interest, including those present in environmental samples or biological fluids, are found in aqueous solutions, detecting ions using organic reagents in these solutions is crucial for environmental monitoring, health diagnostics, and various other applications (Covington et al., 1973). Chemical sensing reactions can be influenced by the choice of solvent, as it has the capacity to control both the physical and chemical properties involved. Consequently, researchers often rely on the trial-and-error method to select the most suitable solvent for their experiments (Bernard et al., 2000). The probe unit in question, documented extensively in the literature, operates as an energy donor component when combined with specific fluorophores to create effective organic sensing materials. This means that the probe can transfer energy to another fluorophore, which then emits light, facilitating the detection of various substances (Ma et al., 2018; Li et al 2019; Jagadhane et al., 2022).

In the field of sensor studies, dyes such as phenolphthalein (**PP**) and rhodamine B (**RhB**) are commonly used due to their ability to act as color sensors under specific conditions. These dyes are highly prized for their characteristic and noticeable color changes in response to pH changes, making them valuable tools in detecting and measuring different ions in different environments (Chandra et al., 2009;Kim et al., 2012). Phenolphthalein is a classic pH indicator that acts as a color sensor in basic environments Figure 1.1. It is colorless in acidic conditions and turns pink to fuchsia as the pH rises, usually becoming distinctly colored in basic conditions (pH > 8.2). This color change is due to the molecular structure of **PP** which undergoes a ring opening reaction when exposed to a basic environment, converting it from its colorless form to its colored form. This property makes them particularly useful in titrations and other analytical procedures where detection of the endpoint of a reaction is crucial (Alici and Aydinet 2021). Rhodamine B on the other hand, acts as a color sensor in acidic environments. Rhodamine is known for its light pink to red color under acidic conditions and its colorless form under basic conditions Figure 1.1. The color change of **RhB** is also attributed to the structural transformation involving ring opening and closing mechanisms, depending on the pH. This behavior is exploited in various sensing applications where it is necessary to monitor changes in acidity or the presence of acidic compounds (Li et al.,2013;Bayindir et al., 2024). Importance in developing sensors, the color change mechanisms of **PP** and **RhB**, driven by their structural transformations, highlight their potential in ion-selective detection. The selective and reversible color changes make these dyes effective in developing sensors that can visually indicate the presence of specific ions based on pH changes. The research emphasizes the importance of manufacturing new derivatives of these dyes to enhance their selectivity and sensitivity towards different ions. (Shi et al., 2012; Guo et al., 2015; Erdemir et al., 2019). The use of **PP** and **RhB** in sensor studies is well established, and their color change mechanisms provide a solid foundation for the development of advanced ion detection systems. By synthesizing new derivatives, the researchers aim to create more sensitive, selective and powerful sensors, expanding the potential applications of these dyes in various scientific and industrial fields (Bernard et al., 2000).

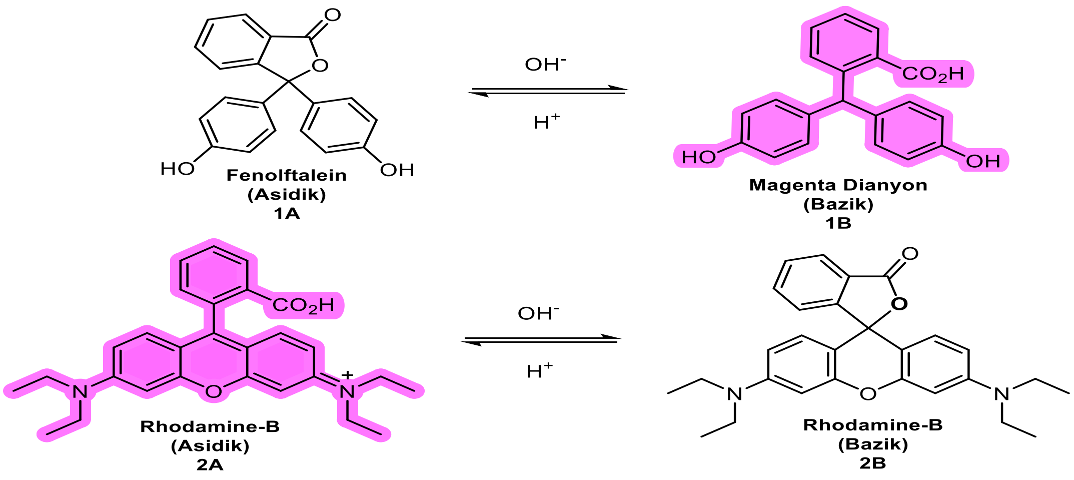

Figure 1.2. Molecular structures of phenolphthalein (1) and rhodamine B (2) in the acidic/basic medium

1.2. Literature Review

Phenolphthalein and Rhodamin B molecules are commercial indicators that change color depending on environmental pH values. In recent years, sensor studies have also been carried out on these indicators. Although there are a very limited number of studies on **PP**, the number of studies on these two dyes is increasing every year, some recent anion sensing studies on **PP** can be listed as follows. For this purpose, the researchers used 5,5'-(3-oxo-1,3-dihydroisobenzofuran-1,1-diyl) bis(2-hydroxybenzaldehyde) (PPDA, 3), which is also an aldehyde derivative and used as the starting molecule. One of the studies on **PP** was conducted by Elmas et al. (Scheme 1). In their research, they developed a probe based on phenolphthalein with both colorimetric and fluorescent properties. The study concluded that this new phenolphthalein derivative $(PH)_2PP$ is effective for detecting the carbonate ion (CO_3^{2-}) in a mixture $EtOH/H_2O$ (v/v: 8/2). The probe demonstrated high sensitivity and selectivity for (CO_3^{2-}) compared to other competing ions. Additionally, studies on liver cancer cells revealed the probe's significant potential in detecting intracellular carbon dioxide. Moreover, carbon dioxide was accurately detected in real water samples (Elmas et al., 2021).

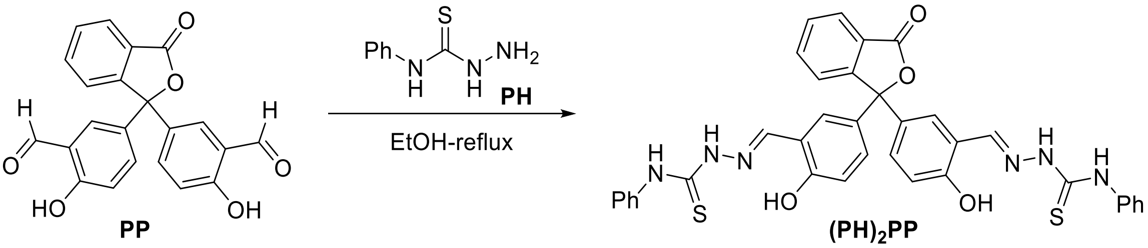

Scheme 1

Another recent study was conducted by Alici et al. In this research, Alici and colleagues synthesized a new phenolphthalein derivative $(FH)_2PP$ through a single-step reaction of the phenolphthalein derivative with furan-2-carbohydrazide in ethanol. They then examined the sensor properties of the synthesized compound on metal ions (Scheme 2). The study concluded that the obtained ligand exhibited specific selectivity for Al^{3+} ions in a mixture CH_3CN/H_2O (v/v: 1/1, HEPES, pH 7) (Alici et al., 2021).

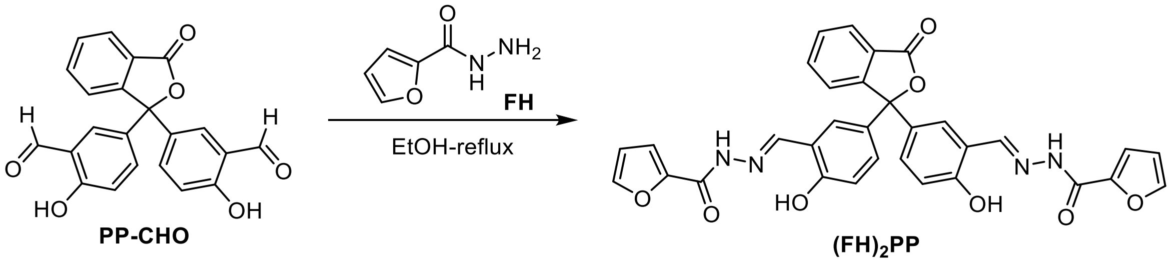

Scheme 2

In another study on phenolphthalein, Wang and his team synthesized the probe phenolphthalein-dialdehyde-(2-pyridyl)-hydrazone, a derivative of phenolphthalein, and employed a variety of metal ions sensing techniques (Scheme 3). Their research focused on the sequential detection of Al^{3+} and F^- ions in nearly 100% aqueous media, which exhibited an (Off-On-Off) fluorescence change upon the addition of Al^{3+} followed by F^-, effectively quenching the fluorescence of the complex with high selectivity. The sensor demonstrated the capability to detect Al^{3+} and F^- ions in living cells (Kong et al. 2019).

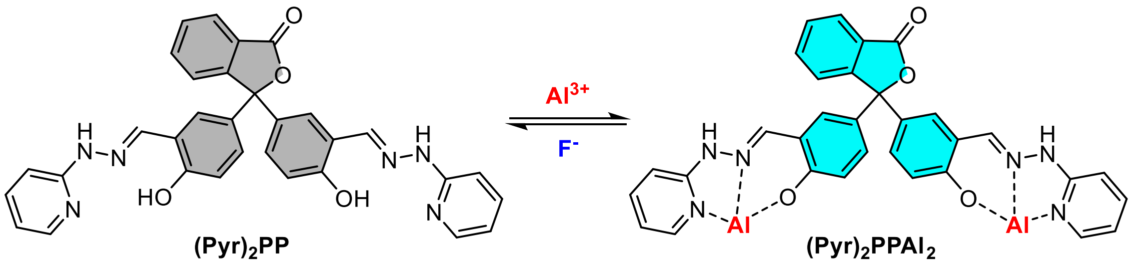

Scheme 3

In another study on phenolphthalein, Erdemir et al. synthesized the probe phenolphthalein-diaminomalonitrile (PDM), a derivative of phenolphthalein, using a variety of metal ions sensing techniques (Scheme 4). The probe is suitable for both fluorescence detection of Al^{3+} and colorimetric detection of Cu^{2+} in a 9/1 EtOH/H_2O (v/v) mixture. The reversibility of the PDM-Al^{3+} and PDM- Cu^{2+} complexes was demonstrated with the addition of F^- and EDTA, respectively. The results indicated that PDM can be used effectively in water sample analysis ions (Erdemir et al., 2019).

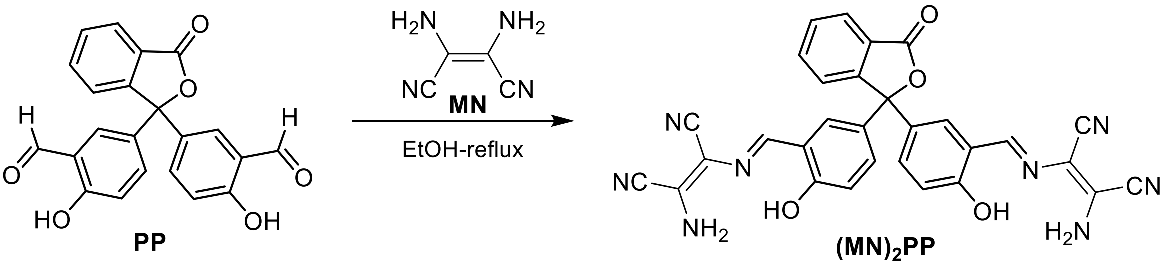

Scheme 4

Kong et al. (2022) developed a new fluorescent chemical sensor, the phenolphthalein-attached Schiff base, to detect Al^{3+} ions (Scheme 5). This sensor utilizes the pyrophosphate ions (PPi) displacement approach and exhibits a dual response following the (Off-On-Off) strategy in a solution DMF/H_2O (v/v:1/4, pH 5.5). The sensor was effectively used for detecting Al^{3+} in food samples and for intracellular imaging of Al^{3+} and PPi in human hepatocellular carcinoma cells (Kong et al., 2022).

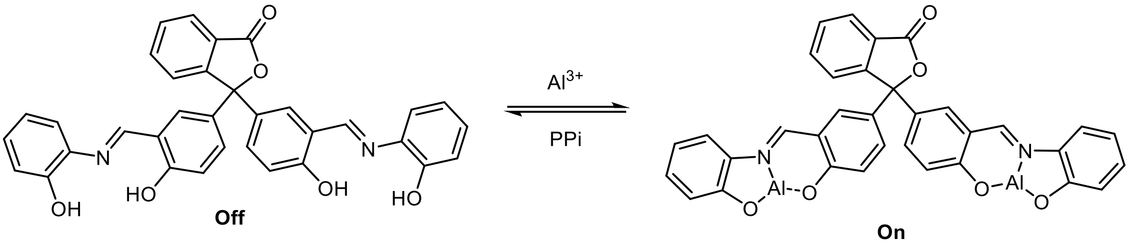

Scheme 5

The research conducted by Aydin et al. (2021) centers on developing a Schiff base by reacting phenolphthalein with isoniazid, which serves as a dual-emission fluorogenic probe for selectively recognizing aluminum and zinc ions among other related ions the probe operates effectively in the medium EtOH (9/1; v/v) (Scheme 6). The researchers evaluated the probe's performance in different aqueous media (Aydin et al., 2021).

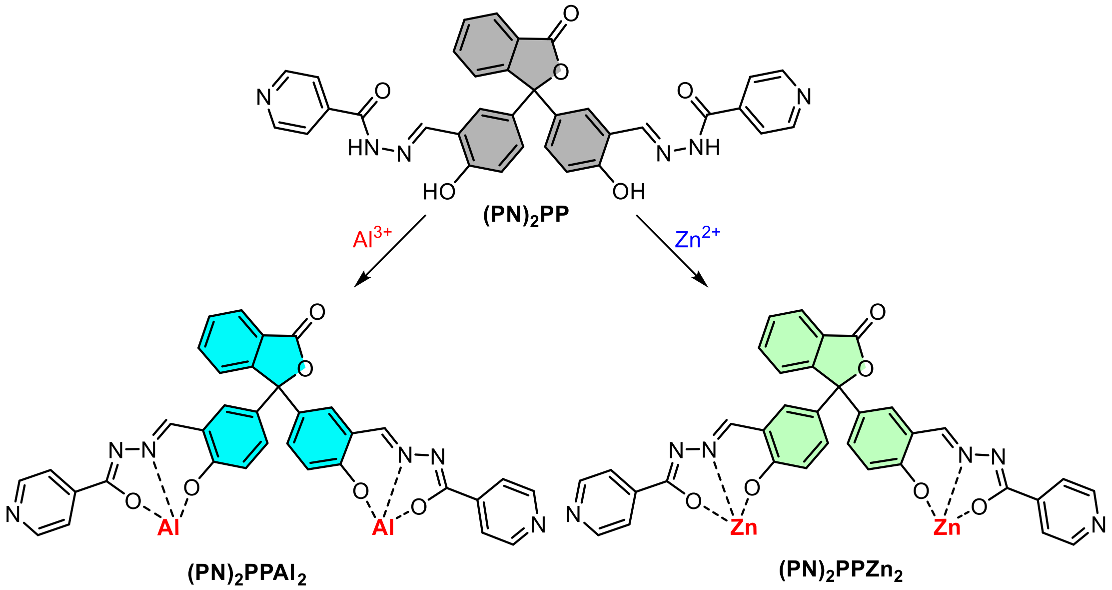

Scheme 6

In a different study, Erdemir et al. developed a probe called phenolphthalein-di-rhodamine (Rh)$_2$PP, synthesized from phenolphthalein and rhodamine B. This probe is highly effective in the fluorescent detection of Hg^{2+} and the colorimetric detection of Zn^{2+} in a mixture EtOH-H$_2$O (v/v: 8/2, 5 mM, HEPES, pH 7.0) (Scheme 7). The reversibility of the (Rh)$_2$PP-Hg^{2+} and (Rh)$_2$PP-Zn^{2+} complexes were confirmed by the addition of EDTA, following an (Off-On-Off) strategy. The findings indicate that this probe is highly efficient for ion analysis in real water samples (Erdemir et al., 2017).

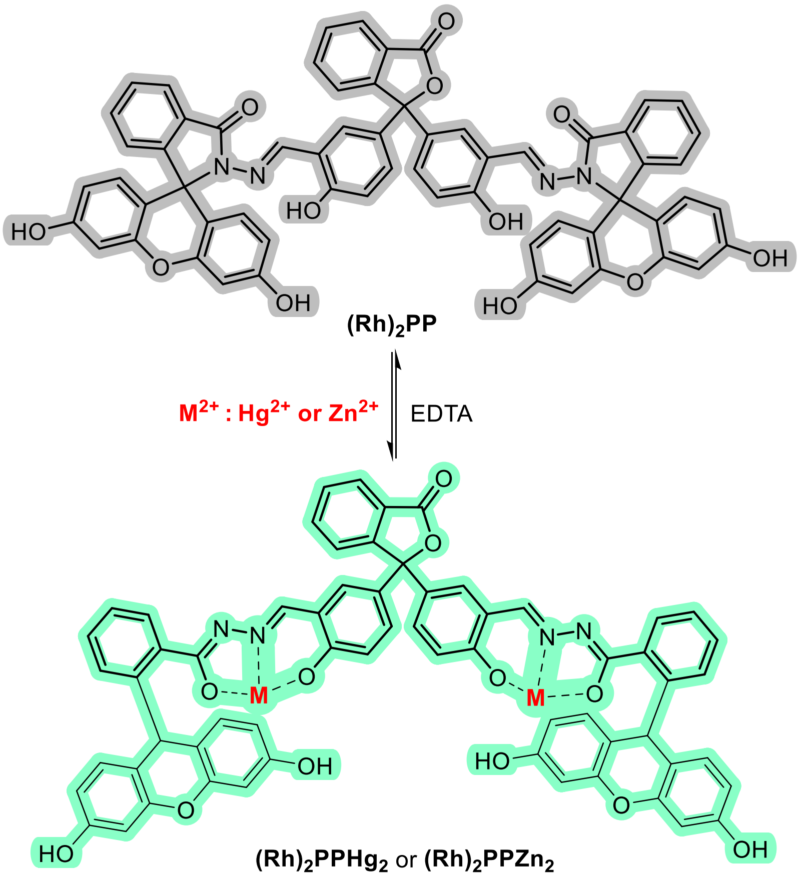

Scheme 7

Another important indicator that has been extensively studied, similar to phenolphthalein, is the rhodamine B molecule, which has seen increased research attention in recent years. The **RhB** derivative is quite similar in composition to the new derivatives that will be produced as part of this thesis. Li et al synthesized an effective fluorescent probe using rhodamine B acid chloride and furan-2-carbohydrazide (Scheme 8). This study examined its properties for metal detection, demonstrating high selectivity and excellent sensitivity towards Cu^{2+} in a CH_3CN/HEPES buffer solution (1:1, v/v, pH 7). The probe allows for the detection of Cu^{2+} with the naked eye and has been successfully applied to monitor intracellular Cu^{2+} in HeLa cells (Li et al., 2013).

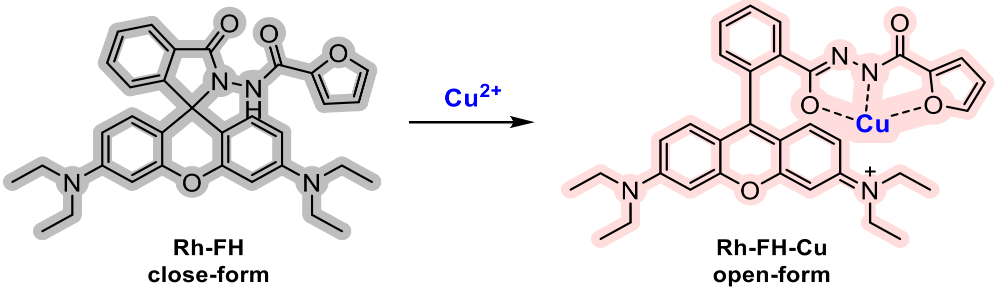

Scheme 8

Yang et al. designed a molecular sensor based on the rhodamine framework, known for its strong fluorescence properties and color change upon structural modification (Scheme 9). This structural transformation leads to a pronounced color change (red shift) and a significant increase in fluorescence, making the sensor effective for both colorimetric and fluorescent detection of Hg^{2+}, allowing it to be easily detected with the naked eye. The researchers evaluated the selectivity of the sensor by testing it against various other metal ions and showed that it specifically binds to Hg^{2+} in aqueous media. This indicates its practical applicability for monitoring mercury pollution in water (Yang et al., 2005).

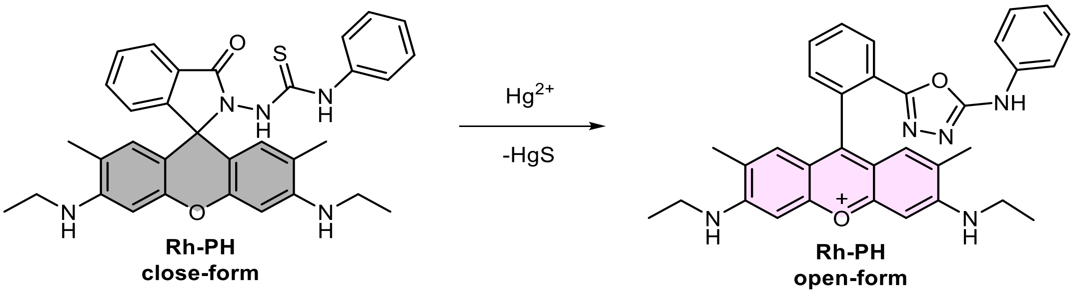

Scheme 9

Song et al. conducted another study on rhodamine. In this study, rhodamine B-pyridine (Rh-2-Pyr) chemical sensors were designed and synthesized (Scheme 10), and their sensing behavior toward different metal ions was evaluated using UV-vis and fluorescence spectroscopy techniques. The sensor showed good spectral responses to Fe^{3+} in an EtOH/H_2O solution (3:1, v/v, HEPES, 0.5 μM, pH = 7.33). The chemical sensor was also demonstrated to be practical for sensitively monitoring trace amounts of Fe^{3+} in real water samples. Fluorescence imaging experiments of Fe^{3+} in live human breast cancer cells demonstrated its potential value for applications in biological systems. (Song et al., 2018).

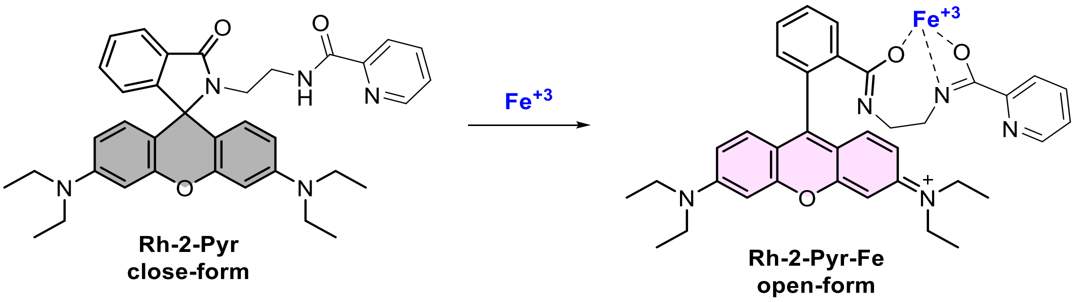

Scheme 10

Sikdar et al. synthesized a novel fluorescent derivative of rhodamine B that includes xanthene and pyridine groups (Scheme 11). They examined the optical properties of this compound in a solution diacetonitrile: water (7:3, v/v) with various ions. The sensor demonstrated high effectiveness in selectively detecting fluorescent and colorimetric changes upon the addition of Cu^{2+}. Furthermore, the sensor was successfully applied in living cells to detect the biologically and physiologically significant Cu^{2+} ion (Sikdar et al., 2013).

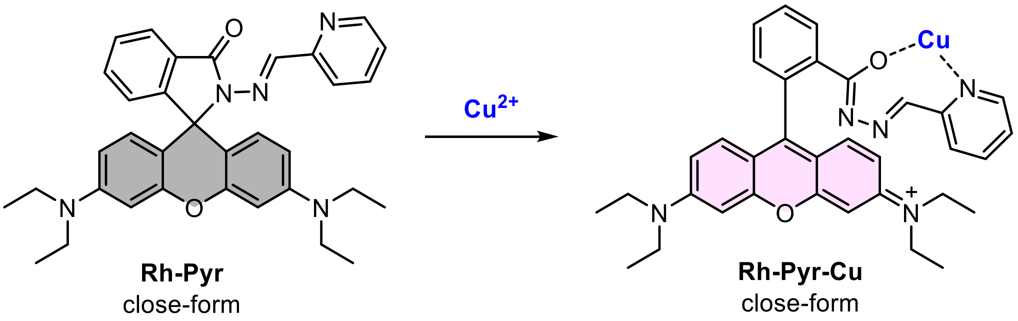

Scheme 11

Other significant markers, such as **PP** and **RhB**, have been studied. In recent years, their (TPE) tetraphenylethene derivatives have also been extensively investigated. Toprak et al. successfully developed a TPE-TSC (Scheme 12) fluorescent sensor capable of selectively detecting Cu^{2+} and Hg^{2+} ions in acetonitrile-water mixtures. The performance of the sensor was highly dependent on the proportion of water in the solvent mixture. The sensor exhibited selective and sensitive fluorescence responses to Cu^{2+} and Hg^{2+} in CH_3CN/H_2O mixtures containing 30-50% H_2O and 70-90% H_2O, respectively, highlighting the influence of solvent environment on fluorescence detection. This makes the sensor suitable for detecting trace amounts of these ions in environmental and biological samples (Toprak et al., 2021).

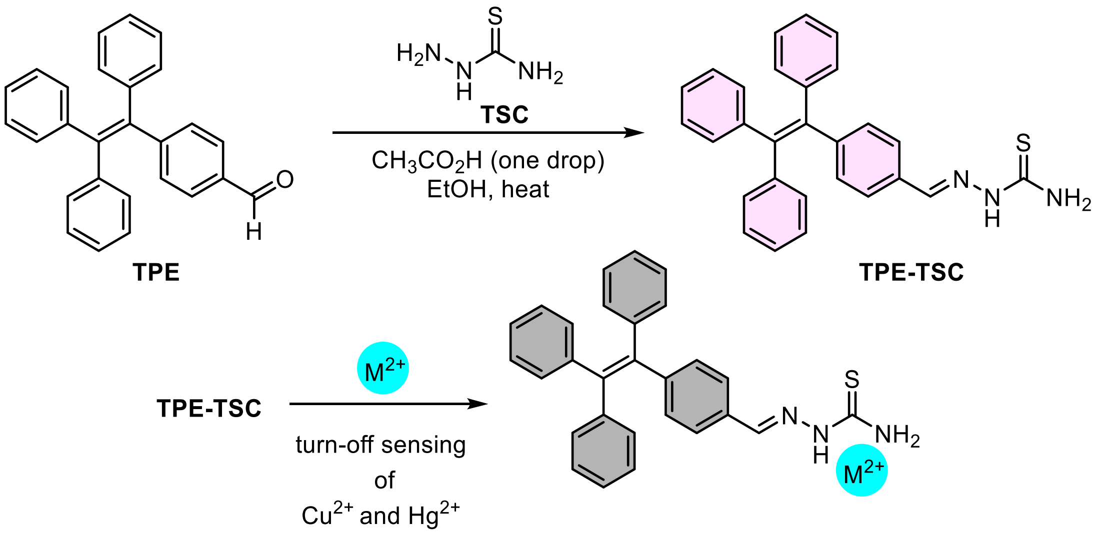

Scheme 12

Hussein et al. have synthesized a new derivative of BIS-TEP (Scheme 13) designed for fluorescence and colorimetric sensing. They studied its interactions with a wide range of ions using UV-vis and fluorescence spectroscopy in various solvent systems. Bis-TPE demonstrated effective sensor capabilities for Zn^{2+} in ethanol. Additionally, the Bis-TPE-Zn^{2+} system exhibited specific fluorescence responses to hydroxide ions following an (Off-On-Off) strategy (Hussein et al., 2023).

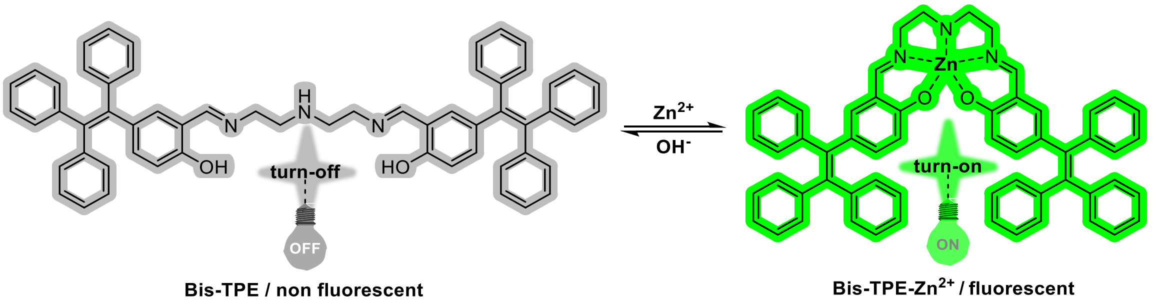

Scheme 13

Bayindır et al. conducted a study on TPE, synthesizing a new fluorescent and colorimetric derivative, TES-TEP-TES, which they analyzed using UV-vis and fluorescence spectroscopy. The study included AIE studies, demonstrating that the fluorescence intensity of TSC-TPE-TSC increased with higher water content. Their findings indicated that the probe showed excellent selectivity and sensitivity for Hg^{2+} or Cu^{2+} in tap water, distilled water, and $EtOH/H_2O$ (v/v:1/1, pH 7). TSC TPE-TSC-Hg^{2+} exhibited specific fluorescence responses to I^- ions in solvent systems. Moreover, effective detection systems were established for tap water, distilled water, and $EtOH/H_2O$ solvents for detecting Hg^{2+}, Cu^{2+}, and I^- (Bayındır et al., 2023).

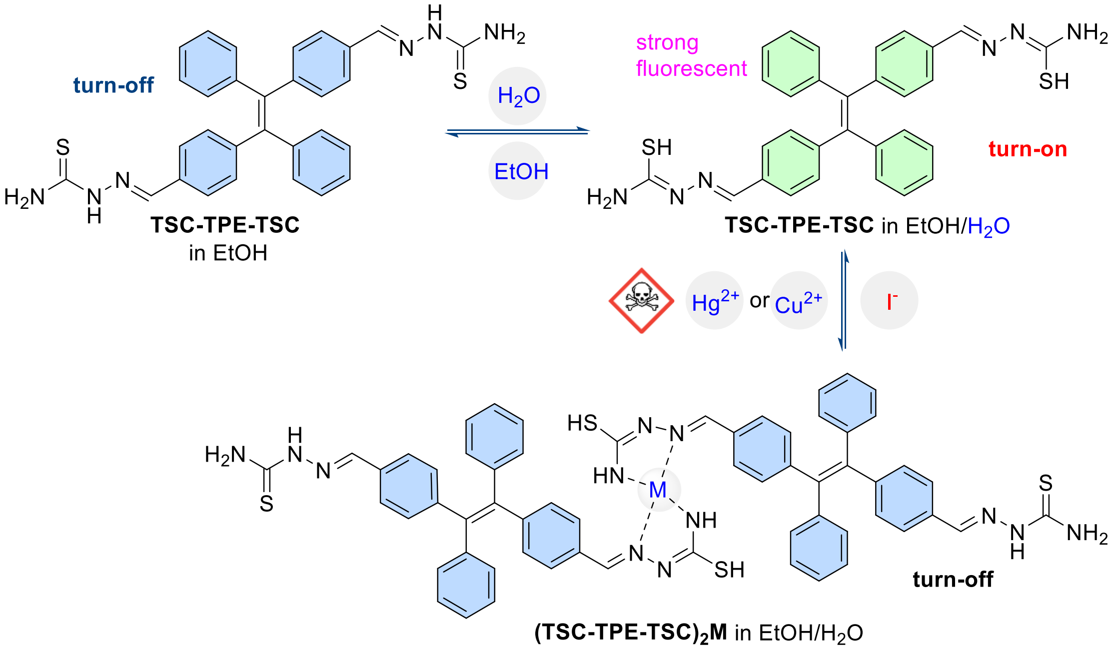

Scheme 14

2. EXPERIMENTAL

2.1. General Methods

All chemicals, reagents, and solvents were commercially available from Sigma-Aldrich or Merck. Infrared spectra were recorded on a Mattson 1000 FT-IR spectrophotometer. ^{1}H NMR and ^{13}C NMR spectra were recorded on a 400 (100)-MHz Varian and Bruker spectrometer and are reported in terms of chemical shift (δ, ppm) with $SiMe_4$ as an internal standard. Data for ^{1}H NMR are recorded as follows: chemical shift (δ, ppm), multiplicity (s: singlet, d: doublet, t: triplet, q: quartet, p: pentet, m: multiplet, bs: broad singlet, bd: broad doublet, qd: quasi doublet) and coupling constant (s) in Hz, integration. Elemental analyses were carried out on a LECO CHNS-932 instrument. High resolution mass spectra were recorded on Agilent QTOF (Quadrupole time-of-flight) spectrometry device. Column chromatography was carried out on silica gel 60 (230–400 mesh ASTM). The reaction progress was monitored by thin-layer chromatography (TLC) (0.25-mm-thick precoated silica plates: Merck Fertigplatten Kieselgel (60 F254)). UV-Vis absorption and fluorescence spectra of samples were recorded on a Shimadzu UV-3101PL UV-Vis-NIR spectrometer and Perkin–Elmer (Model LS55) Fluorescence Spectrophotometer, respectively.

2.2. The Synthesis of PPs

2.2.1. The Synthesis of PP-CHO

The synthesis of starting material 5,5'-(3-oxo-1,3-dihydroisobenzofuran-1,1-diyl) bis (2-hydroxy benzaldehyde) **(PP-CHO)** was synthesized according to the following literature (Guo et al., 2015). A solution of phenolphthalein (100mg, 0.30mmol) and hexamethylenetetramine (**HMTA**, 132 mg, 0.94 mmol) in TFA (8 mL) was refluxed for about 10 h, and then the reaction mixture was cooled to room temperature, a solution of HCl (1.0 M, 20 mL) was added to the resulting mixture. Following the reaction mixture was extracted with CH_2Cl_2 (20 mL). The organic layer was washed with water (20 mL x 3) and saturated brine once and was dried over Na_2SO_4. After the removal of the solvent, the target product PP-CHO was obtained as a white solid (yields of 76%). Following this, the crude PP-CHO was recrystallized from a mixture of ethanol/water. 1H NMR (400 MHz, DMSO-d6): δ 11.04 (s, OH, 2H,), 10.20 (s, CHO, 2H), 7.91 (d, J = 7.74 Hz, =CH, 1H), 7.79–7.76 (m, =CH, 2H), 7.65 (t, J = 7.52 Hz, =CH, 1H), 7.51 (d, J = 2.60 Hz, =CH, 1H), 7.43 (d, J = 2.60 Hz, =CH, 1H), 7.41 (d, J = 2.60 Hz, =CH, 1H), 7.02 (d, J = 8.73 Hz, =CH, 1H).

2.2.2. The Synthesis of PP-1

The target *N',N'''*-((1E,1'E)-((3-oxo-1,3-dihydroisobenzofuran-1,1-diyl)bis(6-hydroxy-3,1-phenylene))bis(methaneylylidene))bis(3-methoxybenzohydrazide) (PP-1) was synthesized as following procedure. The Ph-CHO (100 mg, 0.27 mmol) and 3-methoxybenzene hydrazide (89 mg, 0.54 mmol) were mixed in ethanol and refluxed overnight with one drop CH_3CO_2H catalyst. The reaction was monitored with TLC. After, the mixture product was recrystallized from EtOH. After recrystallization, PP-1 (162 mg, 90%) was obtained as a pale-yellow solid. 1H NMR (400 MHz, DMSO-d6) δ 12.06 (s, OH, 2H), 11.32 (S, NH, 2H), 8.67 (s, N=CH, 2H), 7.96 (d, J = 7.1 Hz, =CH, 1H), 7.87-7.89 (m, =CH, 2H), 7.70 (t, J = 7.1 Hz, =CH, 1H), 7.55 (bs, =CH, 2H), 7.42-7.51 (m, =CH, 6H), 7.24-7.26 (m, =CH, 2H), 7.16-7.17 (m, =CH, 2H), 6.97-7.00 (m, =CH, 2H), 3.32 (s, CH3, 6H); 13C NMR (100 MHz, DMSO-d6) δ 169.54, 163.28, 159.90, 158.09, 152.45, 147.77, 135.74, 134.88, 132.31, 130.69, 130.61, 130.41, 127.33, 126.32, 125.14, 125.07, 120.50, 119.65, 118.39, 117.47, 113.52, 91.34, 56.02; LC-MS (ESI) m/z: $[M^+]$ calcd for $C_{38}H_{30}N_4O_8$, 670.2050 (m/z) found 670.2044 (m/z). FTIR (ATR): 2239, 2212 cm^{-1} (CN), 1724 cm^{-1} (C=O), 1617 cm^{-1} (C=N).

2.2.3 The Synthesis of PP-2

Another target probe *N*',*N*'''-((1E,1'E)-((3-oxo-1,3-dihydroisobenzofuran-1,1-diyl) bis(6-hydroxy-3,1-phenylene))bis(methaneylylidene))bis(2-(1*H*-indol-3-yl)acetohydrazide)(PP-2) was synthesized as following procedure. The Ph-CHO (100 mg, 0.27 mmol) and 2-(1*H*-indol-3-yl) acetohydrazide (101 mg, 0.54 mmol) were mixed in ethanol and refluxed overnight with one drop CH_3CO_2H catalyst. The reaction was monitored with TLC. After, the mixture product was recrystallized from EtOH. After recrystallization, the target PP-2 (138 mg, 72%) was obtained as a pale-yellow solid. ^1H NMR (400 MHz, DMSO-d6) δ 11.74 (s, OH, 2H, isomer), 11.26 (s, NH, 2H, isomer), 11.23 (s, OH, 1H, isomer), 10.95 (s, NH, 1H, isomer), 10.83 (m, indole-NH, 2H, isomer), 10.43 (m, indole-NH, 1H, isomer), 8.43 (m, N=CH, 2H, isomer), 8.24 (m, N=CH, 1H, isomer), 6.91-7.82 (m, =CH, 30H), 3.64 (s, CH2, 2H, isomer), 3.40 (s, CH2, 4H, isomer) ; 13C NMR (100 MHz, DMSO-d6) δ 172.71, 169.37, 169.31, 167.56, 167.51, 157.74, 157.71, 156.91, 152.36, 152.25, 146.20, 146.11, 139.93, 139.78, 136.58, 136.53, 136.48, 135.49, 135.38, 132.14, 132.05, 131.99, 130.32, 130.22, 130.12, 127.74, 127.59, 127.21, 126.99, 126.08, 124.91, 124.82, 124.70, 124.48, 124.32, 124.19, 121.53, 121.41, 120.49, 119.39, 119.32, 119.24, 119.20, 119.09, 118.92, 118.88, 118.75, 117.15, 111.86, 111.79, 108.29, 108.22, 91.24, 91.11, 31.90, 29.70. LC-MS (ESI) m/z: [M^+] calcd for $C_{42}H_{32}N_6O_6$, 716.2350 (m/z) found 716.2340 (m/z). FTIR (ATR): 2239, 2212 cm^{-1} (CN), 1748 cm^{-1} (C=O), 1664 cm^{-1} (N-C=O), 1617 cm^{-1} (C=N) (Scheme 1B).

2.2.4. The Synthesis of PP-3

Another target probe(2E,2'E)-2,2'-((3-oxo-1,3-dihydroisobenzofuran-1,1-diyl)bis(6-hydroxy-3,1-phenylene))bis(methaneylylidene))bis(hydrazine-1-carbothioamide) (PP-3) was synthesized as following procedure. The PP-CHO (100 mg, 0.27 mmol) and hydrazine carbothioamide (49 mg, 0.54 mmol) were mixed in ethanol and refluxed overnight with one drop CH_3CO_2H catalyst. The reaction was monitored with TLC. After, the mixture product was recrystallized from EtOH. After recrystallization, the target PP-3 (112 mg, 81%) was obtained as a yellow solid. ^1H NMR (400 MHz, DMSO-d6) δ 11.40 (s, OH, 2H), 10.30 (s, NH, 2H), 8.32 (s, N=CH, 2H), 8.03-8.12 (m, =CH, 3H), 7.82-7.89 (m, =CH, 2H), 7.65-7.69 (m, =CH, 5H), 7.19 (m, =CH, 2H), 6.88 (m,

=CH, 2H); APT 13C NMR (100 MHz, DMSO-d6) δ 178.00, 169.47, 156.96, 152.29, 140.42, 135.31, 132.37, 130.26, 130.04, 125.96, 125.23, 125.17, 124.87, 120.46, 116.69, 91.19; LC-MS (ESI) m/z: $[M+H]^+$ calcd for $C_{24}H_{21}N_6O_4S_2$, 521.1055 (m/z) found 521.1090 (m/z). FTIR (ATR): 3160 cm^{-1} (NH), 2239, 2050 cm^{-1} (CN), 1748 cm^{-1} (C=O), 1598 cm^{-1} (C=N).

2.3. The Synthesis of Rhs

2.3.1. The Synthesis of Rh-NH_2

The starting material 2-(2-aminoethyl)-3',6'-bis(diethylamino)spiro[isoindoline-1,9'-xanthen]-3-one (Rh-NH_2) was synthesized according to the following literature (Guo et al., 2015). Ethylenediamine (1.0 mL, 15.08 mmol) was added dropwise to a solution of rhodamine B (1.0 g, 2.01 mmol) in 25 mL of ethanol. The solution was heated to reflux for 16 h and evaporated to dryness. The resulting residue was dissolved in water and extracted with DCM (2x 15 mL). The combined organic phases were washed with water and dried over Na_2SO_4. The solvent was removed by evaporation and the remaining solid was dried in vacuo, affording Rh-NH_2 as a pinkish powder (0.96 g, 99%). ^{1}H NMR (400 MHz, $CDCl_3$) δ 7.92 – 7.87 (m, 1H), 7.49 – 7.38 (m, 2H), 7.19 – 7.00 (m, 1H), 6.43 (s, 1H), 6.41 (s, 1H), 6.36 (d, J = 2.6 Hz, 2H), 6.26 (dd, J = 8.9, 2.6 Hz, 2H), 3.32 (q, J = 7.1 Hz, 8H), 3.18 (t, J = 6.6 Hz, 2H), 2.40 (t, J = 6.6 Hz, 2H), 1.38 (s, 2H), 1.15 (t, J = 7.0 Hz, 12H).

2.3.5. The Synthesis of Rh-1 (Rh-PP-Rh)

Culminating this thesis, Rh-PP-Rh is a novel probe featuring both phenolphthalein and rhodamine moieties. The Rh-PP-Rh was synthesized in the following procedure. The mixture of PP-CHO (50 mg, 0.13 mmol) and Rh-NH_2 (130 mg, 0.26 mmol) in 15 mL of dry EtOH was subjected to reflux overnight. The reaction completion was verified using TLS. The resulting precipitate was filtered, washed with ethanol, and vacuum-dried, yielding orange solid Rh-PP-Rh (165 mg, 94% yield). 1H NMR (400 MHz, DMSO-d6) δ 13.22 (bs, OH, 2H), 8.03 (s, N=CH, 2H), 7.91 (d, J = 8.0 Hz, =CH, 1H), 7.76-7.80 (m, =CH, 5H), 7.63-7.67 (m, =CH, 1H), 7.46-7.52 (m, =CH, 4H), 7.15-7.21 (m, =CH, 4H), 7.00-7.03 (m, =CH, 2H), 6.82 (d, J = 8.0 Hz, =CH, 2H), 6.35-6.37 (m, =CH, 5H), 6.20-6.27 (m, =CH, 6H), 3.20-3.23 (m, CH2, 24H), 1.00-1.07 (m, CH3, 24H); ^{13}C NMR (100

MHz, DMSO-d6) δ 169.45, 167.72, 166.94, 161.73, 153.81, 153.33, 153.23, 152.44, 148.99, 135.71, 133.45, 131.50, 131.02, 130.50, 130.32, 129.02, 126.18, 125.02, 124.33, 123.03, 118.58, 117.76, 108.68, 105.60, 105.58, 105.27, 97.86, 91.15, 64.62, 56.70, 56.64, 44.32, 13.03. HRMS (ESI-TOF) m/z: $[M + H]^+$ calcd for$C_{82}H_{83}$N8O8, 1307.6328; found 1307.6345.

2.3.2. The Synthesis of Rh-2

The target probe (E)-2-(2-(([1,1'-biphenyl]-4-ylmethylene)amino)ethyl)-3',6'-bis(diethylamino) spiro[isoindoline-1,9'-xanthen]-3-one (Rh-2) was synthesized as following procedure. The Rh-NH_2 (100 mg, 0.21 mmol) and [1,1'-biphenyl]-4-carbaldehyde (37 mg, 0.21 mmol) were mixed in ethanol and refluxed overnight. The reaction was monitored with TLC. After, the mixture product was recrystallized from EtOH. After recrystallization, the target Rh-2 (102 mg, 76%) was obtained as a yellow solid. ^{1}H NMR (400 MHz, DMSO-d6) δ 7.97 (s, N=CH, 1H), 7.79-8.82 (m, =CH, 1H), 7.58-7.75 (m, =CH, 6H), 7.35-7.51 (m, =CH, 4H), 7.35-7.38 (m, =CH, 1H), 7.00-7.02 (m, =CH, 1H), 6.22-6.38 (m, =CH, 6H), 3.16-3.44 (m, CH2, 12H), 0.98-1.06 (m, CH2, 12H); APT 13C NMR (100 MHz, DMSO-d6) δ 167.63, 161.90, 153.81, 153.16, 148.84, 142.62, 139.74, 135.25, 133.24, 130.82, 129.48, 128.94, 128.89, 128.82, 128.37, 127.19, 127.15, 124.08, 122.79, 108.57, 105.33, 97.61, 64.64, 58.75, 44.11, 41.25, 12.81; LC-MS (ESI) m/z: $[M+H]^+$ calcd for $C_{43}H_{46}N_4O_2$, 649.3500 (m/z) found 649.3539 (m/z); FTIR (ATR): 34224 cm^{-1} (NH), 2968-2464 cm^{-1} (C-H stretch), 2260 cm^{-1} (C-N), 1690 cm^{-1} (O-C=O), 1653 cm^{-1} (C=N).

2.3.3. The Synthesis of Rh-3

Another target probe 2,2''-((((1E,1'E)-(((E)-1,2-diphenylethene-1,2-diyl)bis(4,1-phenylene))bis(methaneylylidene))bis(azaneylylidene))bis(ethane-2,1-diyl))bis(3',6'-bis (diethylamino)spiro[isoindoline-1,9'-xanthen]-3-one)(Rh-3) was synthesized as following procedure. The Rh-NH_2 (100 mg, 0.21 mmol) and (E)-4,4'-(1,2-diphenylethene-1,2-diyl) dibenzaldehyde (TPE$(CHO)_2$, 40 mg, 0.10 mmol) were mixed in ethanol and refluxed overnight. The reaction was monitored with TLC. After, the mixture product was recrystallized from EtOH. After recrystallization, the target Rh-3 (97 mg, 71%) was obtained as a pale orange solid. ^{1}H NMR (400 MHz, DMSO-d6) δ 7.83 (s, N=CH, 2H), 7.77-7.79 (m, =CH, 4H), 7.49-7.50 (m, =CH, 4H), 7.30-7.34 (m, =CH, 4H), 7.10 (m, =CH, 6H), 7.01-7.02 (m, =CH, 4H), 6.92-6.94 (m, =CH, 6H), 6.34-6.36 (m, =CH, 4H), 6.29-6.6.30 (m, =CH, 6H), 3.17-3.35 (m, CH2, 24H), 1.01-1.07 (m, CH3, 24H); APT 13C NMR (100 MHz, DMSO-d6) δ 167.4 (2C), 161.8 (2C), 153.8 (2C), 153.15, 148.8 (2C), 145.9 (2C), 143.1 (2C), 141.2 (2C), 134.4 (2C), 133.20, 131.31, 131.13, 130.9 (2C), 128.90, 128.80, 128.4 (2C), 127.9 (2C), 127.3 (2C), 124.15, 122.76, 108.56, 105.4 (2C), 97.63, 64.53, 58.69, 44.12, 41.18, 12.85; FTIR (ATR): 3428 cm^{-1} (NH), 2935 cm^{-1} (C-H stretch), 2245 cm^{-1} (C-N), 1695 cm^{-1} (O-C=O), 1614 cm^{-1} (C=N).

2.4. Photophysical Studies

2.4.1. UV-Vis and Fluorescence Studies of Probes with Various Cations and Anions

The solution of probes (1×10^{-2} M) and cations (Al^{3+}, Ca^{2+}, Cd^{2+}, Co^{2+}, Cu^{2+}, Fe^{2+}, Fe^{3+}, Hg^{2+}, Mg^{2+}, Mn^{2+}, Ni^{2+}, Zn^{2+}, and Pb^{2+} as their chloride salts, 1×10^{-2} M) / anions (($[Bu_4N]F$, $[Bu_4N]Cl$, $[Bu_4N]Br$, $[Bu_4N]I$, $[Bu_4N]AcO$, $[Bu_4N]BnO$, $[Bu_4N]HSO_4$, $[Bu_4N]ClO_4$, $[Bu_4N]CN$, $[Bu_4N]SCN$, $[Bu_4N]H_2PO_4$, $[Bu_4N]OH$, 1×10^{-2} M) were prepared in selected solvent media and H_2O, respectively. A solution of probes (5 µM) was placed in a quartz cell and the UV-Vis and fluorescence spectrums were recorded in selected solvent media. After the introduction of the solution of cations (1 equiv.), the changes in absorbance intensity were recorded at room temperature each time.

2.4.2. The Fluorescence Titration of Probes with Ions

The solution of probes (1×10^{-2} M) and ions (1×10^{-2} M) were prepared in selected solvent media and H_2O, respectively. The concentration of probe probes used in the experiments was 2 µM. The fluorescence titration spectra were recorded by adding corresponding concentration of ions to a solution of probesin selected solvent media or H_2O. Each titration was repeated at least twice until consistent values were obtained.

2.4.3. Job's Plot Measurement

Probes were dissolved in selected solvent media to make the concentration of (1×10^{-2} M). 5.00, 4.50, 4.00, 3.50, 3.00, 2.50, 2.00, 1.50, 1.00, 0.50 and 0.0 mL of the ligand solution were taken and transferred to vials. Ions were dissolved in H_2O to make the concentration of (1×10^{-2} M). 0.0, 0.50, 1.00, 1.50, 2.00, 2.50, 3.00, 3.50, 4.00, 4.50, and 5 mL of the ion's solution were added to each ligand solution. Each vial had a total volume of 5 mL. After shaking the vials for a few seconds, fluorescence spectra were taken at room temperature.

2.4.4. Determination of Detection limit

The absorption and fluorescence measurements were taken for each solution containing ions. The detection limits for ions were calculated based on the absorption and fluorescence titration. For this purpose, a $3.3\ (\mathrm{SD})\ /\mathrm{Slope}$ equation was used. Where SD is the standard deviation of blank, the slope is the fit line in fluorescence titration experiment or in absorbance titration experiment.

$$(The\ detection\ limit)\mathrm{LOD} = 3.3\ \mathrm{x}\ (\mathrm{Standard\ Deviation\ (SD)}\ /\mathrm{Slope}) \qquad (2.1)$$

2.4.5. Determination of Association Constant

Association constant was calculated according to the Benesi-Hildebrand equation by fluorescence method. Association Constant (K_a) was calculated following the equation stated below:

$$\frac{1}{A-A_0} = \frac{1}{\{K_a(A_{max}-A_0)[I^{x\pm}]^n\}} + \frac{1}{A_{max}-A_0} \qquad (2.2)$$

$$\frac{1}{F-F_0} = \frac{1}{\{K_a(F_{max}-F_0)[I^{x\pm}]^n\}} + \frac{1}{F_{max}-F_0} \qquad (2.3)$$

Here, A_0/F_0 is the absorbans/floresans of receptor in the absence of metal ion, A/F is the absorbans/floresans recorded in the presence of added metal ion, A_{max}/F_{max} is absorbans/floresans in presence of added [Mx^+] max and Ka is the association constant, where $[Mx^+]$ is ions n is the binding stoichiometry for receptor and ions. The association constant (Ka) could be determined from the slope of the straight line of the plot of $1/\,A - A_0$ or this $1/F - F_0$against $1/[I^{x\pm}]^n$.

2.4.6. The pH Measurement

The effect of different pH environments (range of 2–12) was studied for the practical application of the probe (10 µM, in EtOH) in the absence and presence of CN^- (30 µM, in H2O). For this purpose, the probe samples were prepared in ten different tubes, and cyanide ions dissolved in water were added. The pH values of samples were modulated by adding HCl or NaOH solution. pH values of the solution were monitored with a pH meter and/or pH stick.

2.4.7. Determination of Quantum Yield

In this method, the quantum yield of the compound is calculated by using a reference compound (the photophysical properties of the compound used as a reference have been fully determined) that gives a fluorescence spectrum in the emission region of the relevant compound. The Parker-Rees equation is given in 2.4 (Jagadhane et al., 2022)

$$\emptyset_s = \emptyset_r \left(\frac{D_s}{D_r}\right)\left(\frac{n_s}{n_r}\right)^2\left(\frac{1-10^{OD_r}}{1-10^{OD_s}}\right) \qquad 2.4$$

In the equation, $\boldsymbol{\emptyset_r}$ is the quantum yield of the sample and the reference, $\boldsymbol{\emptyset_s}$ is the quantum yield of the ligand, $\boldsymbol{D_r}$ and $\boldsymbol{D_s}$ are the corrected fluorescence spectrum areas of the reference and the ligand, respectively, $\boldsymbol{n_r}$ and $\boldsymbol{n_s}$ are the refractive index of the solvents of the reference and the ligand, respectively,$\boldsymbol{OD_r}$ and $\boldsymbol{OD_s}$are the optical densities of the reference and ligand measured at the excitation wavelength, respectively.

3. RESULTS and DISCUSSION

3.1. Chemistry

3.1.1. Synthesis of PPs

In this part, we synthesized novel phenolphthalein-based probes (**PPs**) (Figure 3.1). First, we reacted phenolphthalein (**PP**) with hexamethylenetetramine (**HMTA**) in trifluoroacetic acid (TFA) to obtain the output compound PP-CHO (2). Then, we synthesized **PP-1** and **PP-2** from **PP-CHO** and 3-methoxybenzene hydrazide or 2-(1*H*-indol-3-yl) acetohydrazide, respectively, in ethanol (Figure 3.1). The characterization of the synthesized probes PPs was carried out using ^{1}H-NMR / ^{13}C-NMR and mass spectroscopy techniques. Upon examination of the ^{1}H-NMR spectrum of the **PPs** probes, the resonance at 9.85 ppm corresponding to the aldehyde peak in the **PP-CHO** structure vanishes. Moreover, when the ^{1}H-NMR spectrum is examined, it is also seen that the NH_2 peak in the structure of R-NH-NH_2 has disappeared (Figure Ap.1-Ap.4).

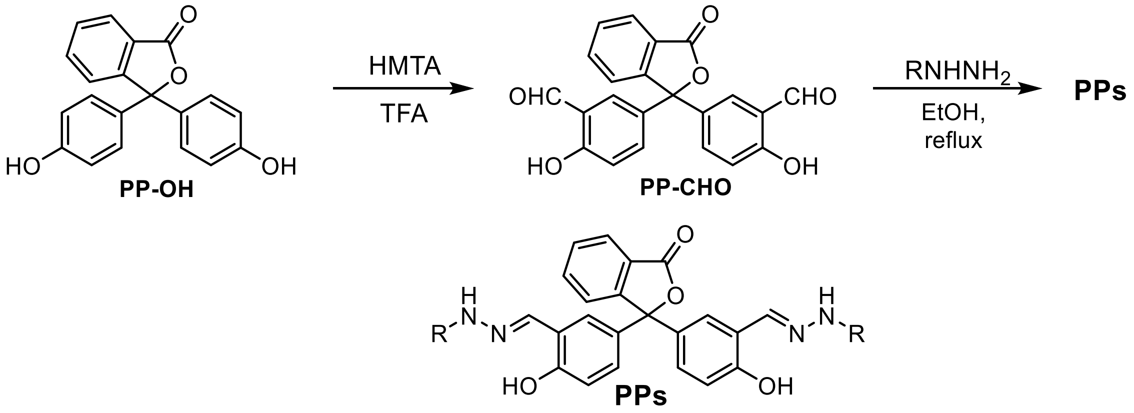

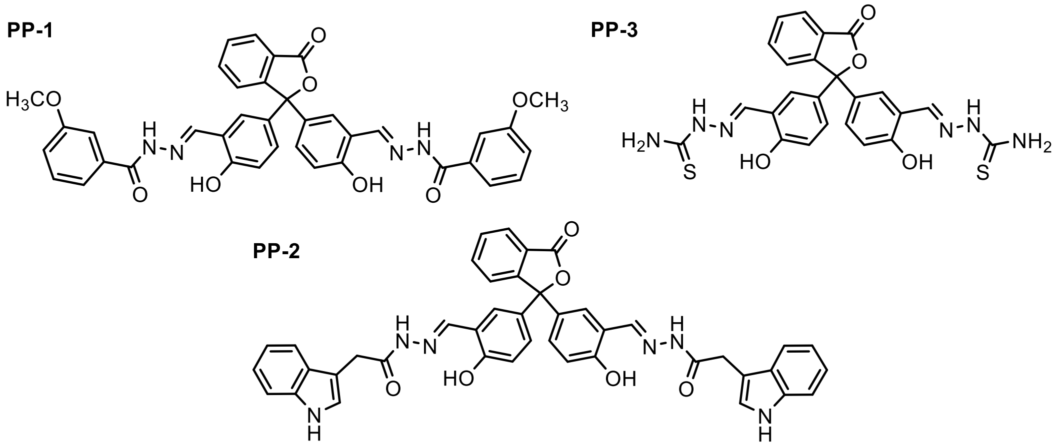

Figure 3.1. The synthesis approach of the PPs probes

3.1.2. Synthesis of Rhs

The objective of this thesis study is to develop novel retrievable rhodamine-based probes (**Rhs**) that can be utilized repeatedly in aqueous solvent systems, inspired by this background. In our research, the novel multi-probes, Rhs, were synthesized by distinct indicators of rhodamine (**Rh**) and selected aldehydes or ketones within a singular structure. To achieve this objective, initially, the output compound Rh-NH_2 was obtained from the reaction of rhodamine B with ethylenediamine in ethanol at reflux temperature, as described in the experimental part. After synthesizing the output compound Rh-NH_2 as described in the literature, the final target Rhs probes were carried out in EtOH without any catalyst at the reflux temperature of ethanol (Figure3.2). Similarly, upon examination of the ^{1}H-NMR spectrum of the Rh-NH_2, the resonance at around 9.50 ppm corresponding to the aldehyde peak in the RCHO structure vanishes. Moreover, when the ^{1}H-NMR spectrum is examined, it is also seen that the NH_2 peak in the structure of Rh-NH_2 has disappeared (Figures Ap.5-Ap.9).

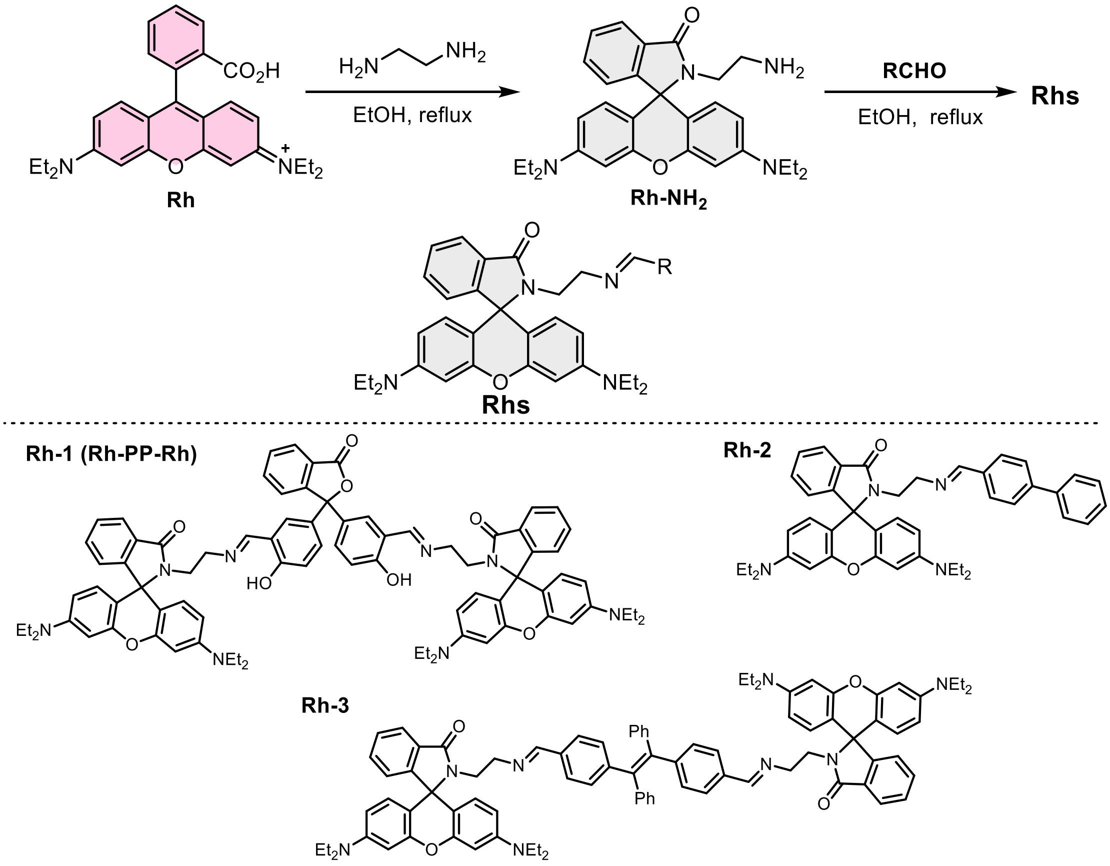

Figure 3.2. The synthesis approach of the Rhs probes

3.2. Photochemical Studies

3.2.1. Selectivity and Sensitivity Studies of PP-1

Following the synthesis of **PP-1**, in this part of the thesis, we studied how **PP-1** interacts with various metal ions using a mixture of ethanol and HEPES buffer (1:1 ratio, pH 7). The **PP-1** solution's absorption properties changed significantly upon adding certain ions, however, these changes weren't specific to any particular metal. As seen in (Figure 3.3A), **PP-1** showed weak absorption in the range of 360-420 nm, indicating it remained in its closed form. Interestingly, adding metal ions caused a noticeable increase in absorption intensity. Following these observations, we examined the fluorescence behavior of **PP-1** with and without metal ions using an excitation wavelength of 390 nm (Figure 3.3B) Adding 30 μM of various metal ions generally didn't affect fluorescence intensity, except for Zn^{2+}, Cd^{2+}, and Al^{3+}. These three ions specifically triggered significant fluorescence increases at 453 nm (Al^{3+}), 493 nm (Cd^{2+}), and 501 nm (Zn^{2+}). These results suggested that **PP-1** could selectively detect Al^{3+}, Cd^{2+}, and Zn^{2+} using fluorescence. However, its ability to detect all three ions simultaneously limits its practical applications. Therefore, we further investigated the selectivity of **PP-1** at different pH levels. We measured the fluorescence spectrum of **PP-1** in ethanol/water (v/v: 1/1) with and without each metal ion across a pH range of 2.0 to 12.0 (Figure 12A). Notably, **PP-1** did not produce a fluorescence peak at any pH value tested, indicating its stability and dominance of the spirocyclic form. Investigating selectivity at pH 5 and 9 revealed some interesting findings. As the solution's pH changed from 2.0 to 12.0, the fluorescence intensity of **PP-1** increased 80-fold for Al^{3+} at pH 5 (Figure 3.3C) and 60-fold for Zn^{2+} at pH 9 (Figure 3.3D). This suggests high selectivity for Al^{3+} only at pH 5, not for other ions. The optimal pH range for selectivity of **PP-1** towards Al^{3+} appears to be 5.0–7.0, with the strongest response at pH 5. This suggests a strong complex formation between **PP-1** and Al^{3+} due to a phenomenon called CHEF. The fluorescence intensity increase can be attributed to the suppression of both ICT and C=N isomerization processes. Interestingly, the blue shift in fluorescence intensity indicates a strong interaction between the probe and Al^{3+}ions. Conversely, adding Al^{3+} ions at basic conditions resulted in almost no change in fluorescence, likely due to Al^{3+}hydrolysis at higher pH. Other cations had minimal impact on the fluorescence intensity of **PP-1** at pH 5. Finally, the study demonstrates that **PP-1** exhibits high selectivity towards Zn^{2+} at pH 9, with a clear "turn-on" fluorescence response. The observed fluorescence enhancement can be explained by suppressed C=N isomerization (rotation) and ICT processes in the Schiff base structure of **PP-1**. However, this effect is specific to Al^{3+} at pH 5 and doesn't apply to other cations at pH 9. In acidic environments, **PP-1** loses selectivity for Zn^{2+} because the probe **PP-1** becomes protonated, causing the complex to dissociate. Following this, we also investigated Cd^{2+} selectivity across a pH range of 2.0 to 12.0 in an ethanol-water mixture (Figure Ap.12). We found no selectivity for Cd^{2+} in this medium. Interestingly, selectivity for Cd^{2+} was observed at pH 7 when HEPES buffer was present (Figure 3.3B), but not at other pH values or without HEPES. This suggests that HEPES is essential for **PP-1** to detect Cd^{2+} at pH 7. Overall, these results demonstrate that **PP-1** exhibits high selectivity for Al^{3+}, Cd^{2+}, and Zn^{2+}, but in a pH-dependent manner. Al^{3+} detection is specific to pH 5, while Cd^{2+} requires HEPES at pH 7. Additionally, Zn^{2+} selectivity is observed at pH 9.

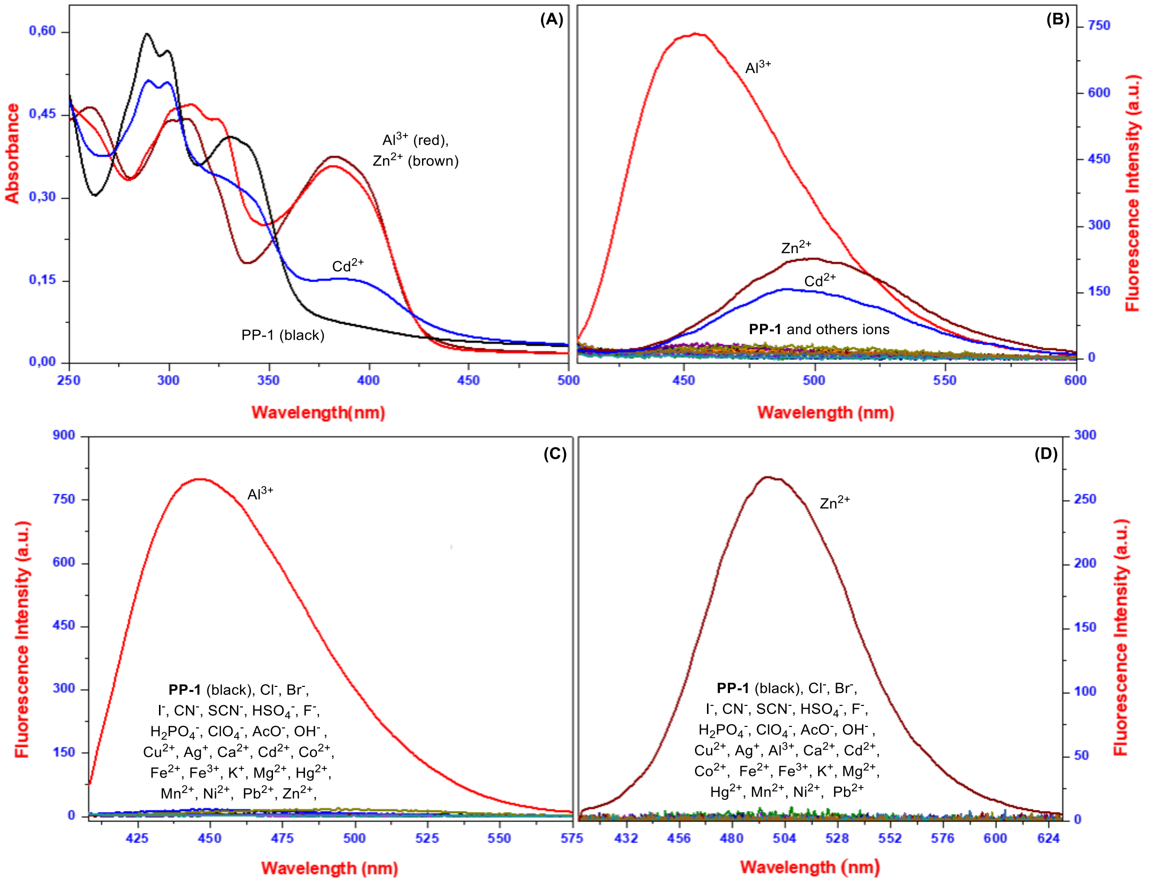

Figure 3.3. The UV-Vis and fluorescence spectrums of PP-1 in the absence and presence of ions in EtOH/HEPES buffer (v/v: 1/1) at pH 7 (**A** and **B**), pH= 5 (**C**) and pH 9 (**D**)

To further investigate the probe's ability to sense specific ions, we performed fluorescence titration experiments. First, we tested **PP-1** (10 µM) with Al^{3+}, Zn^{2+}, and Cd^{2+} at pH 5, pH 9, and pH 7 (with HEPES buffer), respectively (Figure 3.3B, C and D) As we gradually added Al^{3+} to the pH 5 solution of **PP-1**, the fluorescence intensity steadily increased, reaching a maximum with 1.25 equivalents of Al^{3+} (Figure 3.4A and A′). Similar trends were observed when adding Zn^{2+} and Cd^{2+} to the pH 9 and pH 7 (with HEPES buffer) solutions of **PP-1**. The emission intensity at around 500 nm increased proportionally with the selected ion concentration, reaching a maximum at 0.125 and 0.456 equivalents of Zn^{2+} and Cd^{2+} added, respectively. This allowed for the calculation of the detection limits of P**P-1** to be 33 nM for Al^{3+}, 64 nM for Zn^{2+}, and 550 nM for Cd^{2+} (Figure 3.4B, B' and C, C'). These values are lower than those of some previously reported fluorescent probes for these ions (World Health, 2008 and 2011).

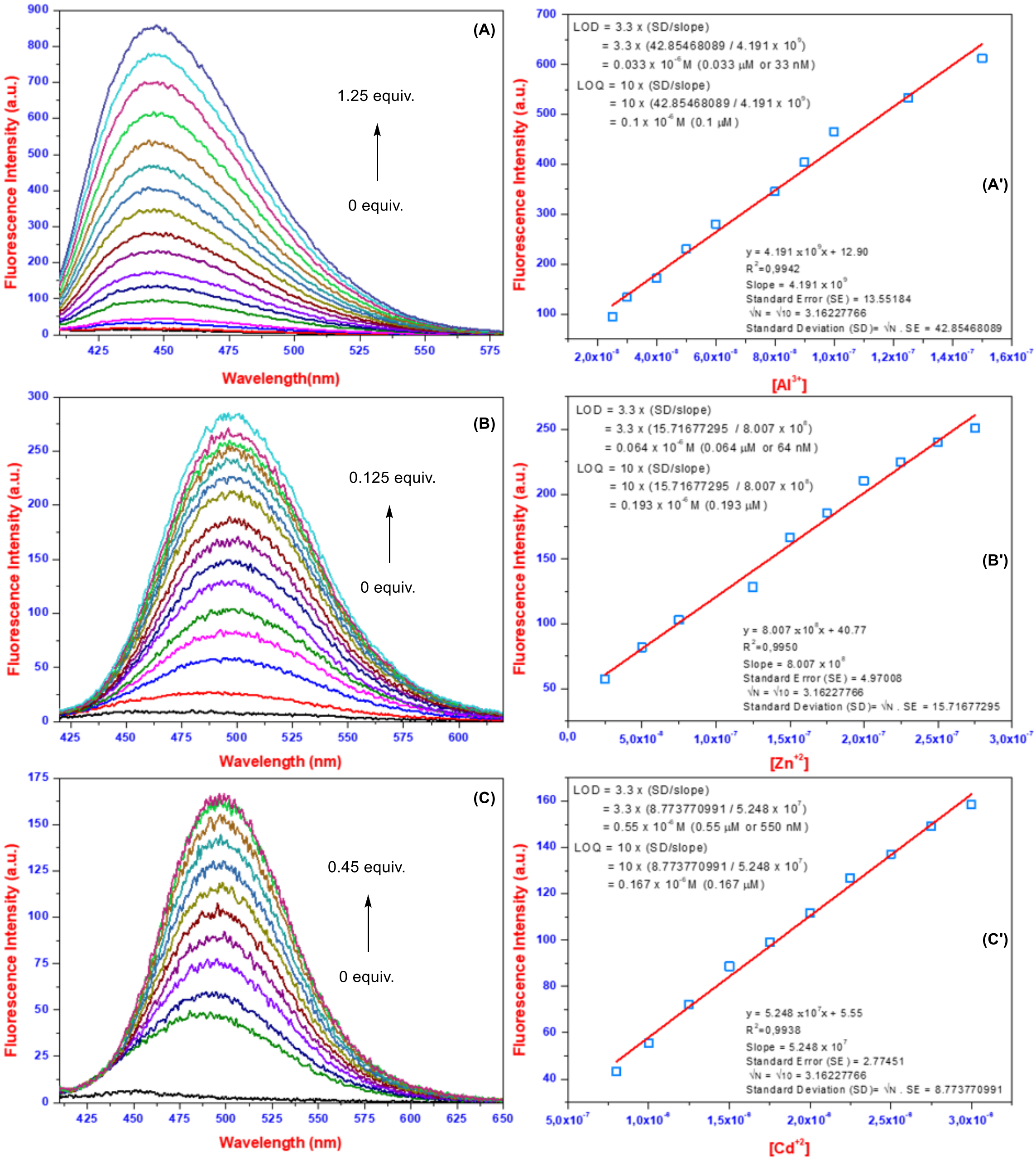

Figure 3.4. The fluorescence titration and change intensity of the PP-1 with the increasing concentration of $AlCl_3$ (**A** and **A'**), $ZnCl_2$ (**B** and **B'**), and $CdCl_2$ (**C** and **C'**)

Following, we further investigated the interaction (complexation) between **PP-1** and Al^{3+}, Zn^{2+} using Job's plot analysis (Figures Ap.13). This analysis revealed a 1:2 binding stoichiometry for three ions with **PP-1** (Figure 3.5.A-C). Following this, they calculated the binding constants (K_a) of **PP-1** with Al^{3+} at pH 5, Zn^{2+} at pH 9, and Cd^{2+} at pH 7 using the Benessi-Hildebrand equation. The resulting values were 2.68 x 10^{14} M^{-2}, 6.15 x

10^{14} M^{-2}, and 5.49 x 10^{15} M^{-2}, respectively, indicating high sensitivity detection of Al^{3+}, Zn^{2+}, and Cd^{2+} by **PP-1** depending on pH (Figure 3.5.A'-C').

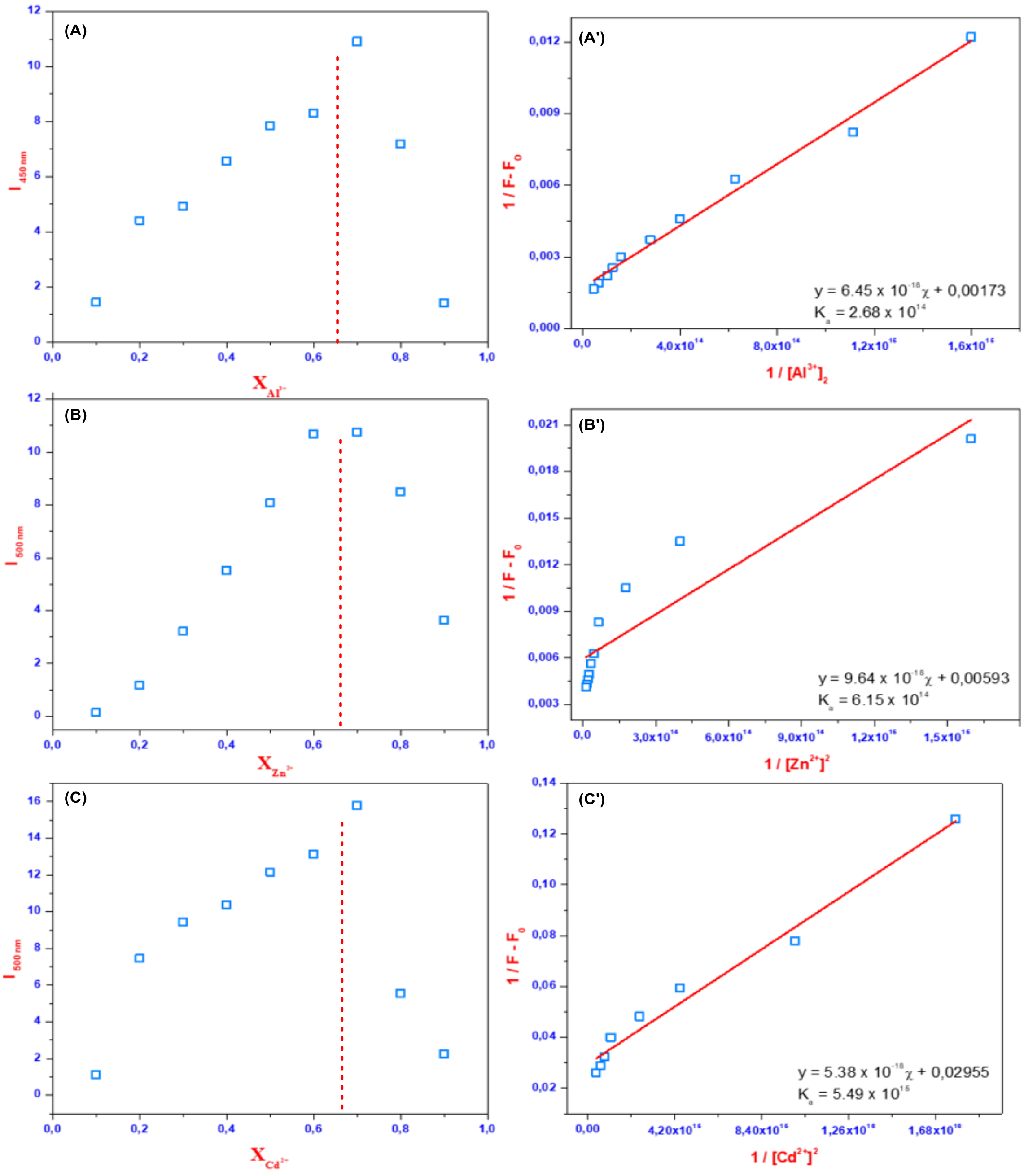

Figure 3.5**.** Job’s and Benesi–Hildebrand plots based on a 1:2 association stoichiometry of PP-1 with $AlCl_3$ (**A** and **A'**), $ZnCl_2$ (**B** and **B'**), and $CdCl_2$ (**C** and **C'**)

Competitive experiments are crucial in sensor development to ensure reliable and specific ion detection. These experiments assess how other ions might interfere with the desired detection of Al^{3+} and Zn^{2+} by **PP-1**. In this context, we also conducted these experiments at pH 5 for Al^{3+} (Figure 3.6A) and pH 9 for Zn^{2+} (Figure 3.6B). In the Al^{3+} detection (pH 5), most ions had minimal impact on the fluorescence intensity of the PP-1+Al^{3+} complex. However, OH caused a slight decrease in fluorescence. This suggests that **PP-1** can function as an effective fluorescent sensor for Al^{3+} at pH 5, even in the presence of most competing metal ions. For Zn^{2+} detection at pH 9, the presence of other ions did cause some interference, resulting in a lower overall fluorescence response of the PP-1+Zn^{2+} complex. Nevertheless, detectable fluorescence remained even with competition, indicating potential for Zn^{2+} detection at pH 9 using **PP-1**. Overall, these competitive experiments highlight the promise of **PP-1** as a sensor for Al^{3+} at pH 5 and Zn^{2+} at pH 9, although some limitations exist in Zn^{2+} detection due to interference.

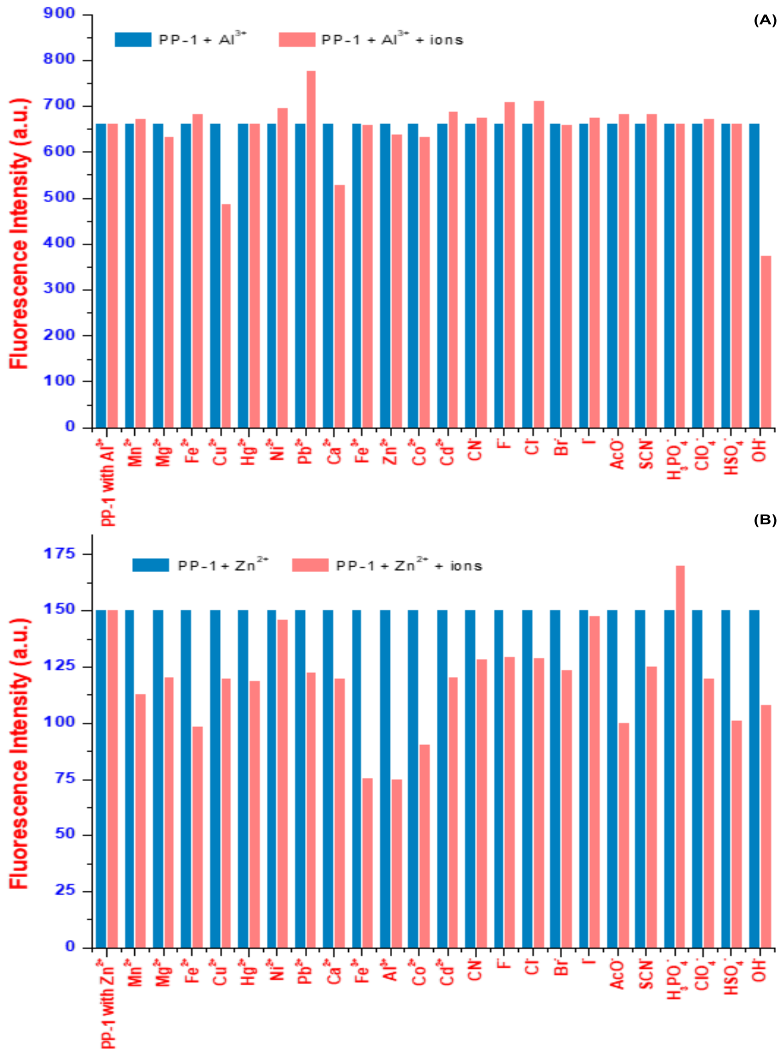

Figure 3.6. Fluorescence bar graphs of PP-1 in the presence of Al^{3+} (**A**) and Zn^{2+} (**B**) upon the addition of different ions

Another crucial factor for practical use is a probe's reversible binding property, indicating stability and reusability. Here, we also evaluated the reversibility of **PP-1** by exposing PP-1+Al^{3+} complexes (in a 1:1 ethanol-water medium) to various anions. The addition of $[Bu_4N]OH$ caused a decrease in the fluorescence intensity of the PP-1+Al^{3+} complex (Figure 3.7 and Ap.14). Interestingly, this process could be repeated for up to five cycles before a significant drop in fluorescence intensity. This suggests that **PP-1** exhibits reversible binding behavior for aluminum detection, allowing for potential reuse.

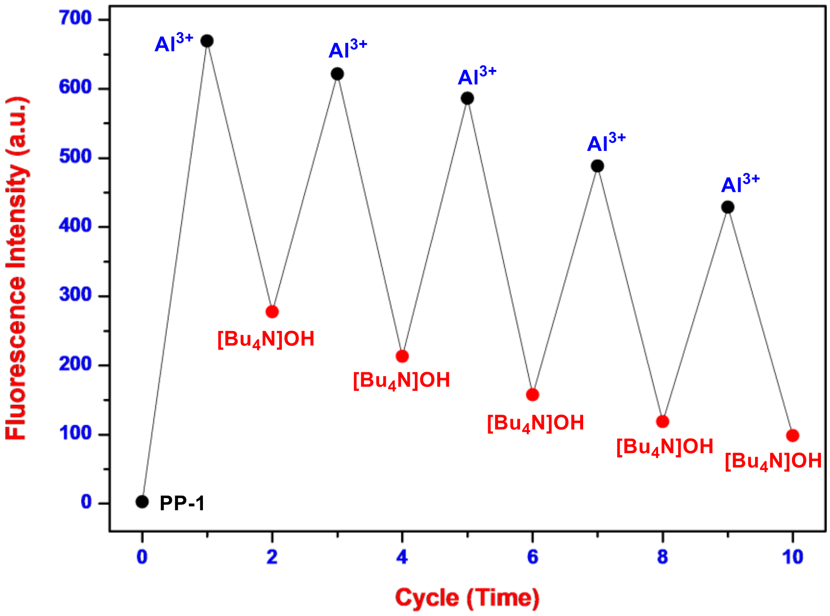

Figure 3.7. The reversible switching of the fluorescence intensity of PP-1-Al^{3+} with $[Bu_4N]OH$

In this part of the thesis, we conducted theoretical simulations employing Gaussian 09 W software on how **PP-1** binds to Al^{3+} and Zn^{2+} ions. First, we optimized the structures of **PP-1**, and its complexes with Al^{3+} and Zn^{2+} (PP-1+Zn^{2+} and PP-1+Al^{3+}), using a method called DFT. Different levels of detail were used for calculations depending on the atom. Then, we analyzed the TD-DFT to see how the electrons move when light interacts with the molecule. (Figure 3.8) shows the optimized structures and how the electrons are distributed in **PP-1** and its complexes. As the figure shows, the energy gap between the key orbitals (HOMO and LUMO) in **PP-1** is relatively large (*around 3.98 eV*). Interestingly, this gap gets smaller in the complexes with Al^{3+} and Zn^{2+}. A smaller gap suggests a stronger interaction between the metal ions and the **PP-1** molecule, which supports the idea that **PP-1** effectively binds these metal ions.

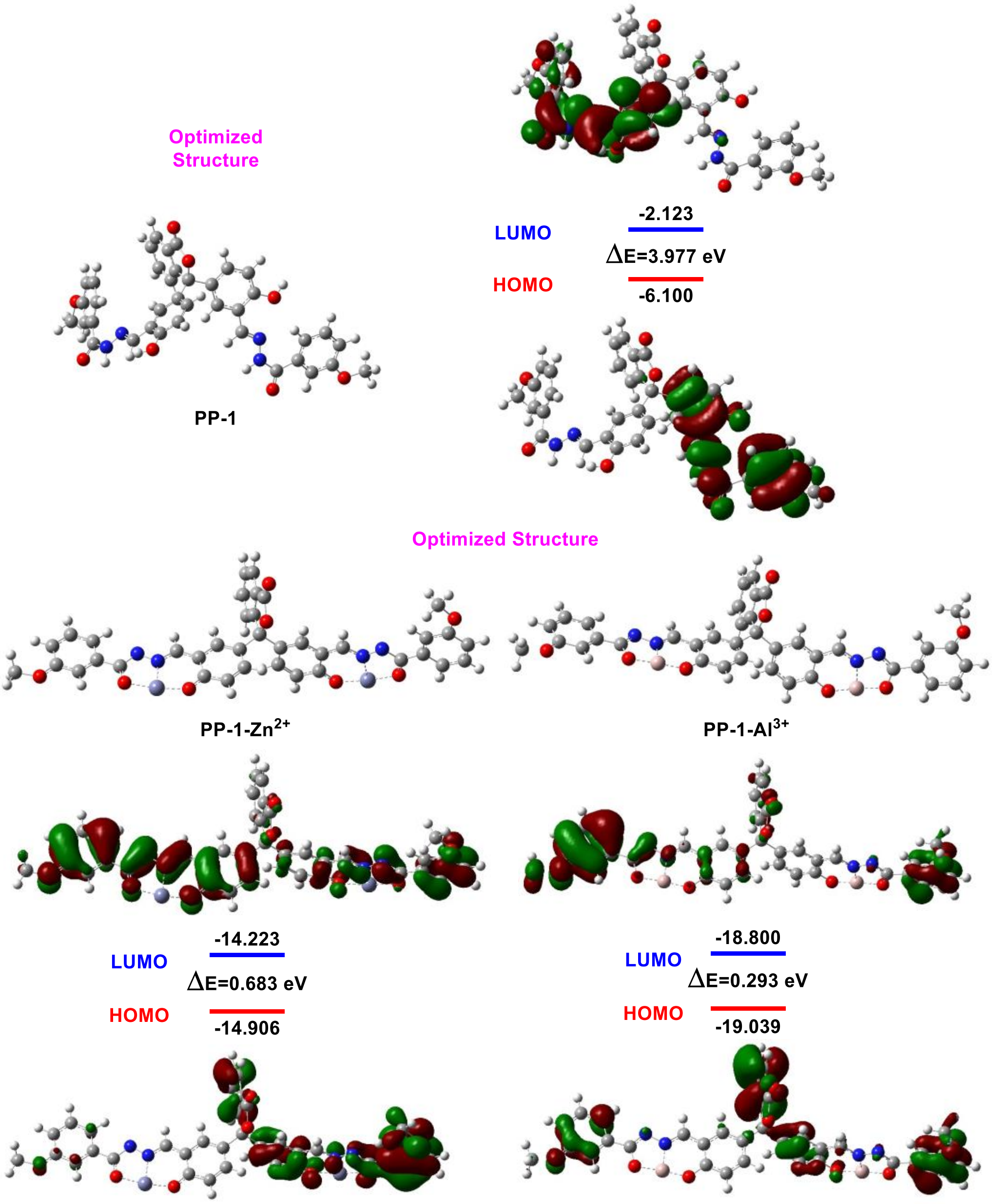

Figure 3.8. Ground-state optimized structures and HOMO/LUMO energy gap of PP-1, and PP-1(M)$_2$

Following spectral studies of **PP-1**, we used real-world water samples (tap, ground, and drinking water) to assess the effectiveness of **PP-1** in practical applications. For this purpose, we investigated how well **PP-1** worked in real water by spiking tap, ground, and drinking water with different concentrations of Al^{3+} and Zn^{2+}+ ions. Fluorescence spectroscopy was then used to analyze the samples. The presence of Al^{3+} and Zn^{2+} in all three water types was confirmed by the analysis (Tables 3.1 and 3.2). Additionally, the results showed recoveries ranging from 97.0% to 105.3% and relative standard deviation

(RSD) values below 4.8%. These findings demonstrate the high accuracy of **PP-1** as a probe for detecting Al^{3+} and Zn^{2+}ions in real water samples. As a result, it can be said that probe **PP-1**, which was tested on real samples in the light of spectral data, is an effective pH-sensitive sensor candidate for aluminum, Zn^{2+}, and cadmium.

Table 3.1. Analytical results for determination of Al^{3+} in real water samples at pH 5

Sample	**Al^{3+}added (µmolL^{-1})**	**Al^{3+}found (µmolL^{-1})**	**Recovery (%)**	**RSD (%) (n= 3)**
	0.00	0.16824 ±0.0033	0.00	2.03
Tap Water	0.04	0.21424 ±0.0041	102.88	1.698
	0.08	0.24886 ±0.0091	99.2	3.184
	0.00	0.09803 ±0.0045	0.00	4.571
Ground Water	0.04	0.13895 ±0.0038	100.6	2.411
	0.08	0.1864 ±0.0010	104.7	0.536
	0.00	0.06556 ±0.0036	0.00	4.740
Bottled Water	0.04	0.09821 ±0.0044	99.5	4.177
	0.08	0.14901 ±0.0040	102.3	2.443

Table 3.2. Analytical results for determination of Zn2+ in real water samples at pH=9

Sample	**Zn^{2+}added (µmolL^{-1})**	**Zn^{2+}found (µmolL^{-1})**	**Recovery (%)**	**RSD (%) (n= 3)**
	0.00	0.2329 ±0.0073	0.00	2.760
Tap Water	0.04	0.4270 ±0.0176	98.5	3.583
	0.08	0.6502 ±0.0097	102.7	1.462
	0.00	0.1328 ±0.0006	0.00	0.464
Ground Water	0.04	0.3246 ±0.0022	95.2	4.057
	0.08	0.541 ±0.0091	100.2	1.680
	0.00	0.0616 ±0.0017	0.00	2.513
Bottled Water	0.04	0.2833 ±0.0052	101.4	1.788
	0.08	0.4668 ±0.0067	100.6	1.259

3.2.2. Selectivity and Sensitivity Studies of PP-2

Following the photophysical studies of **PP-1** and the synthesis of **PP-2**, similarly, we studied how **PP-2** interacted with different metal ions in EtOH/HEPES (v/v:1/1, pH 7). We looked at how the absorbance and fluorescence of **PP-2** changed when ions were added. Adding ions significantly changed the way **PP-2** absorbed light. However, these changes didn't distinguish between specific ions. (Figure Ap.15A) shows that **PP-2** weakly absorbed light between 360 and 425 nm in the solution, indicating it remained closed. Interestingly, adding ions caused a significant increase in light absorption. Based on these absorption changes, we also examined how **PP-2** fluoresced in the absence and presence of ions (using an excitation wavelength of 390 nm (Figure Ap.15), As expected, **PP-2** itself barely emitted any light, likely due to a combination of factors like internal charge transfer, molecular isomerization, and energy transfer. However, in the presence of zinc, the intensity of emitted light by **PP-2** at 494 nm significantly increased (Figure 3.9A). These results showed that **PP-2** selectively detected Zn^{2+} ions in EtOH/HEPES (v/v:1/1, pH 7) using fluorescence. At this stage, to see how water affected this selectivity, we also measured fluorescence at three different water concentrations. For this purpose, we added various ions (5μM) to **PP-2** in the related solution. Interestingly, PP-2 only showed selectivity for cadmium ions in EtOH/H_2O (v/v:9/1) (Figure 3.9B). These results suggest that PP-2 can selectively bind to either Zn^{2+} or Cd^{2+}, depending on the water content in the solution. In other words, while only cadmium ions are specifically determined in solutions with a high ethanol content, as the water content increased, **PP-2** could detect both zinc and cadmium ions.

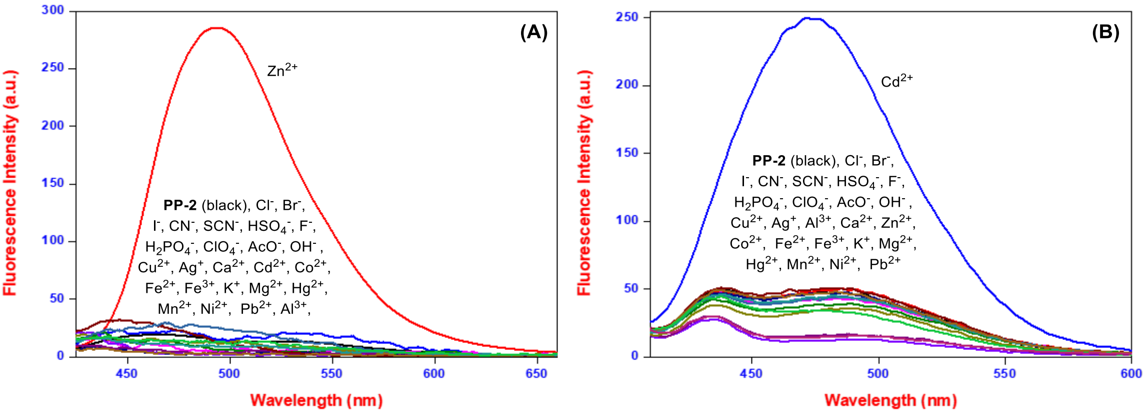

Figure 3.9. The fluorescence spectral changes of PP-2 (10 μM) upon the addition of ions (30 μM) in EtOH/HEPES (v/v:1/1, at pH 7) (**A**) and EtOH/H_2O (v/v:9/1, at pH 9) (**B**)

Following general spectroscopic studies, we investigated how well the probes detected chemicals (chemosensing properties) using fluorescence titration experiments. For this purpose, we titrated **PP-2** with Zn^{2+} and Cd^{2+} ions in EtOH/H_2O (v/v: 1/1 for Zn^{2+} and 9/1 for Cd^{2+}). When we gradually added Zn^{2+} to **PP-2** in EtOH/H_2O (v/v:1/1), the light emission intensity increased six-fold, peaking at 469 nm. This increase reached a maximum level (saturation) after adding 8.0 equivalents of Zn^{2+} (Figure 3.10A). In the experiment with Cd^{2+}, we titrated **PP-2** with up to 1.50 times its amount in EtOH/H2O (v/v:9/1). This caused a threefold increase in fluorescence intensity, with a new emission peak at 471 nm. Similar to Zn^{2+}, the emission intensity reached saturation after adding 1.50 equivalents of Cd^{2+} (Figure 3.10B). The detection limits of **PP-2** were determined to be 550 nM for Zn^{2+} and 15 nM for Cd^{2+} (Figures 3.10A' and 3.10B'). Notably, these values are lower than those reported for some existing fluorescent probes designed to detect these specific ions (World Health, 2008 and 2011).

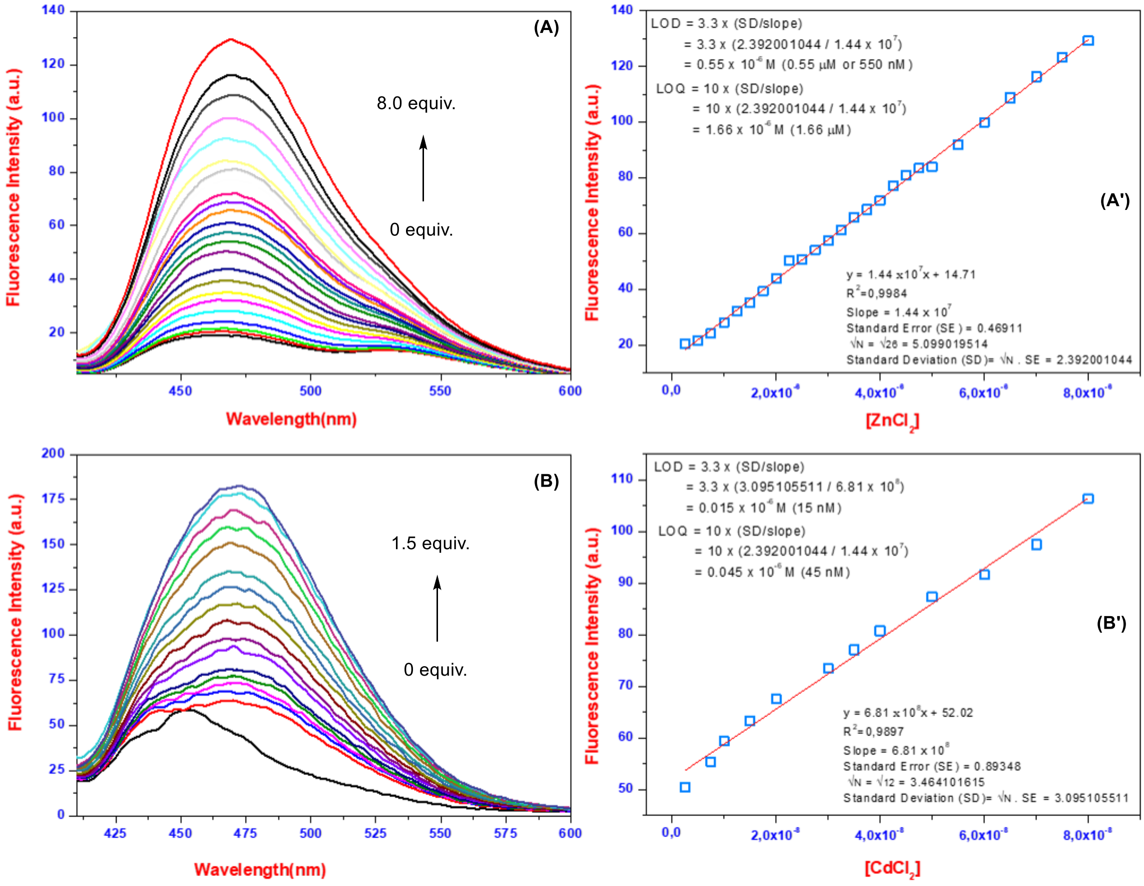

Figure 3.10. The fluorescence titration and change intensity of the PP-2 with the increasing concentration of $ZnCl_2$ (**A** and **A'**), and $CdCl_2$ (**B** and **B'**)

Job's plot analysis confirmed a 1:2 binding stoichiometry between **PP-2** and both Zn^{2+} and Cd^{2+} (Figure 3.11A and 3.11B). This means that two metal ions bind to each PP-2. Subsequently, the binding constants (K_a) of **PP-2** with Zn^{2+} and Cd^{2+} were calculated using the Benessi-Hildebrand equation. The resulting values, 1.31 x 10^{17} M^{-2} and 4.23 x 10^{14} M^{-2} for Zn^{2+} and Cd^{2+} respectively indicate high affinity binding, suggesting the potential of **PP-2** for sensitive detection of these metal ions (Figure 3.11A′ and 3.11B′).

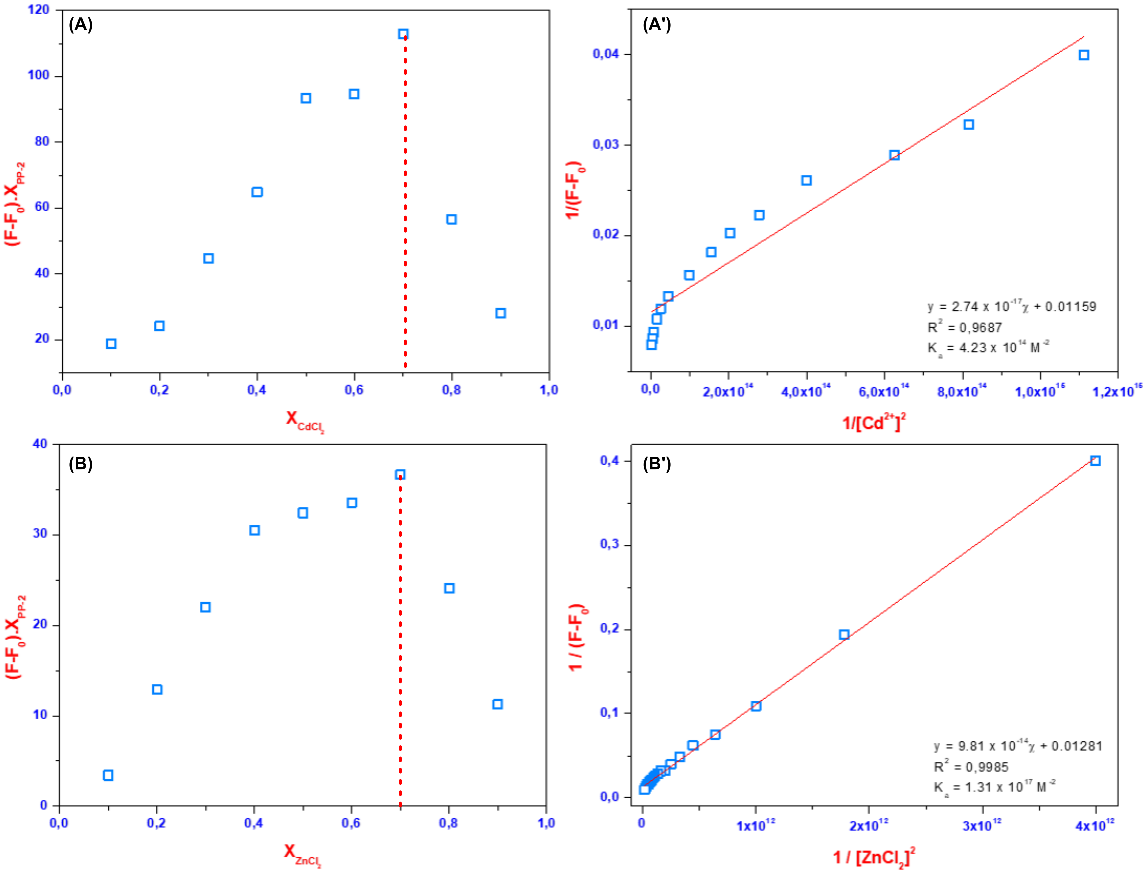

Figure 3.11. Job's and Benesi–Hildebrand plots based on a 1:2 association stoichiometry of PP-2 with $CdCl_2$ (**A** and **A'**), and $ZnCl_2$ (**B** and **B'**)

Competitive experiments were conducted to evaluate the selectivity of the **PP-2** sensor for Cd^{2+} and Zn^{2+} ions (Figure 3.12). These experiments revealed that PP-2+Cd^{2+} exhibited high selectivity for Cd^{2+} in the EtOH/H_2O (v/v:9/1) solution. Interestingly, the presence of most tested anions had minimal impact on the fluorescence intensity of the PP-2+Cd^{2+} complex. However, $[Bu_4N]CN$ and $[Bu_4N]SCN$ caused a significant decrease in fluorescence (Figure 3.12B). This quenching effect is likely caused by the high affinity of $[Bu_4N]CN$ and $[Bu_4N]SCN$ for Cd^{2+}, leading them to compete with **PP-2** for binding to the metal ion. In contrast, PP-2+Zn^{2+} displayed selectivity for Zn^{2+} in the EtOH/H_2O (v/v:1/1) solution but was susceptible to quenching by $[Bu_4N]OH$ ions. These findings suggest that **PP-2** can be a selective sensor for Cd^{2+} and Zn^{2+} under specific conditions.

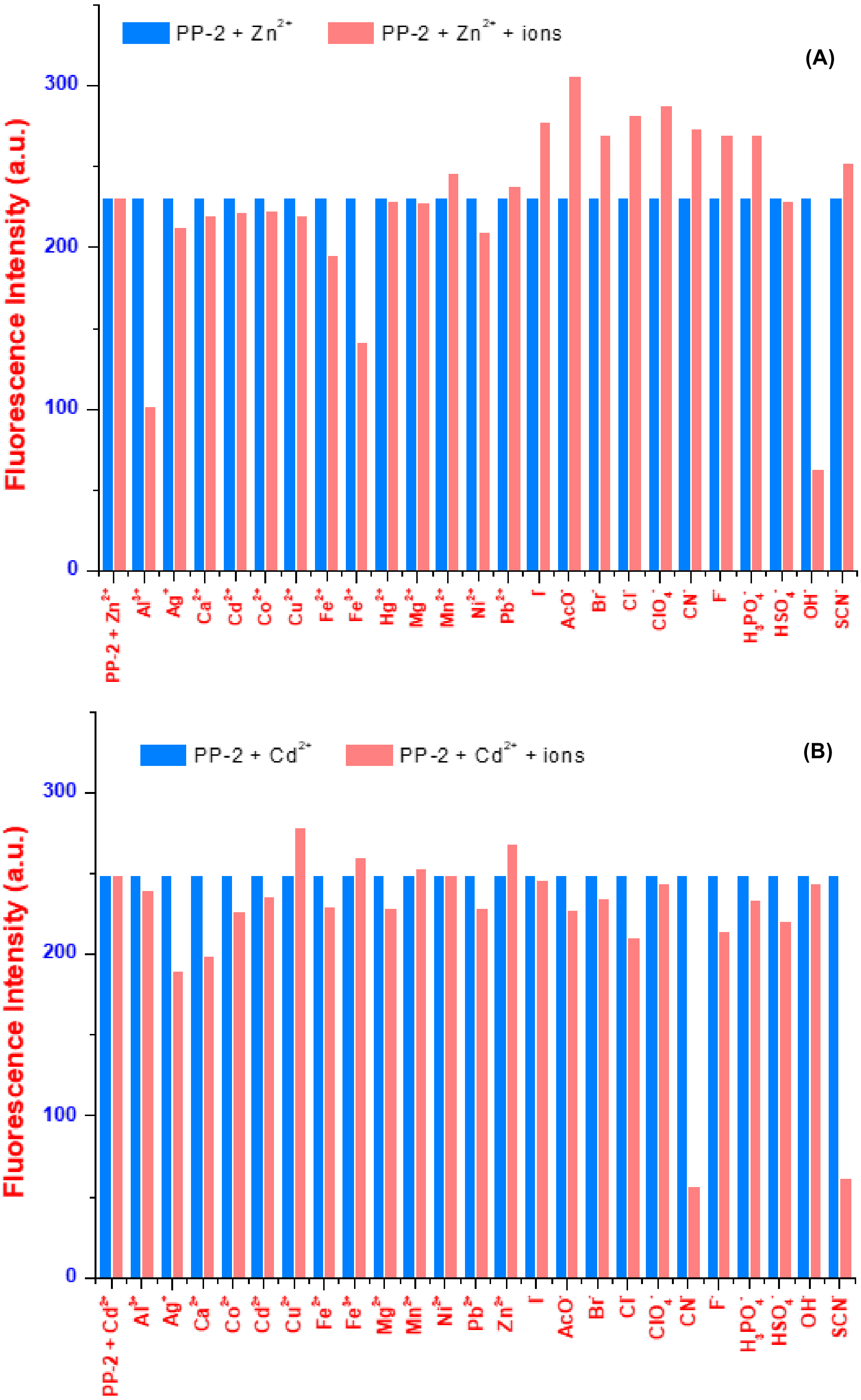

Figure 3.12. Fluorescence bar graphs of PP-2 in the presence of Zn^{2+} (**A**) and Cd^{2+} (**B**) upon the addition of different ions

In all UV-Vis and fluorescence studies, **PP-2** showed a specific response to cadmium ions only in EtOH/H_2O (v/v:9/1). Interestingly, adding CN^{-} or SCN^{-} ions caused the fluorescence to turn off. This distinct on/off switching behavior makes the PP-2+ Cd^{2+}

complex a promising candidate for detecting both cyanide and thiocyanate ions. To determine the amount of cyanide or thiocyanate present, we performed similar experiments as before, gradually adding increasing concentrations of these ions. As expected, the fluorescence intensity of the PP-2+Cd^{2+} decreased as we added more cyanide or thiocyanate, reaching a point where it couldn't decrease further (saturation) at around 3.0 µM for cyanide and 4.5 µM for thiocyanate (Figures 3.13A and 3.13B). Using this data, we calculated the LOD and LOQ for detecting cyanide and thiocyanate using PP-2+Cd^{2+} in this solvent system. The LOD was determined to be 729 nM for cyanide and 1.44 µM for thiocyanate. Similarly, the LOQ was 1.51 µM for cyanide and 4.35 µM for thiocyanate (Figures 3.13A' and 3.13B'). These results indicate that the PP-2+Cd^{2+} effectively functions as a quantitative tool to measure cyanide and thiocyanate ion concentration in EtOH/H_2O (v/v:9/1).

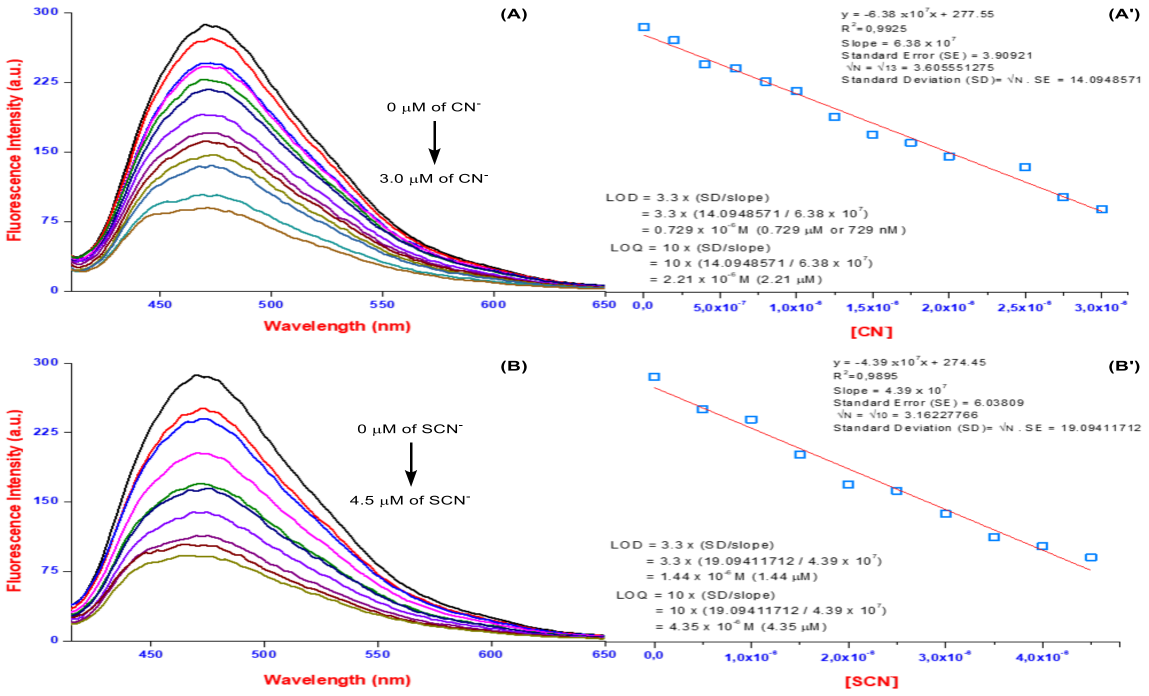

Figure 3.13. The fluorescence titration spectra of PP-2+Cd^{2+} in the presence of CN^{-} (**A**) / SCN^{-} (**B**), and the change in fluorescence intensity of the PP-2+Cd^{2+} with the increasing concentration of CN^{-} (**A'**) / SCN^{-} (**B'**)

To assess its real-world applicability, **PP-2** was tested for Cd^{2+} detection in cigarette smoke extract. A popular cigarette brand was smoked using a low-pressure setup described in (Scheme Ap.15C), and the smoke was collected in a 50 mL EtOH/H_2O (v/v:9/1) solution in a conical flask. The fluorescence intensity of the cigarette smoke extract with **PP-2** was then measured upon the addition of Cd^{2+} ions (Figure Ap.15B). This experiment demonstrated that **PP-2** can effectively detect Cd^{2+} in cigarette smoke. Further studies explored the practical utility of **PP-2** by adding varying concentrations of Cd^{2+} to the extract, with the results summarized in (Table 3.3).

Table 3.3. Analytical results for determination of Cd^{2+} in cigarette smoke extract

Sample	**Cd^{2+}Added (μ moll^{-1})**	**Cd^{2+}Found (μ moll^{-1})**	**Recovery (%)**	**RSD (%) (N= 3)**
Cigarette Smoke Extract	0.00	0.0785 ±0.0017	0.00	2.094
	0.10	0.1668 ±0.0011	98.5	0.631
	0.15	0.2346 ±0.0029	102.7	1.626
	0.20	0.2946 ±0.0081	94.2	2.413
	0.30	0.3817 ±0.0064	100.2	1.651

The recoveries ranged from 94.2 to 102.7% with good reproducibility (relative standard deviation, RSD, max 2.413). These results demonstrate that **PP-2** can effectively detect Cd^{2+} in real-world samples. Overall, the probe **PP-2** exhibited an excellent fluorescence response to Cd^{2+} and Zn^{2+} in these samples, indicating its potential for practical applications.

3.2.3. Selectivity and Sensitivity Studies of PP-3

After successfully synthesizing **PP-3** as a probe, preliminary UV-Vis studies were first performed to understand probe sensing properties. To achieve this, some adsorption studies were conducted in both EtOH/H_2O and in an aqueous medium containing HEPES systems, recognized in the literature as widely used and environmentally preferable solvent systems. To gain a comprehensive understanding of **PP-3** interaction with various metal ions, the UV-Vis absorption spectra of **PP-3** (10 µM) were analyzed at room temperature in an aqueous medium with HEPES. The absorption spectra revealed discernible bands, showing a broad feature starting at 390 nm, extending through 360 nm, and ending around 300 nm. UV spectra were captured one minute after introducing two equivalents of each specific ion (30 µM) and are depicted in (Figure 3.14A). UV-Vis analyses in an aqueous medium with HEPES revealed that the absorption band of **PP-3** at 390 nm appeared in the presence of Cu^{2+} ions, while at 360 nm, it emerged in the presence of Hg^{2+}ions (Figure 3.14A). After absorption studies, comprehensive spectroscopic investigations were conducted, including fluorescence assessments to evaluate **PP-3** effectiveness as a fluorescent cation sensor following UV-Vis analysis research (Figure 3.14B). For this purpose, fluorescence studies on the interaction between Cu^{2+} and Hg^{2+} with **PP-3** were carried out in aqueous solutions of individual pure organic solvents (TFA, MeOH, EtOH, CH_3CN, and DMSO), each in a ratio of five and nine volumes of water containing HEPES. A thorough solvent examination enables us to establish optimal conditions for the interaction between Cu^{2+} and $Hg^{2+}$with **PP-3**. This is crucial for obtaining precise colorimetric and spectroscopic data, and essential for devising improved methodologies to detect and quantify Cu^{2+} and Hg^{2+}in compatible solvent systems, leading to enhanced accuracy and efficiency. Interactions between **PP-3** and ions like Cu^{2+} and Hg^{2+} were observed in an aqueous medium with HEPES and EtOH/H_2O solvents, while no interactions were observed in other aqueous solvents such as MeOH/H_2O, CH3CN/H_2O, DMSO/H_2O, and THF/H_2O (Figure 3.14D and Ap.18). On the other hand, increasing the percentage of water heightened the intensity of the **PP-3** sensor. However, the addition of Cu^{2+} and Hg^{2+}ions to the aqueous medium resulted in the attenuation of sensing intensity. Hence, adopting a water-centric approach is advisable for optimal outcomes (Figure 3.14C and Ap.18G). The cumulative results of these studies converge on determining that the optimal solvent system for research is water, also taking into account its toxicological effects compared to alternative solvents. The fluorescence emission spectra of **PP-3** (10 μM) were meticulously examined in an aqueous medium containing HEPES to enhance our comprehension of its selective and sensitive binding with diverse cations. As illustrated in (Figure 3.14B), **PP-3** displayed no discernible fluorescence peak when excited at 511 nm in an aqueous medium containing HEPES. Additionally, fluorescence spectra of **PP-3** interactions with metal ions were captured within 5 minutes of introducing the metals under uniform conditions. Upon scrutinizing the resulting fluorescence spectra from **PP-3** interactions with various metal ions, minor alterations (*approximately 1 or 10 nm*) were evident for all metals, except in the instances of mercury and copper ions. All of these showed the effect of mercury and copper ions as a turn-off of the ligand in the HEPES-buffered water environment.

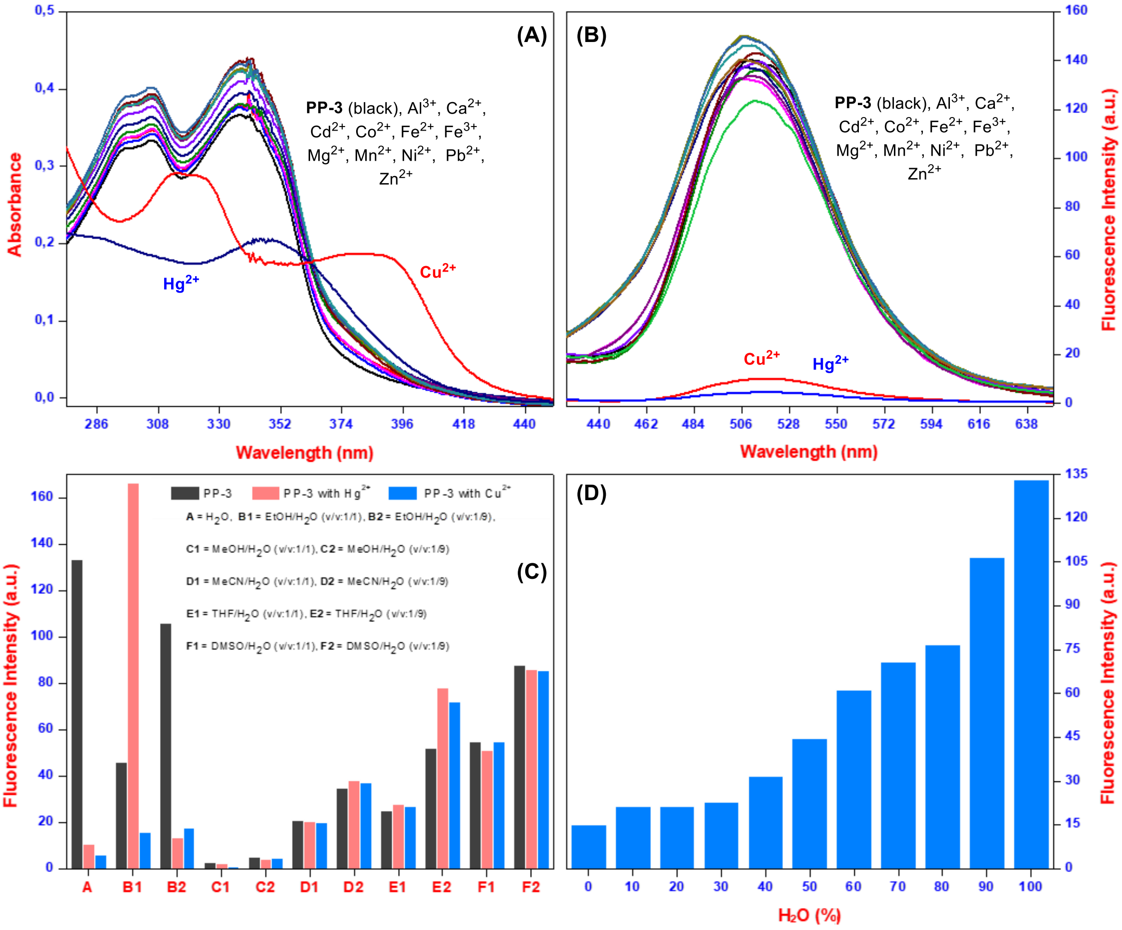

Figure 3.14. The UV-Vis (**A**), the fluorescence (**B**) spectrums of PP-3 in the absence and presence of metal ions in an aqueous medium with HEPES. (**C**) The fluorescent responses of PP-3 with $HgCl_2$/$CuCl_2$ in different solvent systems, and (**D**) according to the increasing H_2O ratio in the EtOH/H_2O solvent system

The limit of detection (LOD), limit of quantification (LOQ), and binding constant (K_a) values are important parameters for analytical studies of organic sensors. Calculation of these values requires precise titration studies between the ligand and ions. For this purpose, following general studies, fluorescence titration studies of **PP-3** were conducted in an aqueous solution under excitation at 360 nm. As can be remembered from previous studies, as a result of the excitation of **PP-3** at 360 nm, the presence of a strong fluorescence peak at approximately 513 nm stands out. Moreover, As the concentrations of Cu^{2+} and Hg^{2+} were increased, a noticeable trend emerged, indicating a gradual reduction in fluorescence intensity. At approximately 4 µM of Hg^{2+} concentration, the fluorescence contrast between **PP-3** and PP-3+Hg^{2+} exhibited a significant 20-fold decrease compared to **PP-3** in water solvent systems. Similarly, at a Cu^{2+} concentration of about 8 µM, the fluorescence contrast between **PP-3** and PP-3+Cu^{2+} displayed a significant 15-fold decrease compared to **PP-3**. Following sensitive fluorescence titration studies, LOD and LOQ values of the binding between ligand **PP-3** and ions were calculated using the relevant formulas given in the experimental section. The LOD and LOQ values for **PP-3** with Cu^{2+} and Hg^{2+}ions were determined as 117 nM (for Hg^{2+}) / 1.56 µM (for Cu^{2+}) and 357 nM (for Hg^{2+}) / 4.72 µM (for Cu^{2+}) as depicted in (Figure 3.15A-B). The obtained values hold great significance as they reside at a critical threshold. This importance emanates from the fact that, although highly sensitive organics can detect at the parts per million (ppm) level, the ability to respond at the micromolar (µM) level is particularly crucial for detecting samples with low concentrations of mercury and/or copper in real water systems.

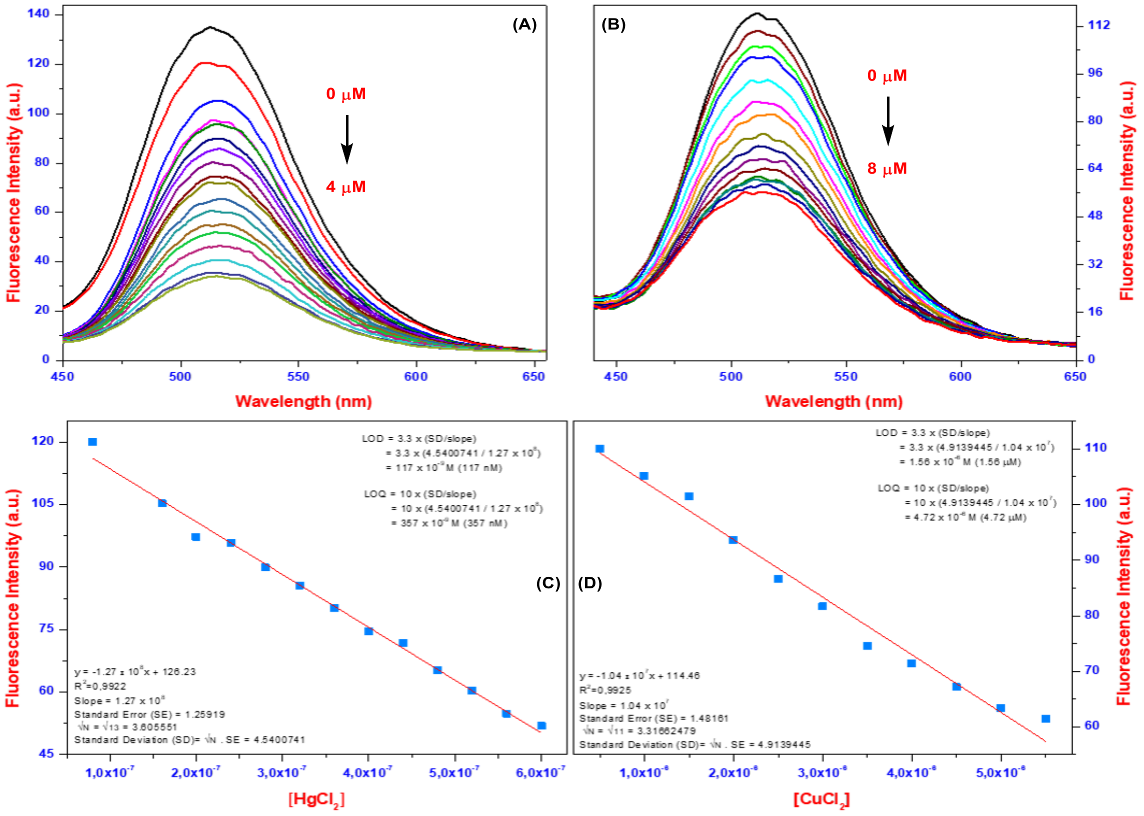

Figure 3.15. Fluorescence titration spectra of PP-3 in the presence of increasing $HgCl_2$ (**A**) and $CuCl_2$ (**B**) in H_2O, and the change fluorescence intensity of PP-3 with the increasing concentration of $HgCl_2$ (**C**) and $CuCl_2$ (**D**) in H_2O

Comprehensive analysis of sensor candidates requires the basic determination of the value of the K_a. This involves the precise stoichiometric determination of the binding interaction between the organic probe **PP-3** and mercury and copper. In this context, first, the binding modes between **PP-3** and Cu^{2+} as well as Hg^{2+} were elucidated by comprehensive functionalization analysis. In an aqueous medium containing HEPES, the fluorescence and absorbance intensity of mixtures containing **PP-3** with Cu^{2+} and Hg^{2+} ions were systematically measured across varying molar ratios. The results obtained from both UV-Vis and fluorescence studies showed that the interaction ratio between the ions and the probe was 2:1 (PP-3:M^{2+}). Following this, the determination of the binding constant (K_a) for **PP-3** with Cu^{2+} and Hg^{2+}ions involved calculating the slope of graphs generated through fluorescence titration and applying the Benesi-Hildebrand equation (2.3). By utilizing concentration-dependent fluorescence changes, the binding constants for **PP-3** with Cu^{2+} and Hg^{2+} in an aqueous medium containing HEPES were computed as 1.94×10^4 $M^{-1/2}$ and 7.98×10^4 $M^{-1/2}$, respectively (Figure 3.16C-D).

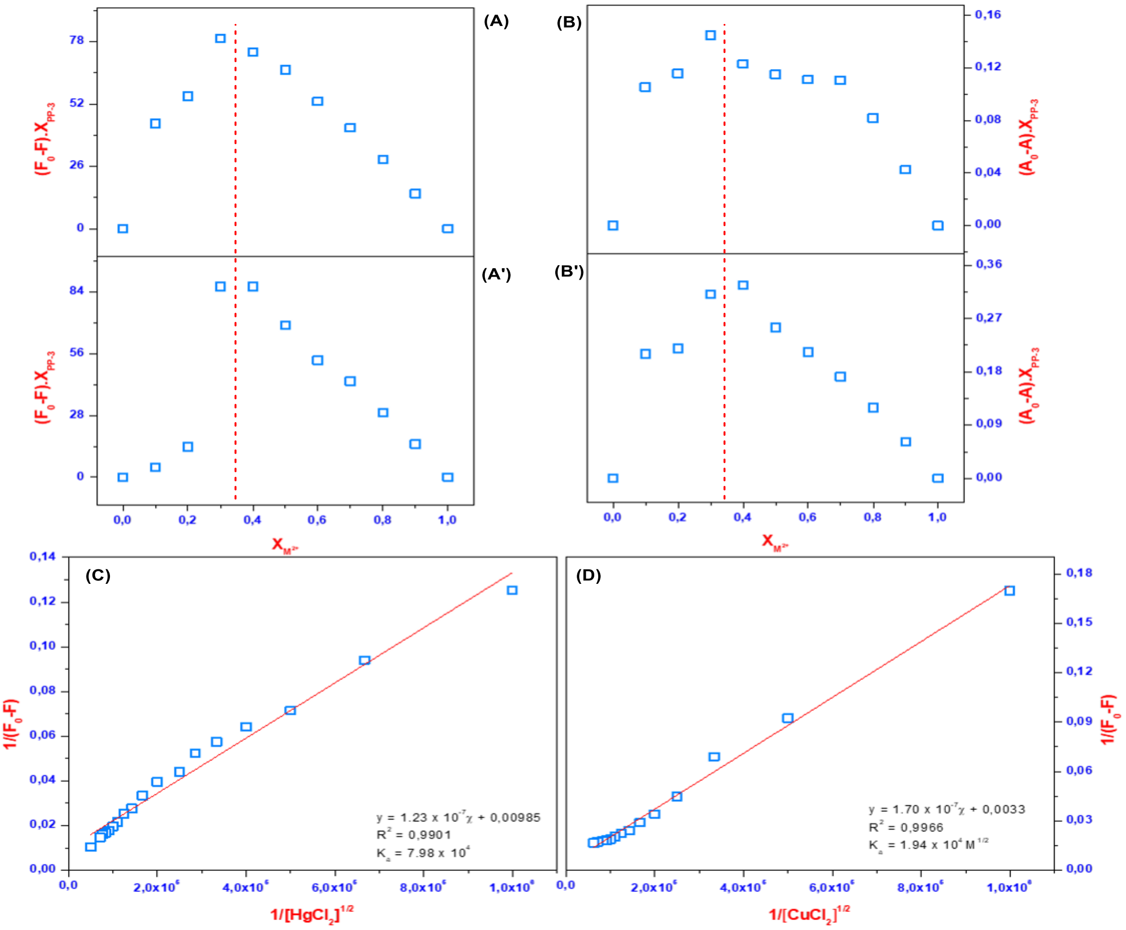

Figure 3.16. Job's plot of PP-3 with $HgCl_2$ (**A, B**)/$CuCl_2$ (**A'**, **B'**), and Benesi-Hildebrand plot based on a 1:2 association stoichiometry between PP-3 (**A**) with the increasing concentration of Hg^{2+}(**C**) and Cu^{2+}(**D**)

Exploring pH variations is imperative for characterizing materials with sensing potential. Comprehensive pH studies were undertaken on **PP-3** (10 μM) in H_2O, spanning a pH range from 1 to 12. Particularly noteworthy were the observations at pH 7, employing a HEPES buffer solution in an aqueous medium, where a pronounced increase in fluorescence intensity was observed exclusively (Figure 3.17A and Ap.19). Our investigations revealed that **PP-3** reached its maximum fluorescence intensity at pH 7 when placed in an aqueous medium with a HEPES buffer solution. Remarkably, at other pH values, **PP-3** exhibited relatively diminished fluorescence values. Conversely, the fluorescence peak at 511 nm, achieved at pH 7 with the use of a HEPES buffer solution in an aqueous medium, experienced a reduction upon the introduction of Cu^{2+} and Hg^{2+} to **PP-3**. Minor alterations were detected across various pH values for the PP-3+Hg^{2+} and PP-3+Cu^{2+} complexes, with no substantial differences observed. Consequently, based on the pH studies, the pH of the aqueous medium was adjusted to 7 using HEPES buffer solution. (Figure 3.17A). In conclusion, the broad pH range within an aqueous environment presents significant and versatile application potential. This versatility proves particularly valuable in diverse fields, such as the detection of copper and mercury in blood, industrial analysis, wastewater assessment, and physiological treatment. The dynamic interaction between mercury or copper ions and the side groups (TSC) of **PP-3** brings about a notable reduction in fluorescence intensity, leading to a distinctive shut-off effect. This observation emphasizes that acidic interactions with the side groups of **PP-3** also result in a substantial decrease in fluorescence intensity. This observation signifies that both acidic and ionic interactions Cu^{2+} and Hg^{2+} with the side groups (TSC) of **PP-3** exert a detrimental influence on aggregation, ultimately resulting in a decline in fluorescence intensity. Conversely, (Figure 3.17A) offers a detailed insight into **PP-3** sensing capability for the aqueous medium using a HEPES buffer solution, illustrating a conspicuous shift characterized by a noteworthy increase in the absorption intensity of **PP-3** from 477 nm to 511 nm (redshift). pH examinations were performed on the PP-3+Hg^{2+} and PP-3+Cu^{2+} system in H_2O, spanning a pH range from 1 to 12. Notably, the fluorescence intensity showed an obvious decrease, indicating that changes in pH levels do not affect the PP-3+Hg^{2+} and PP-3+Cu^{2+} systems. This observation confirms the existence of a strong and stable affinity between **PP-3** and ions at room temperature. The fluorescence intensity of **PP-3**, exposed to Cu^{2+} and Hg^{2+} ions, was tracked over time (Figure 3.17B). Remarkably, the fluorescence intensity of **PP-3** exhibited a rapid and significant decrease of more than 100% within only 1 min of exposure time (Figure 3.17B). This reduction in adsorption intensity highlights the dynamic response of PP-3 to environmental changes. Exploring pH variations is imperative for characterizing materials with sensing potential. Comprehensive pH studies were undertaken on **PP-3** (10 μM) in H_2O, spanning a pH range from 1 to 12. Particularly noteworthy were the observations at pH 7, employing a buffer solution in an aqueous medium, where a pronounced increase in fluorescence intensity was exclusively observed (Figure 3.17B and Ap.19). Cu^{2+} and Hg^{2+} or investigations revealed that **PP-3** reached its maximum fluorescence intensity at pH 7 when placed in an aqueous medium with a HEPES buffer solution. Remarkably, at other pH values, **PP-3** exhibited relatively diminished fluorescence values. Conversely, the fluorescence peak at 511 nm, achieved at pH=7 with the use of a HEPES buffer solution in an aqueous medium, experienced a reduction upon the introduction of Cu^{2+} and Hg^{2+} to PP-3. Minor alterations were detected across various pH values for the PP-3+Hg^{2+} and PP-3+Cu^{2+}complexes, with no substantial differences observed. Consequently, based on the pH studies, the pH of the aqueous medium was adjusted to 7 using HEPES buffer solution (Figure 3.17A).

In conclusion, the broad pH range within an aqueous environment presents significant and versatile application potential, particularly in diverse fields such as the detection of copper and mercury in blood, industrial analysis, wastewater assessment, and physiological treatment. The dynamic interaction between mercury or copper ions and the side groups (TSC) of **PP-3** led to a notable reduction in fluorescence intensity, resulting in a distinctive shut-off effect. This observation emphasizes that acidic interactions with the side groups of **PP-3** also result in a substantial decrease in fluorescence intensity. Both acidic and ionic interactions Cu^{2+} and Hg^{2+} with the side groups (TSC) of **PP-3** exert a detrimental influence on aggregation, ultimately resulting in a decline in fluorescence intensity. Conversely, (Figure 3.17A) offers a detailed insight into **PP-3's** sensing capability for the aqueous medium using a HEPES buffer solution, illustrating a conspicuous shift characterized by a noteworthy increase in the absorption intensity of PP-3 from 485 nm to 511 nm (red-shift). pH examinations were performed on the PP-3+Hg^{2+} and PP-3+Cu^{2+}system in H_2O, spanning the range from 1 to 12. Notably, the fluorescence intensity showed an obvious decrease, indicating that changes in pH levels do not significantly affect the PP-3+Hg^{2+} and PP-3+Cu^{2+} systems. This observation confirms the existence of a strong and stable affinity between **PP-3** and ions at room temperature. The adsorption intensity of **PP-3**, exposed to Cu^{2+} and Hg^{2+} ions, was tracked over time (Figure 3.17B). Remarkably, the adsorption intensity of **PP-3** showed a decrease of more than 100% within only 1 minute of exposure time, as shown in (Figure 3.17B and Ap.20).

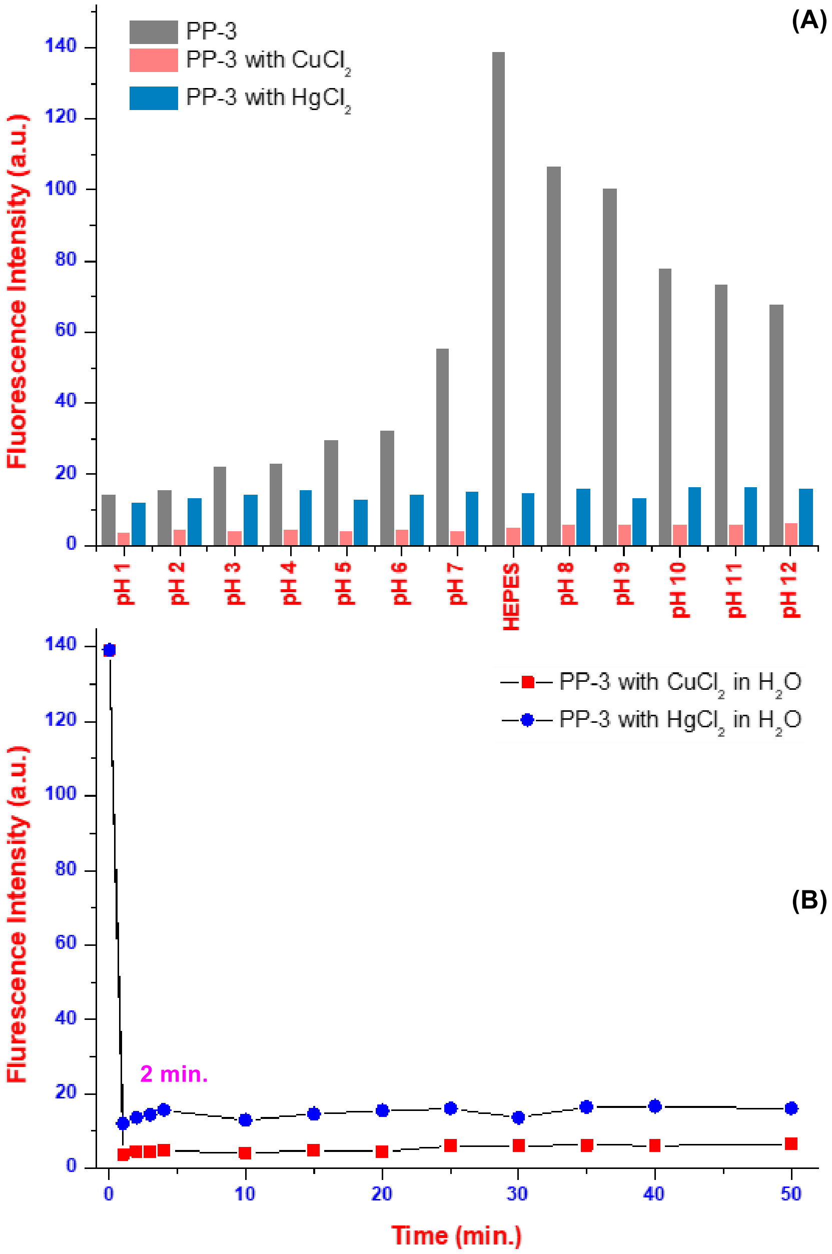

Figure 3.17. The fluorescence values of PP-3 with $CuCl_2$ and $HgCl_2$ at different pH (1–12) values (**A**), and the exposure times of PP-3 with $CuCl_2$ and $HgCl_2$

The potential for **PP-3** to interact with multiple ions raises concerns about unintended probe interactions. Given the likelihood of wastewater samples containing various metal types, it's crucial to identify probe-ion interactions and their resulting spectral changes. Consequently, competitive tests were carried out by examining fluorescence in the presence of Hg^{2+} (10 μM) and other metals (10 μM) in an aqueous environment (Figure 3.18A). The results showed that the amalgamation of the complex PP-3+Hg^{2+} with various metal ions failed to induce a fluorescence increase similar to that observed for **PP-3** in an aqueous medium with a HEPES buffer solution (Figure 3.18A and Ap.21). Therefore, it was inferred that none of the examined metal ions disrupted the interaction between PP-3 and Hg^{2+} ions. Organic probes, as chemosensor candidates, should exhibit switchable or reversible sensing properties, which is a fundamental attribute of organic sensors. In extensive reversal experiments, the sequential addition of Hg^{2+} and $[Bu_4N]I$ to PP-3 triggered a reversible modulation in the emission intensity at 511 nm (Figure 3.18A and Ap.21). Due to the strong binding of iodine ions to mercury, it is reasonable to infer their separation from the PP-3+Hg^{2+} complex, leading to the formation of HgI_2. The liberated **PP-3** can then be used for reversible sensing of Hg^{2+} and I^{-} for approximately four cycles. Hence, **PP-3** can serve as a reversible fluorescence sensor for both mercury and iodine ions, as demonstrated in (Figure 3.18A). Based on the optical responses of **PP-3** to mercury and iodine inputs, the output corresponds to the emission intensity at 485 nm from **PP-3** in an aqueous medium containing HEPES systems. Establishing a logic gate involves designating directing sites 1 and 0 to represent "on" and "off" fluorescence, respectively. In this custom configuration, **PP-3** as a chemical sensor remains in the “on” state in the absence of input Hg^{2+} (In1) and I^{-} (In2). When Hg^{2+} (In1) was introduced into the **PP-3**, a significant decrease in fluorescence intensity occurred at 511 nm, deactivating directing site 0. Conversely, when only I^{-} (In2) ions were added to the **PP-3**, a significant rise in fluorescence intensity occurred at 485 nm, activating directing site 1. The fluorescence intensity of **PP-3** at 511 nm exceeded the 135 nm threshold for inputs (0/0), (0/1), and (1/1), but fell below 140 nm for input (1/0). Utilizing this logic gate system to investigate the **PP-3** fluorescence intensity at 485 nm, with a threshold set at 110 nm, offers a potential means to distinguish between Hg^{2+} and I^{-} (Figure 3.18A-B and Ap.22).

Glutathione (GSH), a crucial cellular antioxidant, guards against damaging free radicals and toxins. Its detection is vital, and organic-copper complexes offer a promising approach due to their strong affinity for GSH. We investigated the interaction between the PP-3+Cu^{2+} complex and GSH in water using fluorescence titration. The complex's fluorescence steadily increased with GSH, reaching saturation at 5 μM. The LOD and LOQ were calculated as 1.80 μM and 5.47 μM, respectively, highlighting the potential of this method for GSH determination (Figure 3.19A-B).

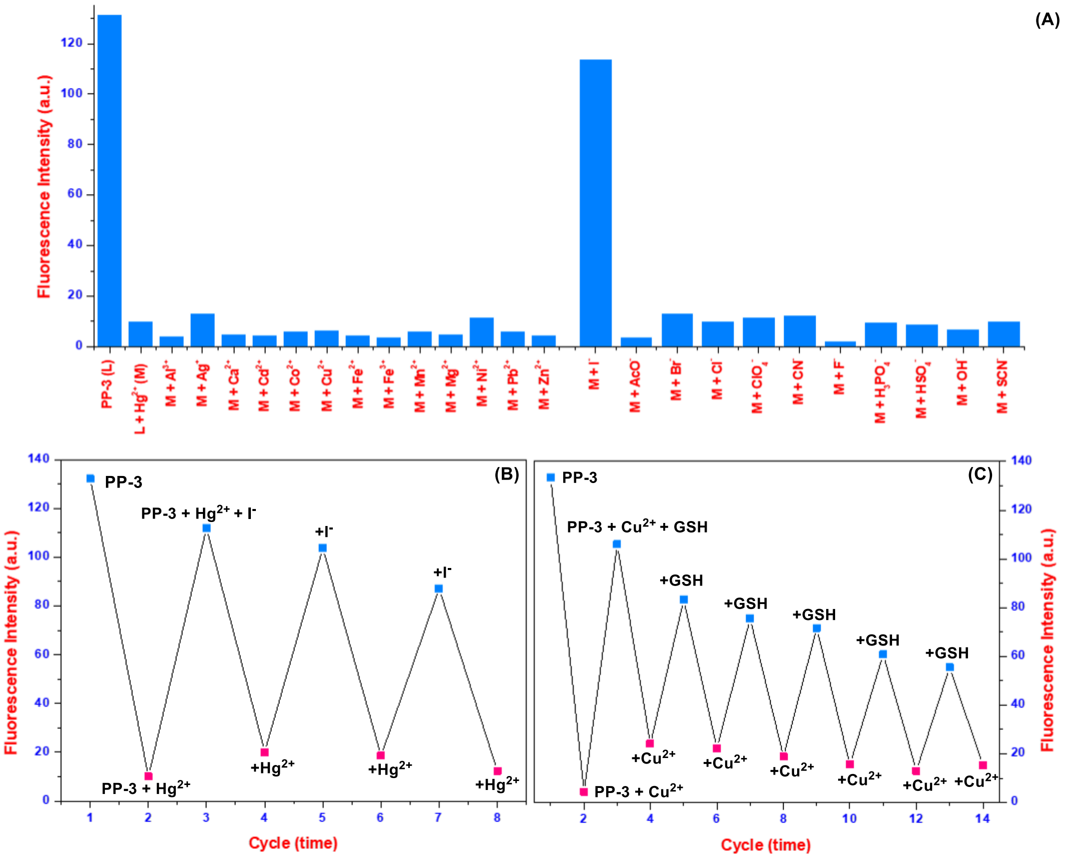

Figure 3.18. The fluorescence selectivity of PP-3 for Hg^{2+} in the presence of other ions **(A)**, and the reversible switching of the fluorescence intensity of PP-3 + H g^{2+} and PP-3 + Cu^{2+} with I^{-} **(B)** and GSH **(C)**

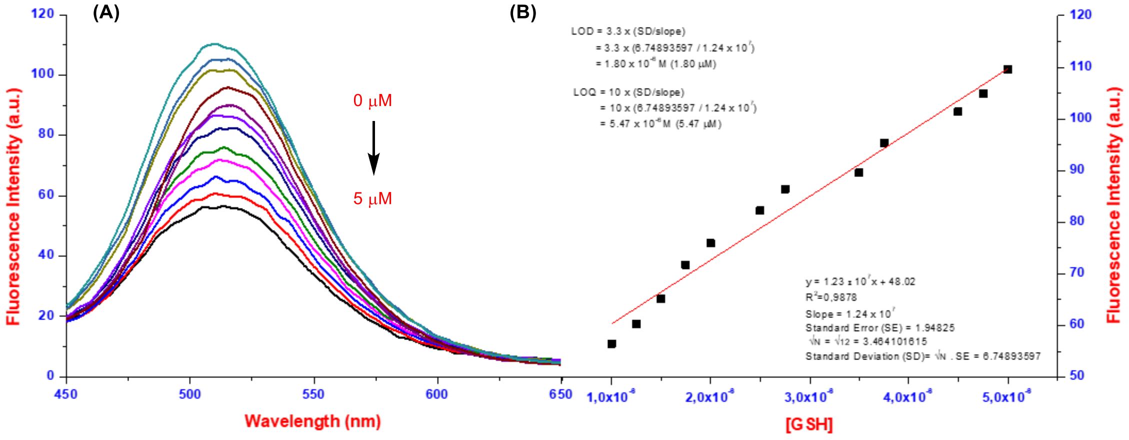

Figure 3.19. Fluorescence titration spectra of PP-3/Cu^{2+} in the presence of increasing GSH in H_2O **(A)**, and (**B**) the change in fluorescence intensity of PP-3/Cu^{2+} with the increasing concentration GSH in H_2O

The fluorescence quantum yield ϕ was calculated using the standard proportional method, the quantum yield of **Rh-101** in ethanol was standardized to (λex = 500nm, ϕ_{ref}= 1) to ascertain the quantum yield of the molecular sensor (**PP-3**) in water. The calculation of fluorescence quantum yields employed the (Figure Ap. 22C). The quantum yield of the molecular sensor was determined at λex = 360 nm, resulting in ($\emptyset_s = 0.114$) and applying the equation (2.4).

3.2.4. Selectivity and Sensitivity Studies of Rh-1

Following the synthesis of **Rh-1** (**Rh-PP-Rh**) as a probe, initially, we studied how different solvents affected the interaction between **Rh-PP-Rh** and various metal ions. This helped us find the best conditions for precise color measurements (absorbance) to identify and measure ions. The studies were started with a common and eco-friendly solvent mixture (EtOH/H_2O). **Rh-PP-Rh** in this mixture had specific absorption patterns, as shown in (Figure 3.20A). Interestingly, adding mercury ions caused a distinct change: the original absorption peak at 405 nm disappeared, and a new peak emerged at 558 nm. After studying how light absorption changed with metal ions, we investigated the fluorescence abilities of **Rh-PP-Rh** to detect them using fluorescence spectroscopy. They tested **Rh-PP-Rh** in various organic solvents (CH_3CN, DMSO, EtOH, MeOH, and THF) and water mixtures to find the best environment. While some solvents (DMSO, THF, DMSO/H_2O, and THF/H_2O) didn't show any interaction, others like methanol, ethanol, and acetonitrile did (Figure Ap. 23A). Importantly, only the EtOH/H_2O mixture showed a specific response to mercury ions, as seen in (Figures 3.20 B and Ap. 23B) Considering this and its lower toxicity compared to other options, the EtOH/H2O mixture was chosen as the optimal solvent system. Following solvent studies, we used fluorescence to see how **Rh-PP-Rh** binds to different metal ions in the chosen EtOH/H_2O mixture (Figure 3. 20C). On its own, **Rh-PP-Rh** didn't emit any light when exposed to specific light (excitation) at 550 nm. Also, adding most metal ions caused very small changes in the light emission pattern. However, when mercury ions were added, a significant shift occurred, resulting in a new peak around 582 nm. This shift suggests that **Rh-PP-Rh** interacts strongly with mercury, causing a change in its structure (from closed-form Rh to open-form Rh). Furthermore, we also investigated how much water affected the interaction between **Rh-PP-Rh** and metal ions (Figure 3.20D and Ap.23C). In pure alcohol (EtOH), **Rh-PP-Rh** interacted with several metal ions, including mercury. But as more water was added, the interaction with other ions disappeared. Interestingly, **Rh-PP-Rh** still responded to mercury even in solutions with up to 50% water. This suggests **Rh-PP-Rh** could be a good sensor for mercury ions in water-alcohol mixtures. The decrease in performance at higher water content is likely because **Rh-PP-Rh** becomes less soluble.

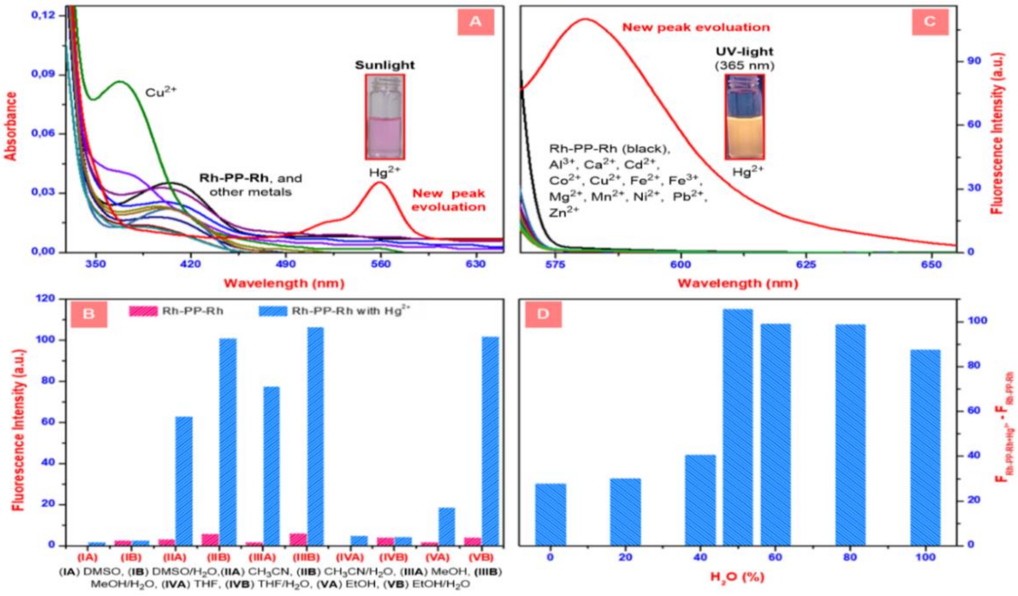

Figure 3.20**.** The UV-Vis (**A**), the fluorescence (**C**) spectrums of Rh-PP-Rh in the absence and presence of metal ions in EtOH/H_2O (v/v: 1/1, with HEPES), the fluorescent responses of Rh-1 with Hg^{2+} in different solvent systems (**B**), and according to the increasing H_2O ratio in the EtOH/H_2O solvent system (**D**)

As mentioned before, a significant portion of sensor studies consists of quantitative as well as qualitative studies. In this context, at this stage, we tested how sensitive **Rh-PP-Rh** was at detecting mercury ions using fluorescence in an EtOH/H_2O (v/v:1/1) (Figure 3.21A). We already studied how **Rh-PP-Rh** interacted with light and other ions using different techniques (UV-Vis and general fluorescence). When they gradually added more mercury chloride ($HgCl_2$) to **Rh-PP-Rh**, the emission intensity steadily increased. The difference in light emission between **Rh-PP-Rh** alone and **Rh-PP-Rh** with high levels of mercury (around 5 μM $HgCl_2$) was more than 30 times greater. This shows that **Rh-PP-Rh** is very sensitive to mercury. Following, based on these results, we calculated how much mercury **Rh-PP-Rh** could detect with high confidence (limit of detection, LOD) and how much it could accurately measure (limit of quantification, LOQ). These values were calculated as 0.334 μM (334 nM) and 1.01 μM, respectively, in the alcohol-water mixture.

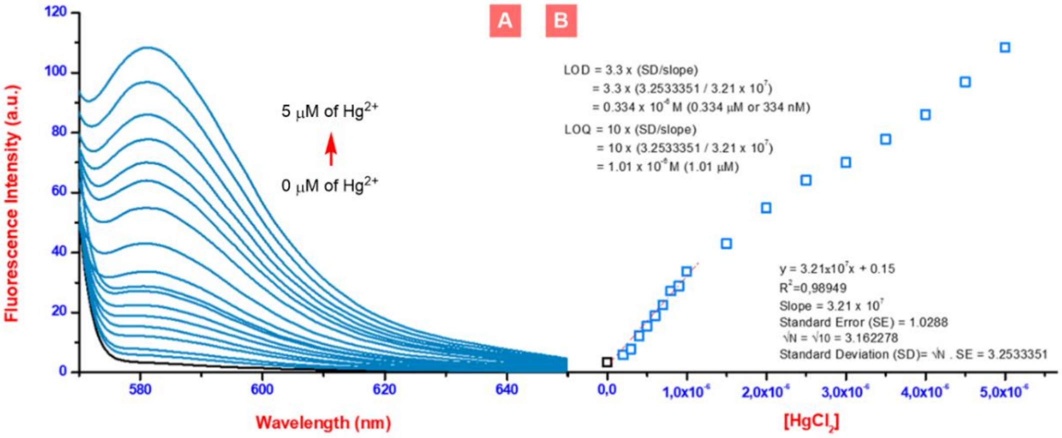

Figure 3.21. (**A**) The fluorescence titration spectra of Rh-PP-Rh in the presence of Hg^{2+}, and (**B**) the change fluorescence intensity of the Rh-PP-Rh with the increasing concentration of Hg^{2+}

To understand how well **Rh-PP-Rh** binds to mercury, we needed to find two key things: first, how many **Rh-PP-Rh** molecules bind to one mercury ion, and second, the determination of the binding constant (K_a). First, we used a technique called Job's plot analysis to figure out the binding ratio. This analysis showed that one **Rh-PP-Rh** molecule binds to two mercury ions (Figure 3.20A). Next, we used the results from the fluorescence experiments (mentioned earlier) to calculate the Ka value using the Benesi-Hildebrand plot. A high K_a value indicates a strong bond. In this case, the K_a value was 9.33×10^{11} M^{-2}, which means **Rh-PP-Rh** binds very strongly to mercury ions (Figure

3.22B). Another important factor for sensors is how they react to different pH levels. For this purpose, we also tested **Rh-PP-Rh** in a wide range of pH values (3 to 12) in the EtOH/H_2O (v/v/:1/1) (Figure 3.22C). As a result of our research, we found that **Rh-PP-Rh** worked best between a pH of 2 and 7, and its effectiveness decreased at higher pH levels (Figure 3.22C, red). This is likely because part of the **Rh-PP-Rh** molecule closes up under more basic conditions (high pH), which affects its ability to bind mercury. Furthermore, at very acidic levels (pH 2 and pH 3), the molecule **Rh-PP-Rh** changes its structure on its own, regardless of the presence of mercury. This makes it unsuitable as a sensor for mercury at these pH levels, although it could still be useful as a general indicator. However, in the slightly acidic to neutral range (pH 4-7), **Rh-PP-Rh** still interacts with mercury ions, even though the response is slightly weaker. Lastly, we also investigated how long it took for **Rh-PP-Rh** to react fully with mercury ions. For this, we monitored the light emission (fluorescence) over time as **Rh-PP-Rh** was exposed to mercury (Figure 3.22D). The results showed a steady increase in light emission at a specific wavelength (581 nm) for about 12 minutes. This suggests that the interaction between **Rh-PP-Rh** and mercury starts around 5 minutes and takes roughly 12 minutes to reach its maximum level.

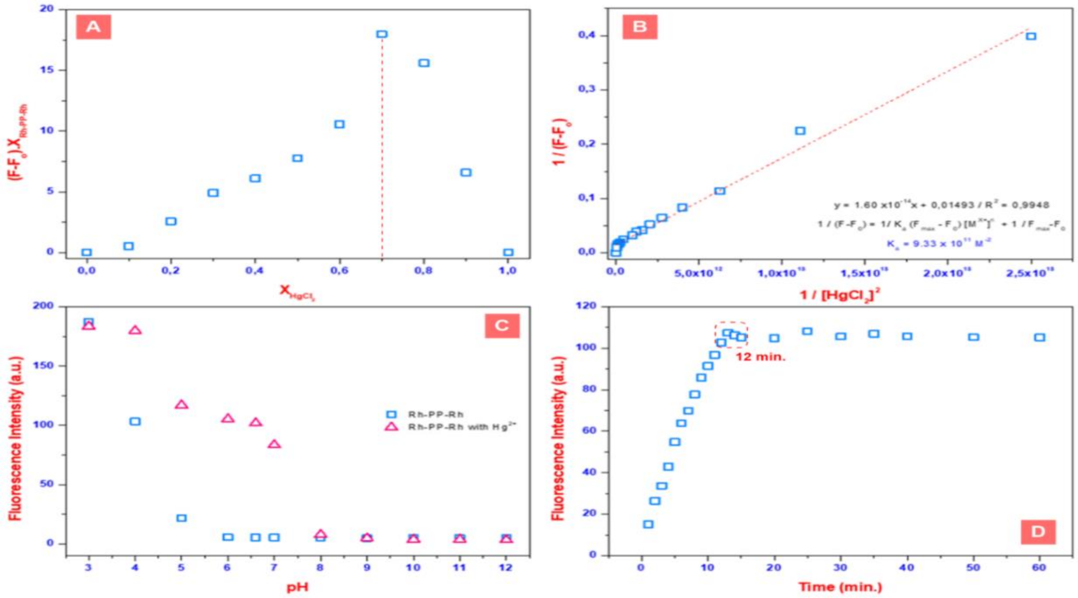

Figure 3.22. The Job's plot of the Rh-PP-Rh with $HgCl_2$(**A**), the Benesi–Hildebrand plot based on a 1:2 association stoichiometry between Rh-PP-Rh and Hg^{2+}(**B**), the fluorescence values of Rh-PP-Rh with [$HgCl_2$] at different pH (3–12) values(**C**), and the exposure times of the Rh-PP-Rh with $HgCl_2$(**D**)

It's important to consider how **Rh-PP-Rh** might react to other metals besides mercury, especially since real-world samples like wastewater often contain multiple metal ions. To test this, we conducted experiments where they exposed **Rh-PP-Rh** to both mercury and other metals simultaneously (Figure 3. 23A) and found that even in the presence of these other metals, **Rh-PP-Rh** still responded to mercury by increasing its light emission (fluorescence) just like it did with mercury alone. This suggests that none of the tested metals interfered with the ability of **Rh-PP-Rh** to detect mercury ions. Moreover, an ideal sensor should be able to turn the detection process on and off. For this purpose, we also tested Rh-PP-Rh+Hg^{2+} with anions and determined that the fluorescence intensity of Rh-PP-Rh+Hg^{2+} decreased only in the presence of fluoride (F^-) or iodide (I^-) ions. Following this result, we tested if **Rh-PP-Rh** could do this with mercury by adding and removing F^- or I^- ions, and found that adding mercury to **Rh-PP-Rh** caused the light emission to turn on (582 nm). Interestingly, adding fluoride or iodide ions could then turn the light emission off, and this process could be repeated a few times (Figure 3.23C and 3.23D). This suggests **Rh-PP-Rh** can be reused for detecting both fluoride and/or iodide ions besides mercury ions. In addition, we used this on/off behavior to create a simple logic function based on the presence or absence of mercury and fluoride ions. For this purpose, we used the on/off behavior of **Rh-PP-Rh** to create a simple logic gate. Imagine a light on represents a "1" and a light off represents a "0". In this system, **Rh-PP-Rh** starts with the light off (logic 0) when there's no mercury (In1) or fluoride (In2) present. Adding mercury turns the light on (logic 1) because of the increased light emission. Contrary, adding fluoride turns the light off (logic 0) because of the non-increased light emission. However, if fluoride and mercury are added together, the light emission goes down, turning the light back off (logic 0) (Figure 3.23D). This shows that **Rh-PP-Rh** can act like a basic logic gate based on the presence or absence of mercury and fluoride ions.

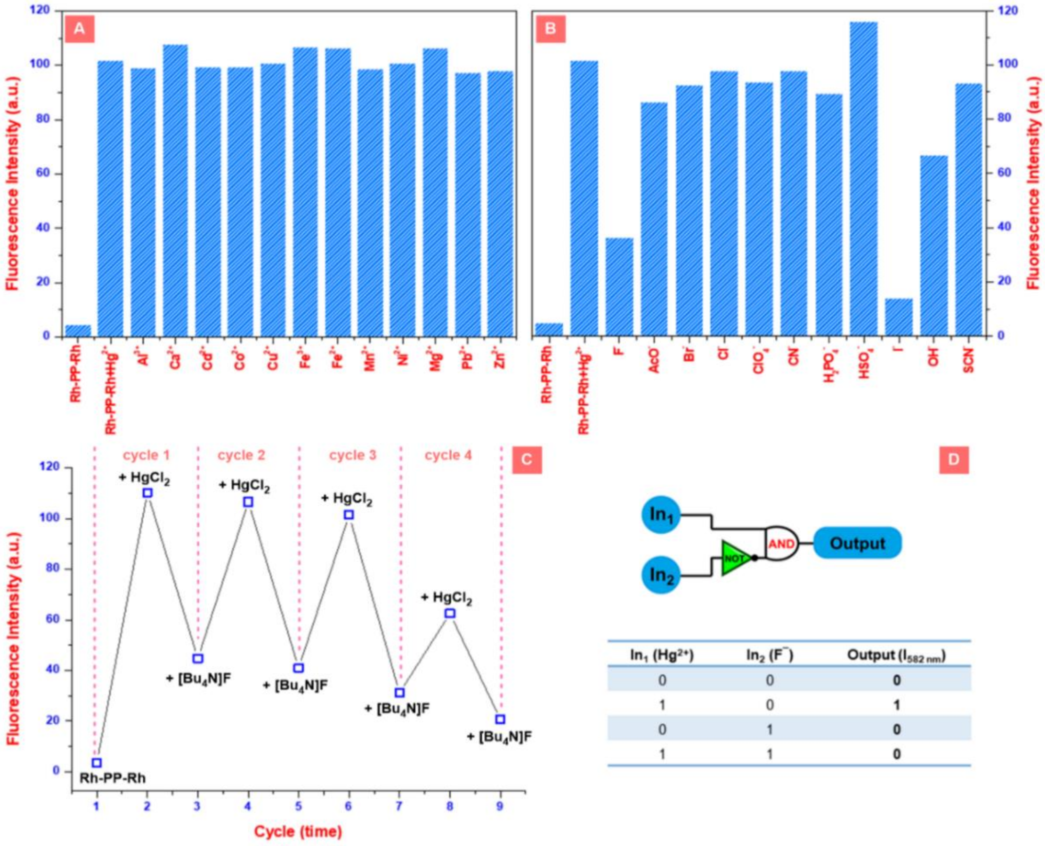

In_1 (Hg^{2+})	In_2 (F^-)	Output ($I_{582\ nm}$)
0	0	**0**
1	0	**1**
0	1	**0**
1	1	**0**

Figure 3.23. The selectivity of Rh-PP-Rh for mercury in the presence of other metal (**A**) / anion (**B**) ions, the reversible switching of the fluorescence intensity (**C**), and the “IMPLICATION” logic gate (**D**)

The observed spectral changes are a result of the formation of 1:2 complexes between **Rh-PP-Rh** and Hg^{2+} ions. To determine the precise binding structure between **Rh-PP-Rh** and Hg^{2+}, we initially tried using ^{1}H-NMR (DMSO-d6) but weren't able to see the expected changes that would indicate a structural change in **Rh-PP-Rh**. This matched our earlier observations (Figure 3.24A). Since the initial test didn't work, we mixed **Rh-PP-Rh** and mercury chloride in EtOH/H_2O (v/v:1/1) and saw a clear color change after about 15 minutes. Following, we evaporated the solvent, and then, analyzed the resulting mixture using ^{1}H-NMR (DMSO-d6) and found results that supported their proposed mechanism for binding (Figure Ap.9). This mechanism involves a ring-opening in **Rh-PP-Rh** upon binding to mercury. The ring-opening is confirmed by a shift in specific signals (enamine proton and OH peak) in the ^{1}H-NMR spectrum. Other signals remained mostly unchanged. Finally, we also used mass spectrometry to further confirm how **Rh-PP-Rh** interacts with mercury ions (Figure Ap.9 and Ap.10).

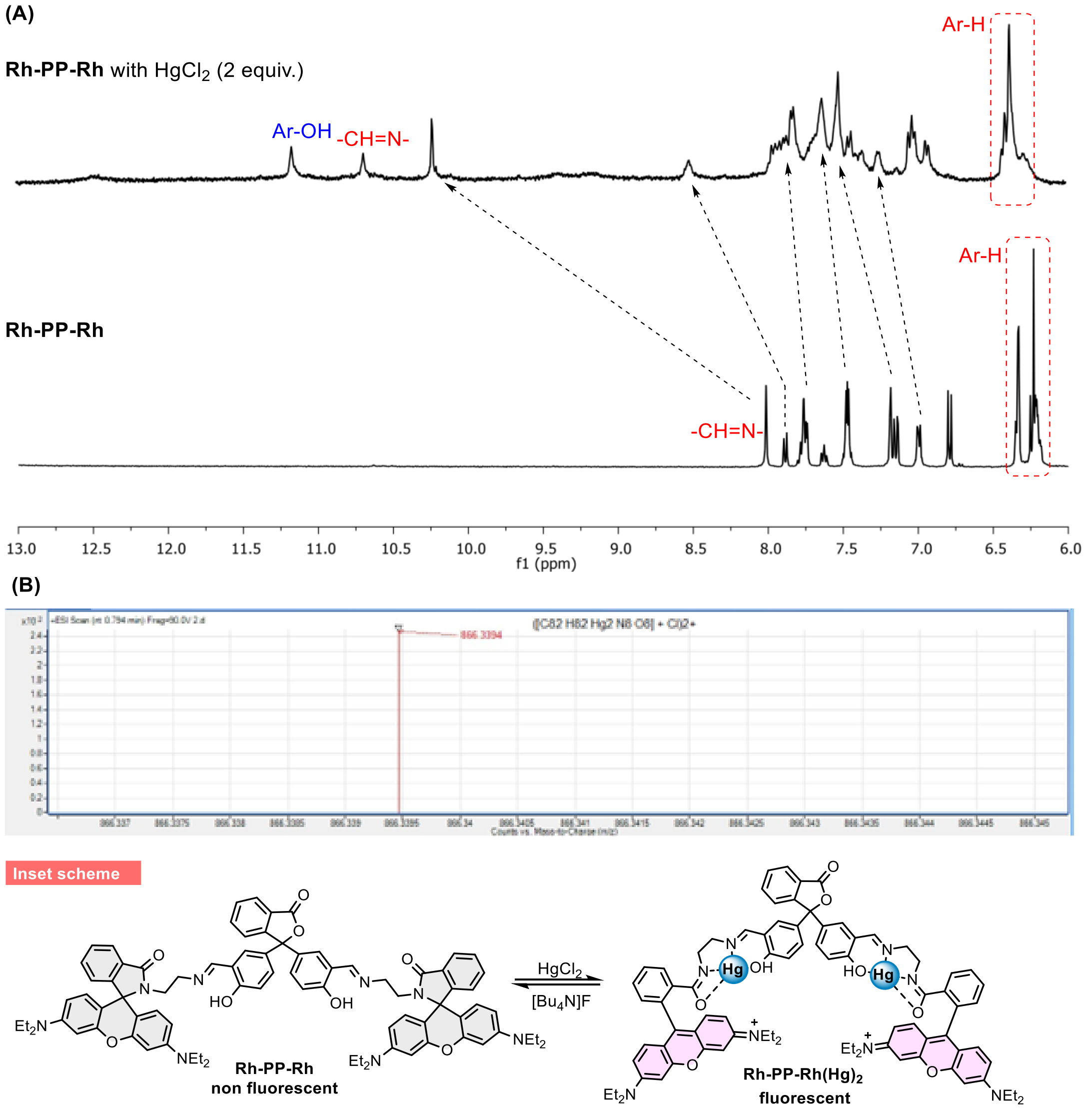

Figure 3.24. ^{1}H-NMR titration of Rh-1 with $HgCl_2$ (DMSO-d6) **(A)**, The HRMS (ESI-TOF) spectrums of Rh-PP-Rh $(Hg)_2$(**B**), and (**Inset scheme**) the principle of a “turn-on/off” sensing for Hg^{2+} and F^{-} detection

Following ^{1}H-NMR and mass studies, we used computer simulations (DFT and TD-DFT) to analyze the energy levels of **Rh-PP-Rh** and its complexes with mercury. These energy levels influence how light interacts with the molecule. We found that in the unbounded **Rh-PP-Rh**, the energy levels were spread across different parts (rhodamine and phenolphthalein). However, when Rh-PP-Rh bonded with Hg^{2+}, the energy levels shifted significantly (Figure 3.25). In the complex, one level (HOMO) stayed focused on the rhodamine part, while another (LUMO) moved closer to the mercury and imine center. This shift explains the observed color change (red-shift) when **Rh-PP-Rh** interacts with Hg^{2+}.

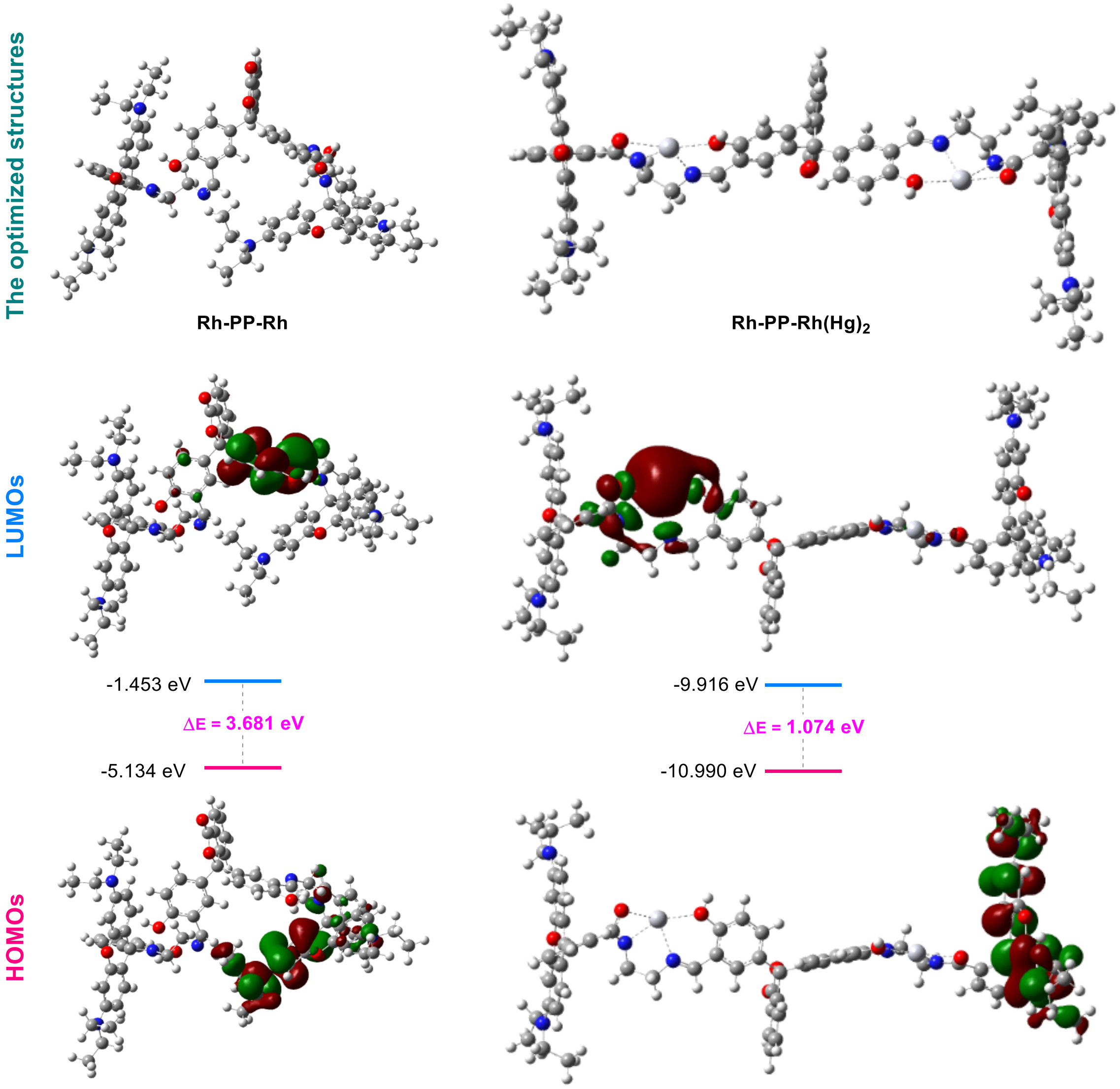

Figure 3.25**.** Ground-state optimized structures and HOMO/LUMO energy gap of Rh-1 and Rh-PP-1$(Hg)_2$

Within the scope of the thesis, **Rh-PP-Rh** detection features were examined in all their dimensions, and finally, naked-eye and filter paper studies were carried out under this heading. For this purpose, initially, we investigated if **Rh-PP-Rh** could be used as a simple and effective tool to detect mercury ions. Initially, we tested its color-changing properties in various solvents (pure alcohol, water, and alcohol-water mixture). In pure alcohol, **Rh-PP-Rh** changed color with several metal ions, including mercury (Figure Ap.27). However, the good news is that in both pure water and water mixed with alcohol, a clear color change only occurred with mercury ions (Figures 3.26A and 3.26B). This suggests **Rh-PP-Rh** can be used as a visual sensor (naked-eye) to detect mercury in both pure water and water-based solutions. Following this, we also created easy-to-use test strips for mercury detection. These strips were made by soaking filter paper in a special **Rh-PP-Rh** solution for a short time. After drying, the strips were exposed to water containing mercury ions. When placed in sunlight or under a UV lamp, the strips with **Rh-PP-Rh** changed color quickly and noticeably, especially when they were dipped in water with both mercury and other metal ions (Figure 3.26C). This simple and affordable method allows for the visual detection of mercury ions. Overall, it can be said that using **Rh-PP-Rh** to develop sensors for mercury detection in water shows great promise for fast and easy testing.

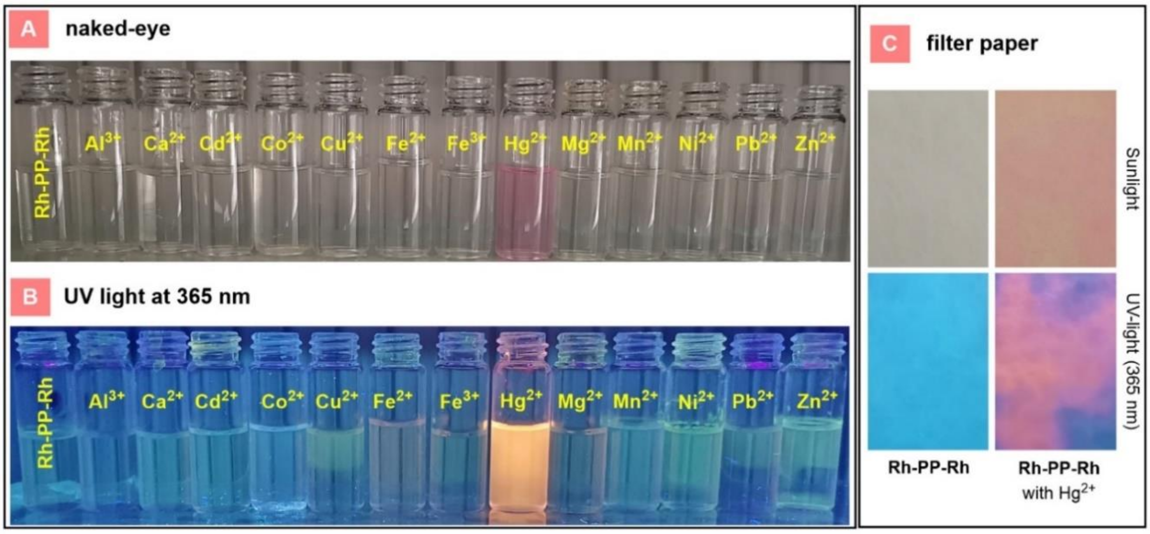

Figure 3.26. The naked-eye (**A**) and UV light at 365 nm (**B**) color changes of Rh-PP-Rh in the presence of metal ions in EtOH/H_2O (v/v: 1/1, with HEPES), and (**C**) the photographs depicting the colorimetric response of Rh-PP-Rh systems

3.2.5. Selectivity and Sensitivity Studies of Rh-2

Following the synthesis of **Rh-2** as a probe, initially, we investigated how different solvents influenced its interaction with various ions. This helped us optimize conditions for using **Rh-2** unique light absorption patterns (Figure 3.27A) to identify and quantify specific ions. **Rh-2** was tested in a range of organic solvents (acetonitrile, dimethyl sulfoxide, ethanol, methanol, and tetrahydrofuran) and water mixtures. We found that **Rh-2** interacted with Hg^{2+}, Al^{3+}, Fe^{2+}, and Fe^{3+} ions in water, EtOH, ETOH/H_2O, MeOH, MeOH/ H_2O, THF, and THF/ H_2O. Interestingly, **Rh-2** showed no interaction in pure DMSO but became selective for Al^{3+} ions in DMSO/ H_2O (v/v:1/1) mixture. Further studies focused on optimizing the DMSO/water ratio for sensor applications. While no interaction was observed in ratios ranging from 10/0 to 8/2 (DMSO/ H_2O, v/v), a specific response towards Al^{3+} ions emerged in ratios from 7/3 to 4/6 (DMSO/ H_2O, v/v). Notably, it was determined that the probe interacted with both Al^{3+} and Hg^{2+} ions in 3/7 to 0.1/9.9 (DMSO/ H_2O, v/v) (Figure 3.27 B). Encouraged by these findings, we explored the impact of pH. In DMSO/H_2O (v/v:1/9, pH 8-12), **Rh-2** did not interact with any ions. However, significant activity was observed for both mercury and aluminum ions at a pH range of 3-7. Most intriguingly, **Rh-2** displayed high selectivity for mercury ions and weak interaction with aluminum ions in DMSO/HEPES (1:9), while only interacting with aluminum ions in DMSO/Tris (1:9) (Figure 3.27 C). Thus, based on kinetic studies, optimal conditions were identified for both qualitative and quantitative analysis. DMSO/Tris (1:9 v/v) was chosen for mercury ion detection, while DMSO/HEPES (1:9 v/v) was specific for aluminum ions. Additionally, lastly, in this part, time-dependent studies were also conducted. In these optimized environments, mercury ions reached their maximum response after 5 minutes, whereas aluminum ions required about 20 minutes (Figure 1D).

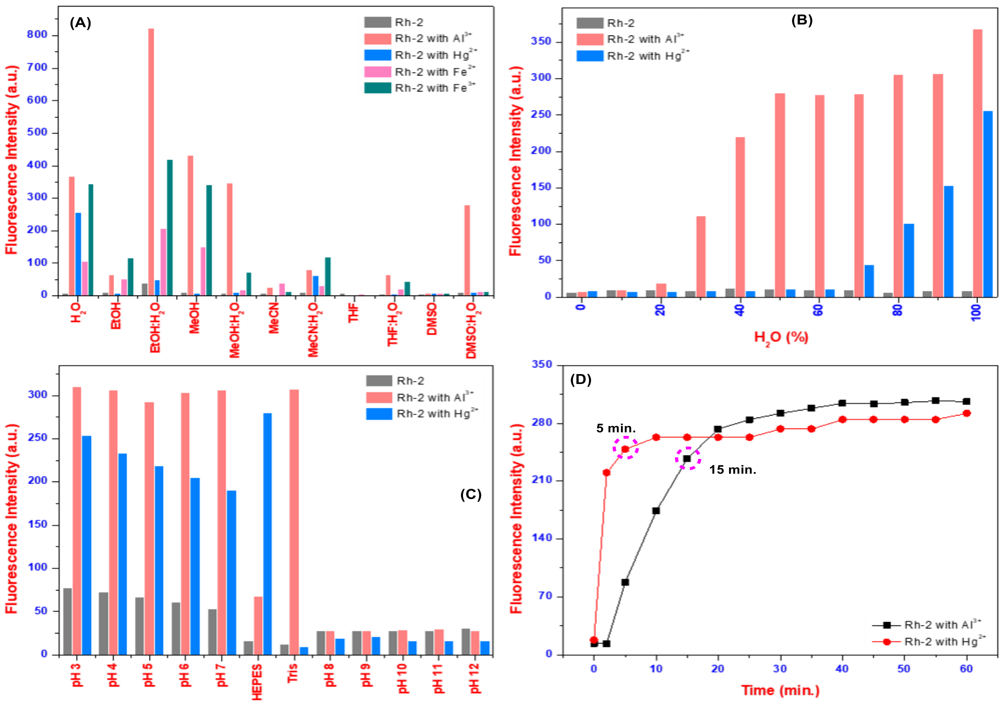

Figure 3.27**.** The fluorescent responses of Rh-2 with ions in different solvent systems (**A**), according to the increasing H_2O ratio in the DMSO/H_2O solvent system (**B**), at different pH (3–12) values (**C**), and the exposure times of the Rh-2 with $HgCl_2$ and $AlCl_3$ (**D**)

After optimizing conditions, we used UV-vis and fluorescence spectroscopy to explore how ions interact with **Rh-2** in DMSO/HEPES (v/v: 1/9) and DMSO/Tris (v/v:1/9). In rhodamine-based probes, a key change in UV-vis spectra is the appearance of a peak due to the opening of the rhodamine ring. When **Rh-2** (closed form) interacts with specific metals under these conditions, it transforms into the open form, generating a new UV-vis peak between 500-600 nm. We monitored UV-Vis spectra after 10 minutes after adding various ions (30μM) to **Rh-2** solutions (10 μM) in both solvent mixtures. In DMSO/Tris (v/v:1/9), the rhodamine ring only opened in the presence of aluminum ions, creating a new peak at 573 nm (Figure 3. 28A). Conversely, in DMSO/HEPES (v/v: 1/9), a strong peak at 560 nm and a weaker peak at 558 nm indicated ring opening upon interaction with mercury and aluminum ions, respectively (Figure 3.28B). Interestingly, the solution color also changed from light yellow to violet upon exposure to aluminum ions in DMSO/Tris (v/v: 1/9) and both mercury and aluminum ions in DMSO/HEPES (v/v: 1/9). This demonstrates the probe's potential for colorimetric detection alongside UV-Vis spectroscopy. Following colorimetric and UV-Vis studies, we further investigated the interaction of **Rh-2** with ions using fluorescence spectroscopy under the optimized conditions determined earlier. Similar to the UV-vis results, fluorescence studies in EtOH/Tris (excited at 550 nm) revealed a new peak at 585 nm in the interaction of **Rh-2** with only aluminum ions (Figure 3.28A'). This "turn-on" response confirmed the probe's selectivity for aluminum in this environment. In EtOH/HEPES, fluorescence peaks emerged at around 583 nm for both mercury and aluminum ions, again indicating the interaction of mercury and aluminum with **Rh-2** (Figure 3.28B'). These results align perfectly with the colorimetric observations, demonstrating that aluminum and mercury detection with **Rh-2** provides clear and consistent signals across multiple spectroscopic techniques.

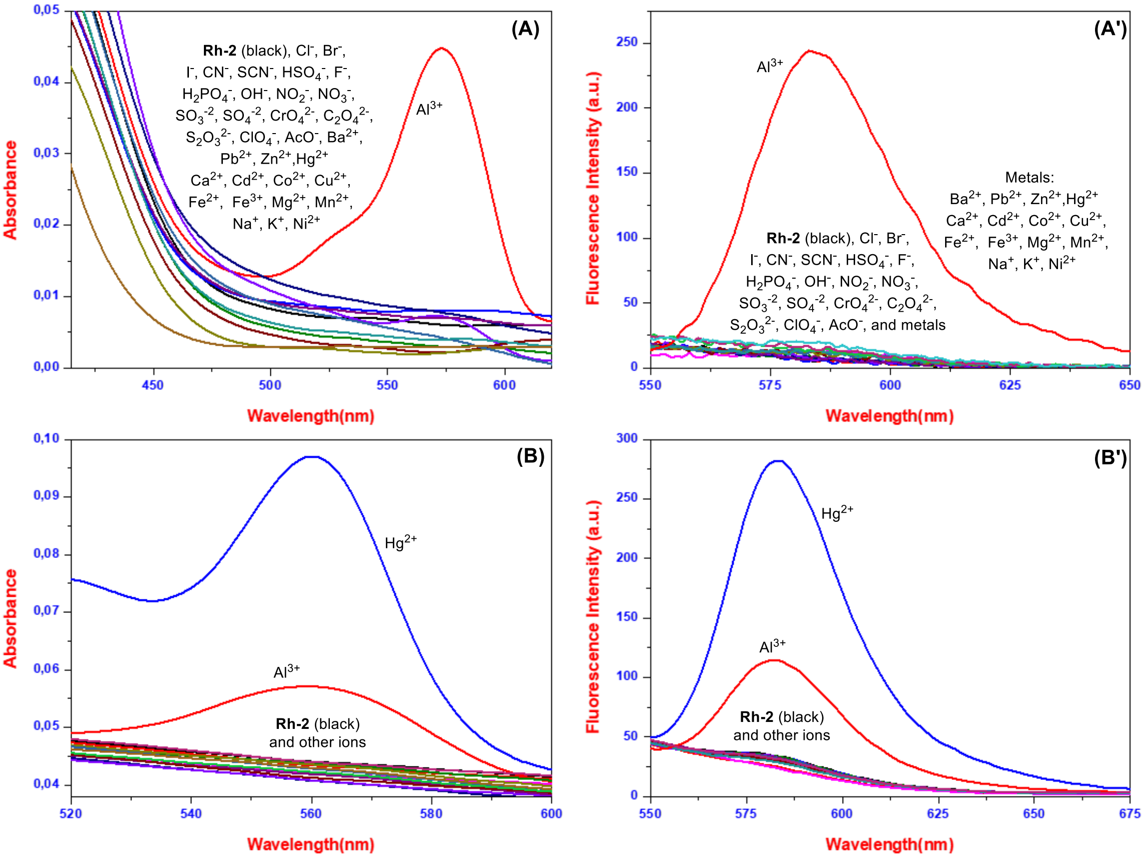

Figure 3.28. The UV-Vis (**A** and **B**), the fluorescence (**A'** and **B'**) spectrums of Rh-2 in the absence and presence of metal ions in DMSO/Tris (v/v: 1/9, **A** and **A'**), and DMSO/HEPES (v/v: 1/9, **B** and **B'**)

Building on our prior studies of **Rh-2**'s light interactions and ion binding, we investigated its sensitivity towards aluminum and mercury ions using fluorescence. We employed DMSO/Tris (v/v:1/9) and DMSO/HEPES (v/v:1/9) solvent mixtures. Titration with increasing concentrations of aluminum and mercury ions resulted in a gradual rise in fluorescence intensity. Notably, the emission intensity with high levels of these ions was over twenty times greater for aluminum and over eight times greater for mercury compared to **Rh-2** alone (Figures 3.29A and 3.29B). This demonstrates **Rh-2** high sensitivity toward these specific ions. Next, leveraging these findings, we determined the LOD and LOQ for mercury and aluminum detection by **Rh-2** in the selected conditions. These values were established as 366 nM (for Hg^{2+}) / 554 nM (for Al^{3+}) and 1.11 μM (for Hg^{2+}) / 1.68 μM (for Al^{3+}) respectively (Figures 3.29C and 3.29D). These results indicate that the simply synthesized rhodamine derivative **Rh-2** functions as an effective quantitative probe for mercury and aluminum ion detection, with performance dependent on solvent conditions.

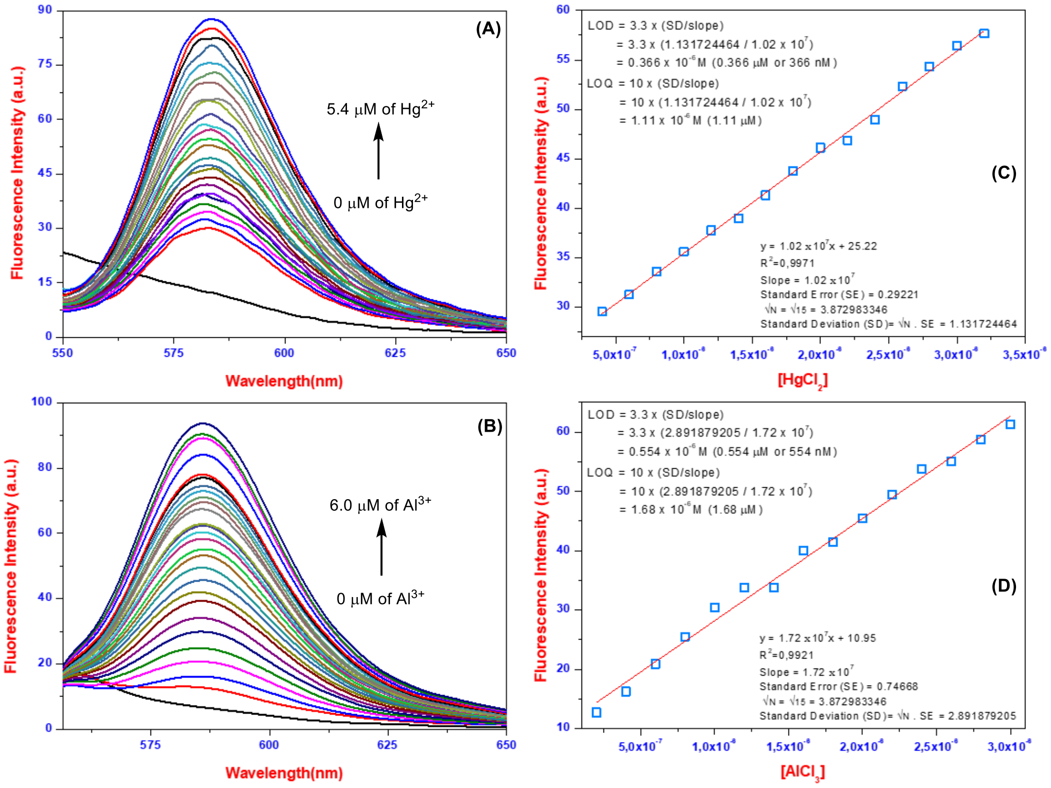

Figure 3.29. The fluorescence titration spectra of Rh-2 in the presence of Hg^{2+} (**A**) / Al^{3+} (**B**), and the change fluorescence intensity of the Rh-2 with the increasing concentration of Hg^{2+} (**C**) / Al^{3+} (**D**)

Other important steps of quantitative analysis studies are the determination of binding stoichiometry and, in this case, the calculation of binding constants. In this context, to quantitatively analyze the interaction of **Rh-2** with aluminum and mercury, two key parameters needed evaluation: binding stoichiometry (the number of ions bound per **Rh-2** molecule) and binding constants. We employed Job's plot analysis (Figures 3.30A and 3.30B) to determine the binding ratio, revealing a 1:1 stoichiometry for both aluminum and mercury ions. Subsequently, the Benesi-Hildebrand plot, along with the aforementioned fluorescence data, allowed us to calculate the binding constant for each ion. A high K_a value signifies a strong binding affinity. The obtained K_a values, 6.37 x 10^4 M^{-1} for Hg^{2+} and 1.53 x 10^5 M^{-1} for Al^{3+}, demonstrate strong binding of **Rh-2** to both metal ions (Figures 3.30C and 3.30D).

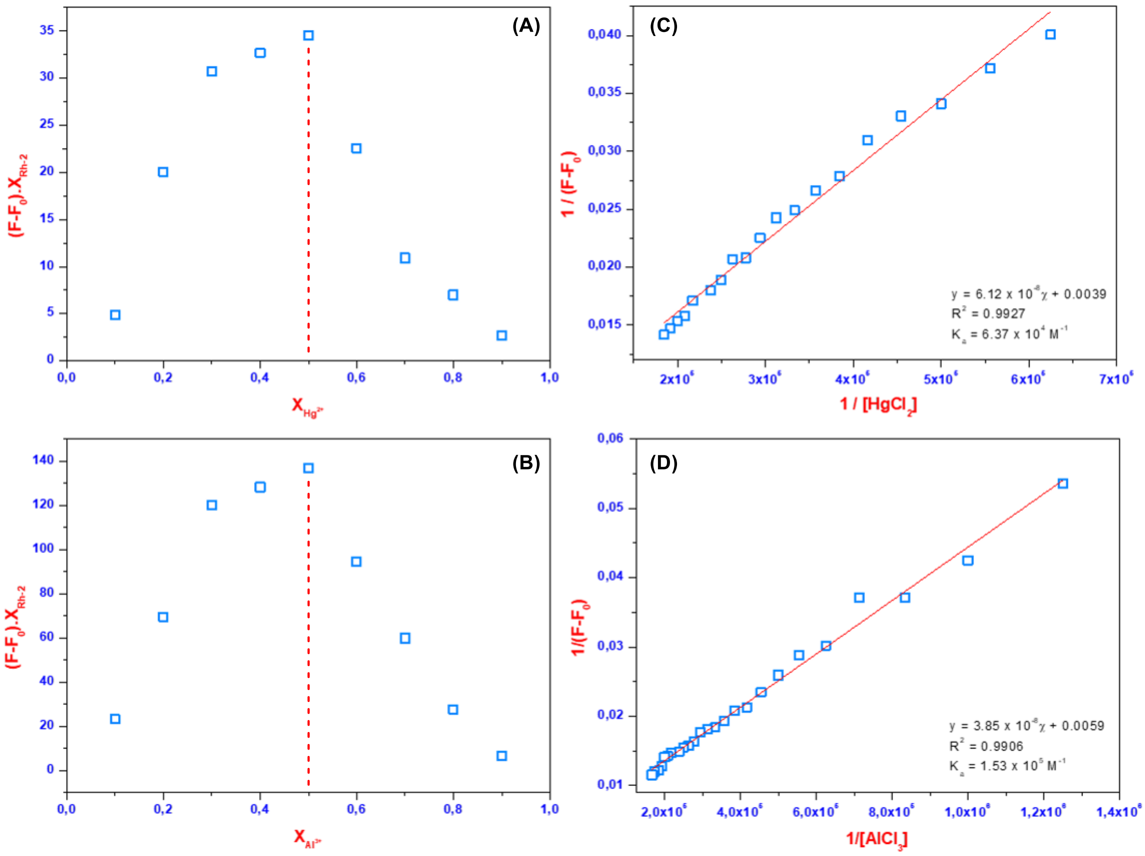

Figure 3.30**.** The Job’s plot of the Rh-2 with $HgCl_2$ (**A**) / $AlCl_3$ (**B**), and the Benesi–Hildebrand plot based on a 1:1 association stoichiometry of Rh-2 with $HgCl_2$ (**C**) / $AlCl_3$ (**D**)

Real-world samples, such as wastewater, often contain a mixture of metal ions. To assess the selectivity of **Rh-2**, we exposed it to aluminum/mercury alongside other metals in the previously defined solvent systems. Gratifyingly, **Rh-2** maintained its response to aluminum/mercury even in these competitive environments, indicating minimal interference from the tested metals. An ideal sensor should also offer reversible detection. To explore this, we investigated the effect of anions on **Rh-2** complexes with Al^{3+} and Hg^{2+}. We observed a decrease in fluorescence intensity upon the addition of cyanide ions for Al^{3+} and iodide ions for Hg^{2+} (Figures 3.31A and 3.31B). This quenching effect offered a potential on/off switch for detection. We tested this concept by adding and removing CN^- and I^- ions (Figure 3.31C). Introducing aluminum/mercury ions turned on the fluorescence emission (583 nm), while the subsequent addition of cyanide or iodide ions quenched it, respectively. Remarkably, this cycle could be repeated several times, suggesting the potential of **Rh-2** for reusability in detecting not only aluminum/mercury but also cyanide and iodide ions. Leveraging the observed on/off switching behavior, we explored the possibility of constructing a simple logic gate based on the presence/absence of mercury and fluoride ions. In digital logic, a '1' typically represents an on state (light on), and a '0' represents an off state (light off). In this system, **Rh-2** initially exhibits a logic '0' with no input (In1: no Al^{3+}/Hg^{2+}, In^2: no CN^-/I^-). Introducing aluminum/mercury ions triggers a transition to logic '1' due to increased fluorescence. Conversely, adding cyanide/iodide ions quenches the emission, resulting in a logic '0' state. Interestingly, the simultaneous presence of both cyanide/iodide and aluminum/mercury ions leads to a decrease in light emission, returning the system to logic '0' (Figure 3.31D). These observations demonstrate the potential of **Rh-2** as a basic logic gate by translating the presence/absence of specific ions into a digital output.

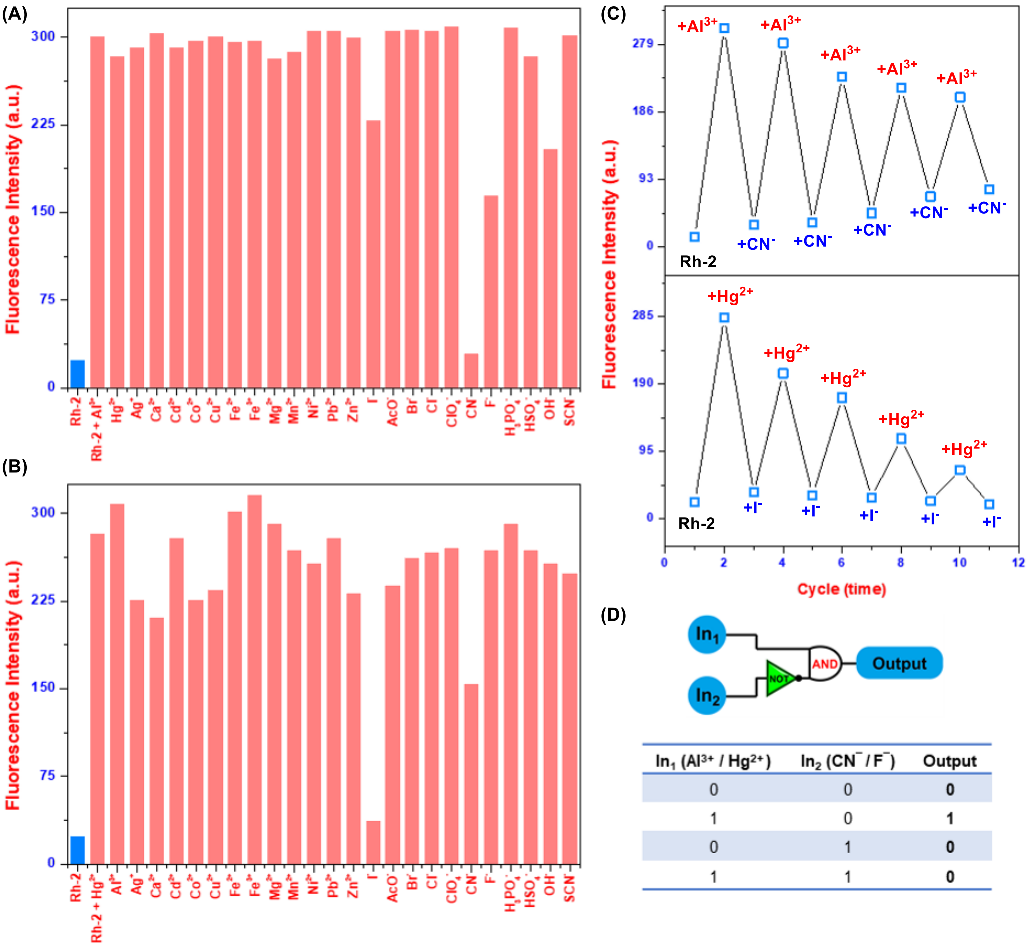

In$_1$ (Al^{3+} / Hg^{2+})	In$_2$ (CN^- / F^-)	Output
0	0	**0**
1	0	**1**
0	1	**0**
1	1	**0**

Figure 3.31. The selectivity of Rh-2 for $Al^{3+}$and Hg^{2+} in the presence of other ions (**A** and **B**) ions, the reversible switching of the fluorescence intensity of Rh-2+Al^{3+} and Rh-2+Hg^{2+} with CN^- and I^- (**C**), and the “IMPLICATION” logic gate (**D**)

Recycling experiments revealed a selective turn-on response of **Rh-2** to aluminum ions in DMSO/Tris (v/v:1/9). Notably, only cyanide ions triggered a turn-off response upon addition to the solution. This switchable on-off behavior suggests the Rh-2+Al^{3+} complex as a potential turn-off sensor for cyanide detection. To quantify cyanide concentration, we performed titration studies similar to previous experiments. As expected, the Rh-2+Al^{3+} emission peak in DMSO/Tris (v/v:1/9) decreased with increasing cyanide concentration, reaching saturation around 3.5 μM cyanide (Figures 3.32A). Building on these observations, we quantified LOD and LOQ for Rh-2+Al^{3+} mediated detection of cyanide under the chosen conditions. The LOD values were determined to be 497 nM, while the LOQ values were 1.51 μM (Figure 3.32B). These findings imply that the Rh-2+Al^{3+} complex serves as an effective quantitative probe for cyanide ion detection.

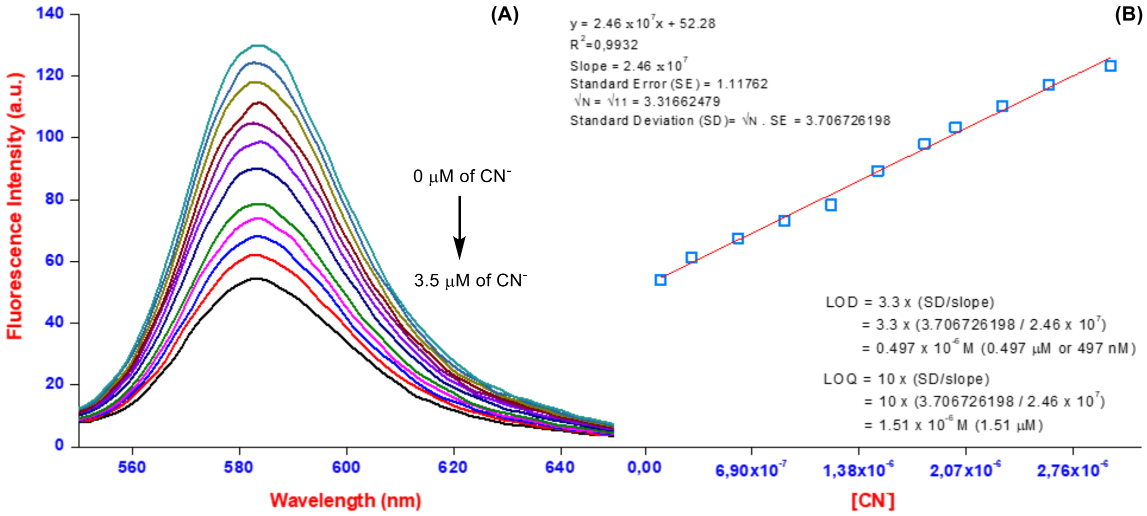

Figure 3.32. The fluorescence titration spectra of Rh-2+Al^{3+} in the presence of CN^- (**A**)**,** and (**B**) the change in fluorescence intensity of the Rh-2+Al^{3+} with the increasing concentration of CN^-

In this thesis study, we also explored the potential of **Rh-2** for naked-eye detection of specific metal ions. Firstly, we tested **Rh-2**'s color-changing properties in various solvents with metal ions. **Rh-2** exhibited a clear color change with mercury in HEPES buffer and with aluminum in Tris buffer (Figures 3.33A and 3.33B), suggesting its use as a visual sensor for these metals in specific environments. To create a user-friendly test for mercury detection, we developed strips by soaking filter paper in an **Rh-2** solution. These strips, when exposed to water containing mercury or aluminum ions (especially both), displayed a rapid and noticeable color change under sunlight or UV light (Figure 3.33C).

Furthermore, we revealed that test papers dyed with Rh-2+Hg^{2+} or Rh-2+Al^{3+} lose color rapidly upon exposure to cyanide. This color change signifies the presence of cyanide, making these dyes valuable for cyanide detection in waste or environmental samples. Overall, this simple and cost-effective method offers a visual approach to detecting mercury, aluminum, and cyanide ions.

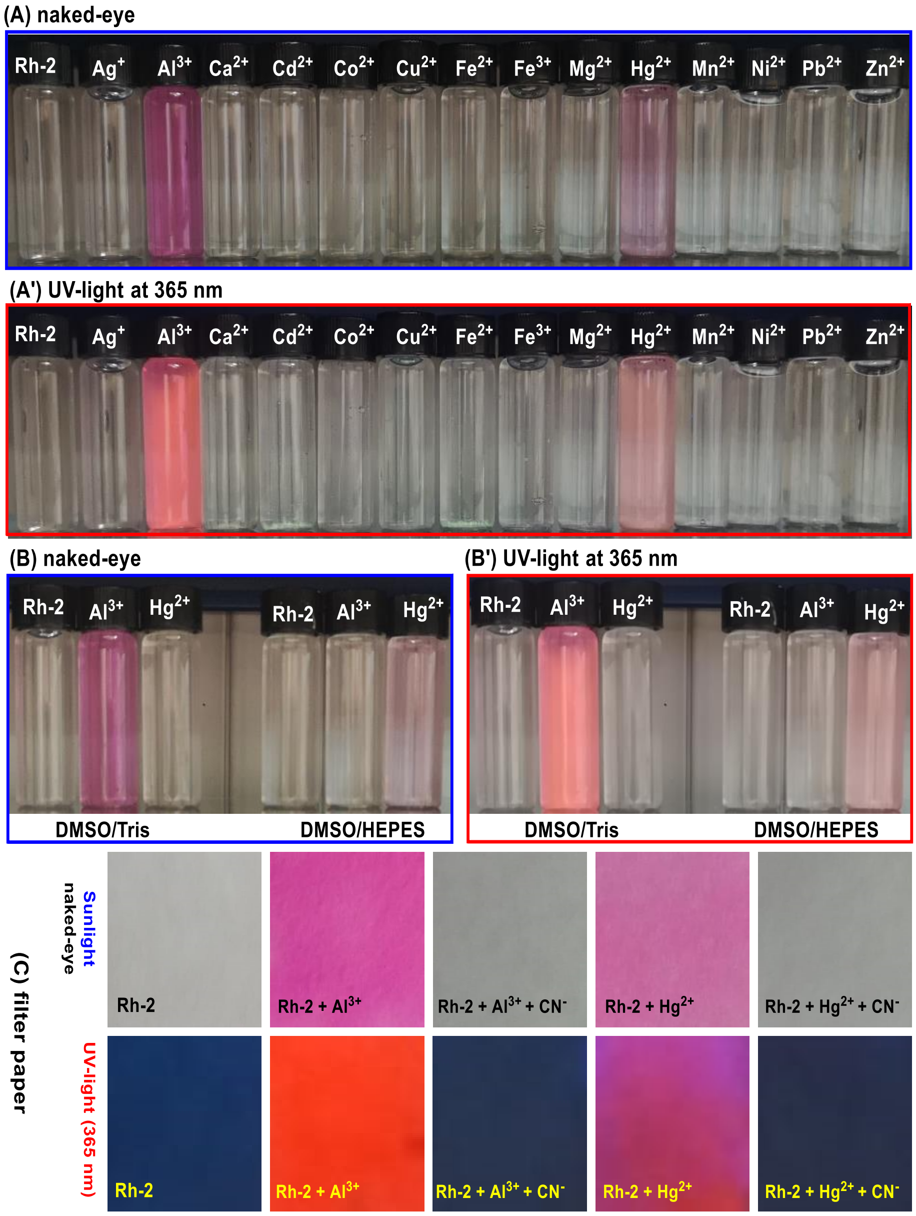

Figure 3.33. The naked-eye (**A** and **B**) and UV light at 365 nm (**A'** and **B'**) color changes of Rh-2 in the presence of metal ions in DMSO/H_2O (v/v: 1/9, pH 7, **A** and **A'**) / DMSO/Tris or HEPES (v/v: 1/9, **B** and **B'**), and (**C**) the photographs depicting the colorimetric response of Rh-2 system

3.2.6. Selectivity and Sensitivity Studies of Rh-3

Following the synthesis of **Rh-3**, our research focused on optimizing **Rh-3** as a sensor for specific ions. We first investigated how different solvents affected its interaction with various ions (Figure 3.34 A). This helped us identify ideal conditions for using unique light absorption properties of **Rh-3** to detect and quantify specific ions. Interestingly, **Rh-3** only interacted with mercury ions in both pure water and real water samples, suggesting its potential as a mercury sensor in real-world applications. Further studies revealed that buffer presence (HEPES) had the same impact, and the probe functioned effectively between pH 2 and 8. However, no interaction occurred between pH 9 and 12 (Figures 3.34B and Ap.35). We then explored the probe's behavior in mixtures of organic solvents (acetonitrile, DMSO, ethanol, methanol, and tetrahydrofuran) and water (Figure Ap.34). While no interaction was observed in pure organic solvents, a specific response towards aluminum ions was detected in aqueous solutions. The fastest response times were achieved in EtOH/H_2O (v/v:1/1) and MeOH/H_2O (v/v:1/1). For environmental considerations, ethanol/water (1:1 v/v) was chosen for further aluminum detection studies. Additionally, time-dependent experiments revealed that mercury ions reached their maximum response within 5 minutes, while aluminum ions required approximately 2-5 minutes (Figures Ap.35). Overall, these preliminary studies demonstrate that **Rh-3** exhibits specific activity towards mercury ions in water and aluminum ions in EtOH/HEPES (v/v:1/1).

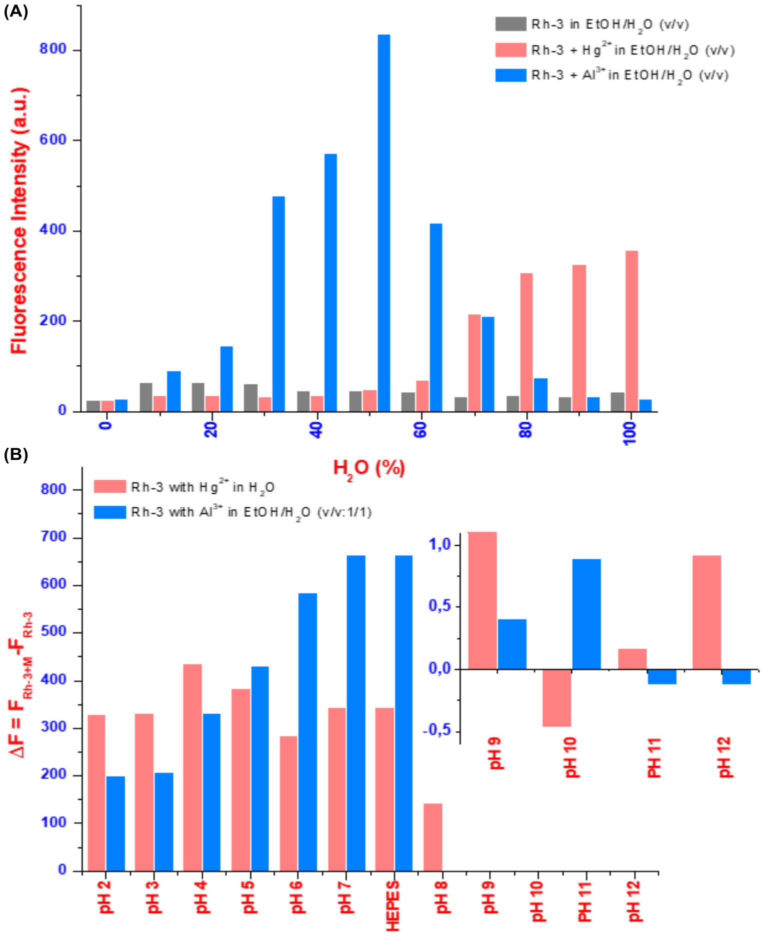

Figure 3.34. Fluorescent responses of Rh-3 with Hg^{2+} and Al^{3+} upon increasing H_2O ratio (**A**) and at different pH values (2–12) (**B**) in the EtOH/H_2O

After optimizing conditions, we optimized conditions for **Rh-3**, another rhodamine-based probe, and used UV-vis and fluorescence spectroscopy to understand how it interacts with metal ions in water and EtOH/HEPES (v/v:1/1). A key indicator in these probes is the emergence of a new peak in the UV-vis spectrum due to the opening of the rhodamine ring upon binding a metal. We monitored **Rh-3** solutions (10 µM) after adding various metal ions (30 µM) in both solvents. In water, only mercury ions trigger ring opening, as evident by a new peak at 552 nm (Figure 3.35A). Similarly, only aluminum ions trigger ring opening, as evident by a new peak at 551 nm in EtOH/H_2O (v/v:1/1) (Figure 3.35B). These reactions also caused color changes from light yellow to violet, demonstrating the potential for colorimetric detection alongside UV-Vis. Fluorescence spectroscopy, performed under the same conditions, confirmed these findings. In water (excited at 550 nm), a new peak at 582 nm appeared only with mercury ions (Figure 3.35A'). This "turn-on" response solidified the selectivity of **Rh-3** for mercury in 100% aqueous media. Additionally, in the ethanol/HEPES mixture, a peak at around 585 nm emerged for aluminum ions, indicating their interaction with **Rh-3** (Figure 3.35B'). These results mirrored the colorimetric observations, highlighting the ability of **Rh-3** to provide clear and consistent signals for aluminum and mercury detection across different spectroscopic methods.

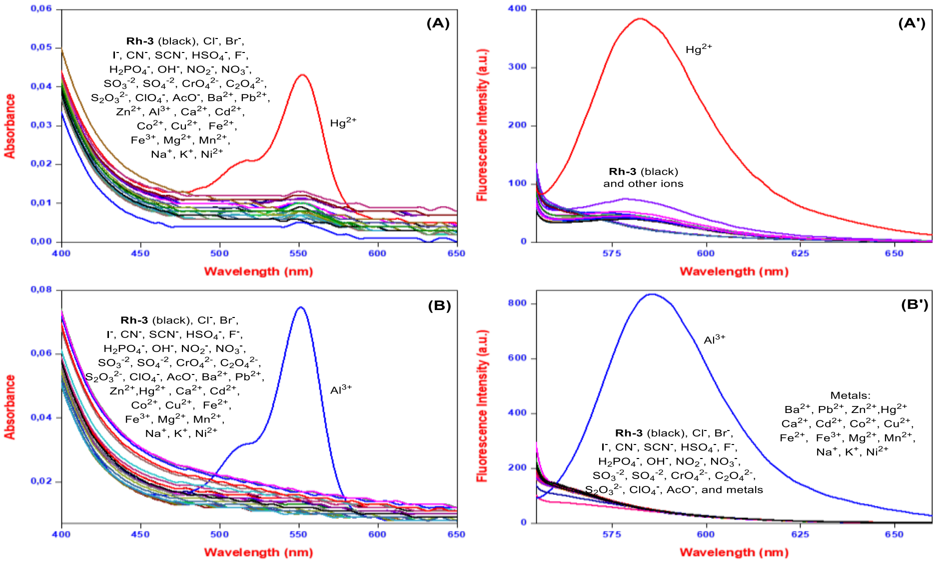

Figure 3.35. The UV-Vis (**A** and **B**), the fluorescence (**A'** and **B'**) spectrums of Rh-3 in the absence and presence of metal ions in HEPES (**A** and **A'**), and EtOH/HEPES (v/v: 1/1, **B** and **B'**)

In this part of our thesis studies, we further explored **Rh-3** potential by examining its sensitivity towards mercury and aluminum ions using fluorescence, building upon our previous work on its light interactions and ion binding. We tested **Rh-3** in both water and EtOH/HEPES (v/v:1/1) solvent systems. The gradual addition (titration) of these metal ions caused a steady increase in **Rh-3** fluorescence intensity. Remarkably, compared to **Rh-3** alone, the fluorescence intensity with high concentrations of aluminum was over 10-times stronger, while mercury showed an over 5-fold increase (Figures 3.36A and 3.36B). This clearly demonstrates **Rh-3** high sensitivity to these specific ions. Taking advantage of this discovery, we then determined the LOD and LOQ for mercury and aluminum using **Rh-3** under the chosen conditions. As shown in (Figures 3.36C and 3.36D), the LOD and LOQ were established as 1.01 µM and 3.10 µM for Hg^{2+}, and 23 nM and 70 nM for Al^{3+}, respectively. These results highlight **Rh-3**, a readily synthesized rhodamine derivative, as a promising and effective quantitative probe for detecting mercury and aluminum ions, with its performance influenced by the chosen solvent system.

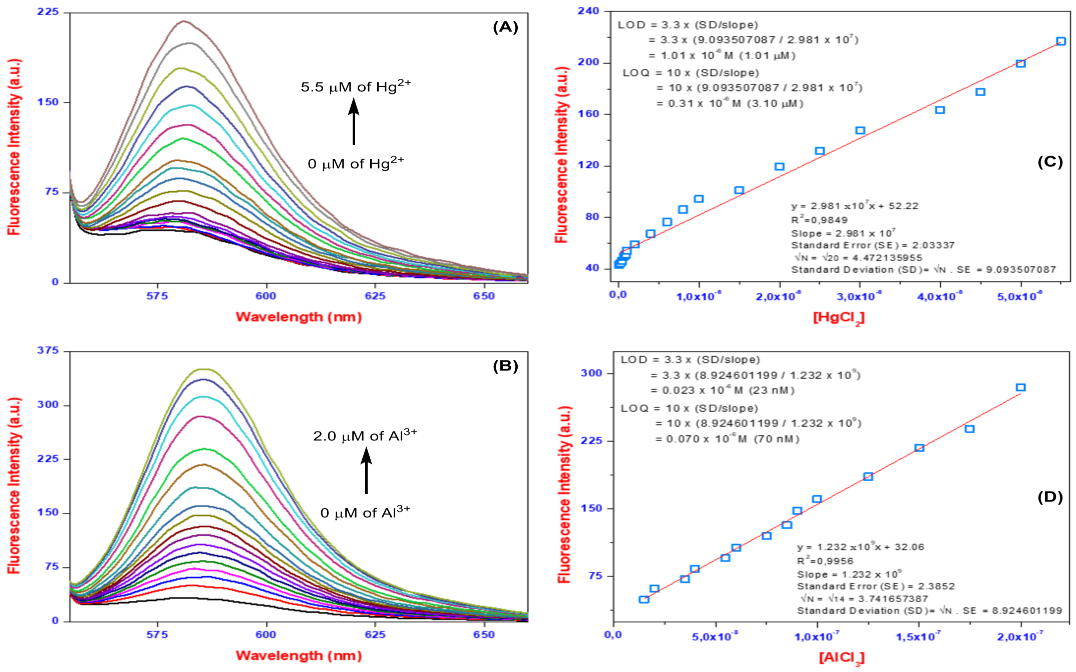

Figure 3.36. The fluorescence titration spectra of Rh-3 in the presence of Hg^{2+} (**A**) / Al^{3+} (**B**), and the change in fluorescence intensity of the Rh-3 with the increasing concentration of Hg^{2+} (**C**) / Al^{3+} (**D**)

To fully understand how **Rh-3** interacts with mercury and aluminum ions, we needed to delve deeper into two crucial aspects: how many ions bind to each **Rh-3** molecule (binding stoichiometry) and how tightly they bind (binding constants). In this context, we used a technique called Job's plot analysis (Figures 3.37A and 3.37B) to determine the binding ratio. This analysis revealed that both aluminum and mercury ions bind to **Rh-3** in a 1:2 ratio, meaning two metal ions bind to each **Rh-3** molecule. Next, we employed the Benesi-Hildebrand plot along with the previously collected fluorescence data (Figures 3.37C and 3.37D) to calculate the K_a for each ion. A high K_a value indicates a strong attraction between the molecule and the ion. The resulting K_a values, 1.30 x 10^{14} M^{-2} for Hg^{2+} and 1.89 x 10^{14} M^{-2} for Al^{3+}, confirm that **Rh-3** binds very strongly to both metal ions.

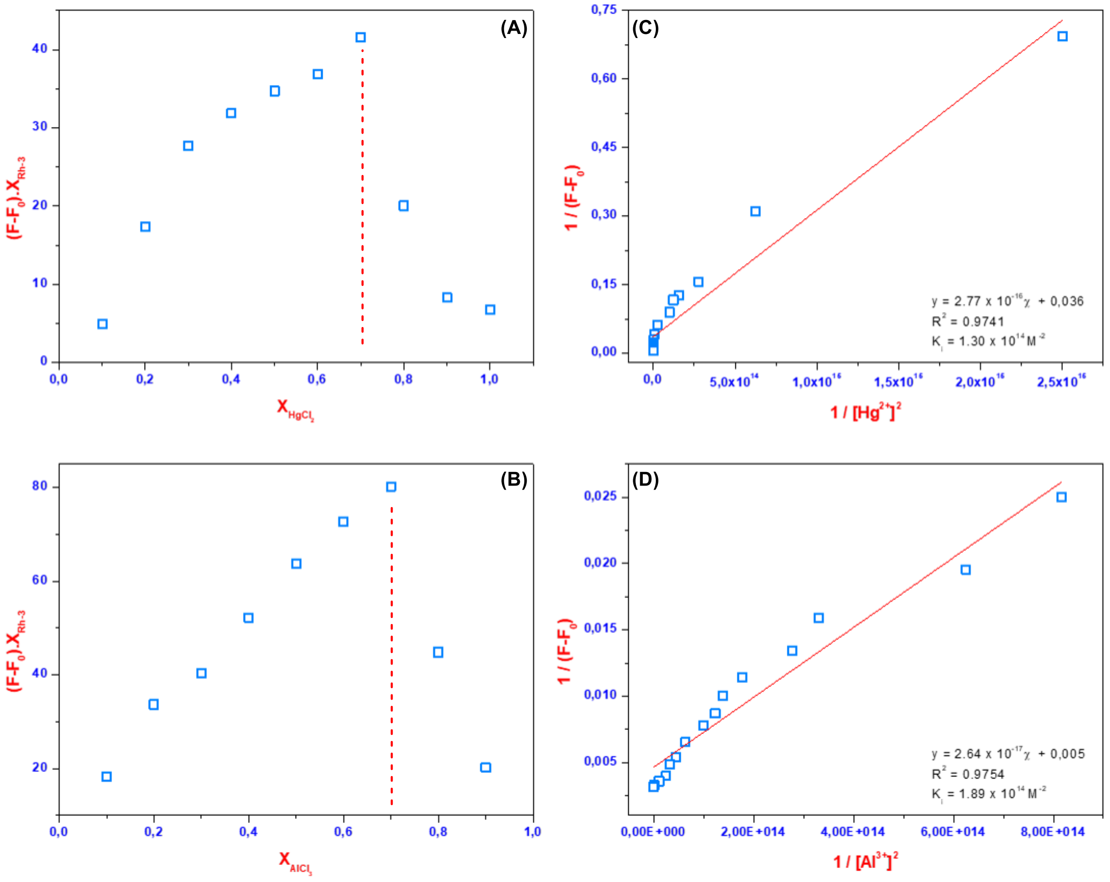

Figure 3.37. The Job's plot of the Rh-3 with $HgCl_2$ (**A**) / $AlCl_3$ (**B**), and the Benesi–Hildebrand plot based on a 1:2 association stoichiometry of Rh-3 with $HgCl_2$ (**C**) / $AlCl_3$ (**D**)

In the continuation of the thesis study designed for the **Rh-3** probe, we wanted to see how **Rh-3** performs in real-world scenarios, where water samples often contain a mix of metal ions. To test its selectivity, we exposed **Rh-3** to both mercury/aluminum and other metals in the same solvent systems used earlier. The good news is that the response of **Rh-3** to mercury/aluminum remained strong even in this competitive environment, indicating minimal interference from other metals. An ideal sensor should also be reversible, allowing for multiple detection cycles. To explore this, we investigated how different anions affect the complexes formed between **Rh-3** and Hg^{2+}/Al^{3+}. Interestingly, adding cyanide/iodine ions for Hg^{2+} and cyanide ions for Al^{3+} caused the fluorescence intensity to decrease (Figures 3.38A, 3.38B, Ap.37, and Ap.38). This quenching effect suggests a potential on/off switch for detection. We tested this by adding and removing cyanide ions (Figure 3.38C). Adding aluminum/mercury ions turned on the fluorescence emission (583 nm) while adding cyanide ions turned it off. Remarkably, we were able to repeat this cycle several times, hinting at the possibility of reusing **Rh-3** to detect not only aluminum/mercury but also cyanide and iodide ions. Following, building on the on/off switching behavior of Rh-3, we explored its potential as a simple logic gate. In the world of computers, a "1" usually means something is on (like a light), and a "0" means it's off. In our system, **Rh-3** starts with a logic "0" when there's no input (no Hg^{2+}/Al^{3+} ions, or no CN^{-} ions). Adding Hg^{2+}/Al^{3+} ions turn it on to a logic "1" because the fluorescence gets brighter. But adding cyanide ions turns the light back off, making it a logic "0" again. Interestingly, if both cyanide and Hg^{2+}/Al^{3+} ions are present at the same time, the light emission goes down, and the system returns to a logic "0" (Figure 3.38D). These findings suggest **Rh-3** could function as a basic logic gate, translating the presence or absence of specific ions into a digital output, like an on/off switch.

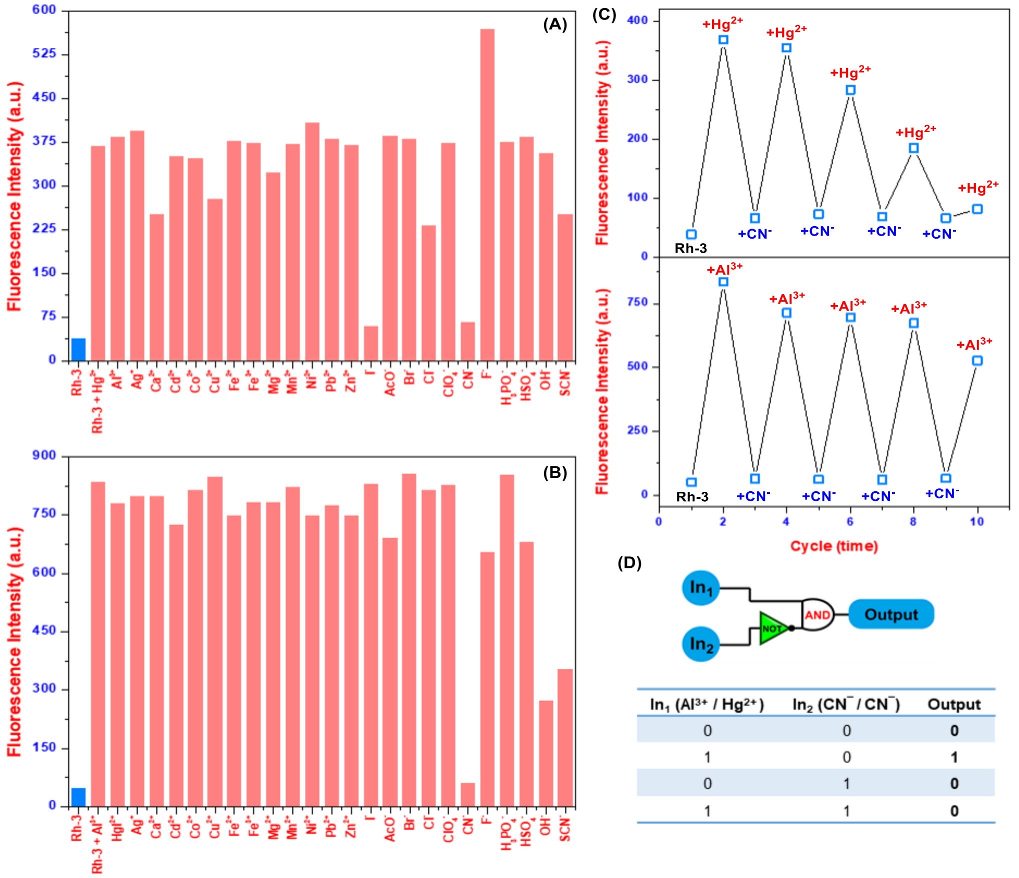

In$_1$ (Al^{3+} / Hg^{2+})	In$_2$ (CN^{-} / CN^{-})	Output
0	0	**0**
1	0	**1**
0	1	**0**
1	1	**0**

Figure 3.38. The selectivity of Rh-3 for Hg^{2+} and Al^{3+} in the presence of other ions (**A** and **B**) ions, the reversible switching of the fluorescence intensity of Rh-3+Al^{3+} and Rh-3+Hg^{2+} with CN^{-} (**C**), and the "IMPLICATION" logic gate (**D**)

Experiments involving repeated use showed that **Rh-3** interacting with aluminum ions in EtOH/HEPES (v/v:1/1) fluoresced up. This suggests that **Rh-3** could be useful for detecting aluminum ions in this solvent mixture. Interestingly, only cyanide ions caused the fluorescence to turn off when added to the solution. This distinct on/off switching behavior makes the Rh-3+Al^{3+} complex a promising candidate for detecting cyanide. To determine the amount of cyanide present, we performed similar experiments to before, gradually adding increasing concentrations of cyanide. As expected, the fluorescence intensity of the Rh-3+Al^{3+} complex in EtOH/HEPES (v/v:1/1) decreased as more cyanide was added, reaching a point where it couldn't decrease further (saturation) at around 10 µM cyanide (Figure 3.39A). Using this data, we calculated the LOD and LOQ for detecting cyanide using Rh-3+Al^{3+} in this solvent system. The LOD was determined to be 738 nM, and the LOQ was 2.24 µM (Figure 3.39B). These results indicate that the Rh-3+Al^{3+} complex effectively functions as a quantitative tool to measure cyanide ion concentration in EtOH/HEPES (v/v:1/1).

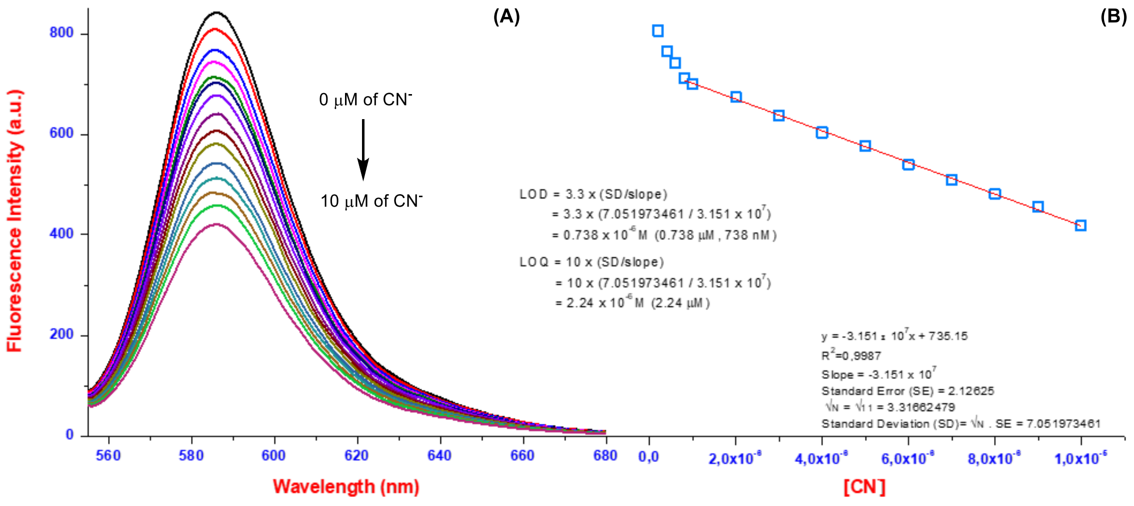

Figure 3.39. The fluorescence titration spectra of Rh-3+Al^{3+} in the presence of CN^- (**A**), and (**B**) the change in fluorescence intensity of the Rh-3+Al^{3+} with the increasing concentration of CN^-

Within the scope of the thesis, **Rh-3** detection features were examined in all their dimensions, and finally, naked-eye and filter paper studies were carried out under this heading. For this purpose, initially, we investigated if **Rh-3** could be used as a simple and effective tool to detect mercury (in H_2O) and aluminum (in EtOH/HEPES, v/v:1/1) ions. Initially, we tested its color-changing properties in various solvents (water, and an alcohol-water mixture). In water, **Rh-3** changed color with mercury. However, the good news is that in the alcohol-water mixture, a clear color change only occurred with aluminum ions (Figures 3.40A and 3.40B). This suggests **Rh-3** can be used as a visual sensor (naked-eye) to detect mercury (in H_2O) and aluminum (in EtOH/HEPES). Following this, we also created easy-to-use test strips for mercury detection. These strips were made by soaking filter paper in a special **Rh-3** solution for a short time. After drying, the strips were exposed to water containing mercury and aluminum ions. When placed in sunlight or under a UV lamp, the strips with **Rh-3** changed color quickly and noticeably, especially when they were dipped in water with both mercury and aluminum ions (Figure 3.40C). This simple and affordable method allows for the visual detection of mercury and aluminum ions. Our experiments also showed that test papers dyed with Rh-3+Hg^{2+} or Rh-3+Al^{3+} lose their color rapidly when dipped in a solution containing cyanide ions. This color change indicates the presence of cyanide, making these dyes useful for cyanide detection in waste or environmental samples. Overall, it can be said that using **Rh-3** to develop sensors for mercury and aluminum detection in a water/water-alcohol mixture shows great promise for fast and easy testing.

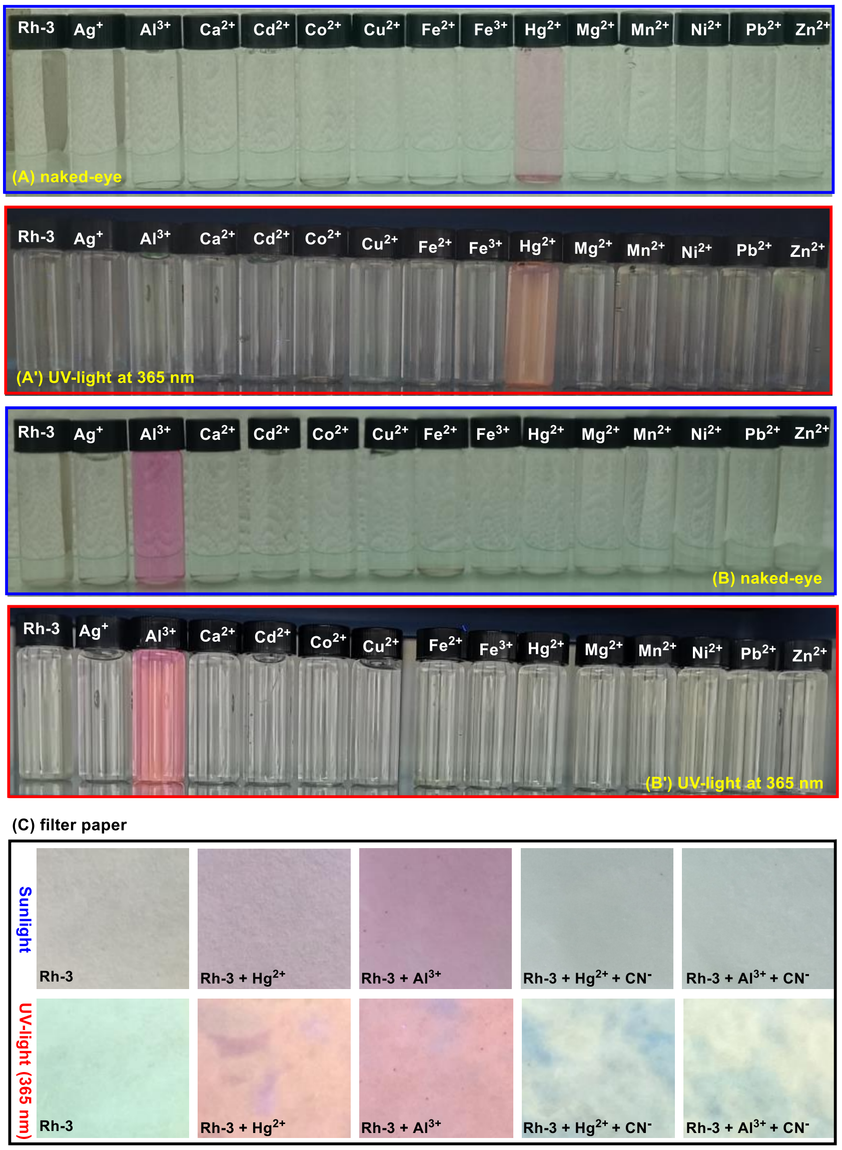

Figure 3.40. The naked-eye (**A** and **B**) and UV light at 365 nm (**A'** and **B'**) color changes of Rh-3 in the presence of metal ions in H_2O (**A** and **A'**) / EtOH/H_2O (v/v: 1/1, with HEPES, **B** and **B'**), and (**C**) the photographs depicting the colorimetric response of Rh-3 systems

4. CONCLUSIONS

In conclusion, this thesis explored the synthesis of novel organic probes based on phenolphthalein (**PP**) and rhodamine B (**RhB**), two increasingly popular platforms (Scheme 15). By incorporating commonly used side groups, these probes offer the potential for diverse functionalities. The impact of these side groups on the overall sensing mechanism was also investigated.

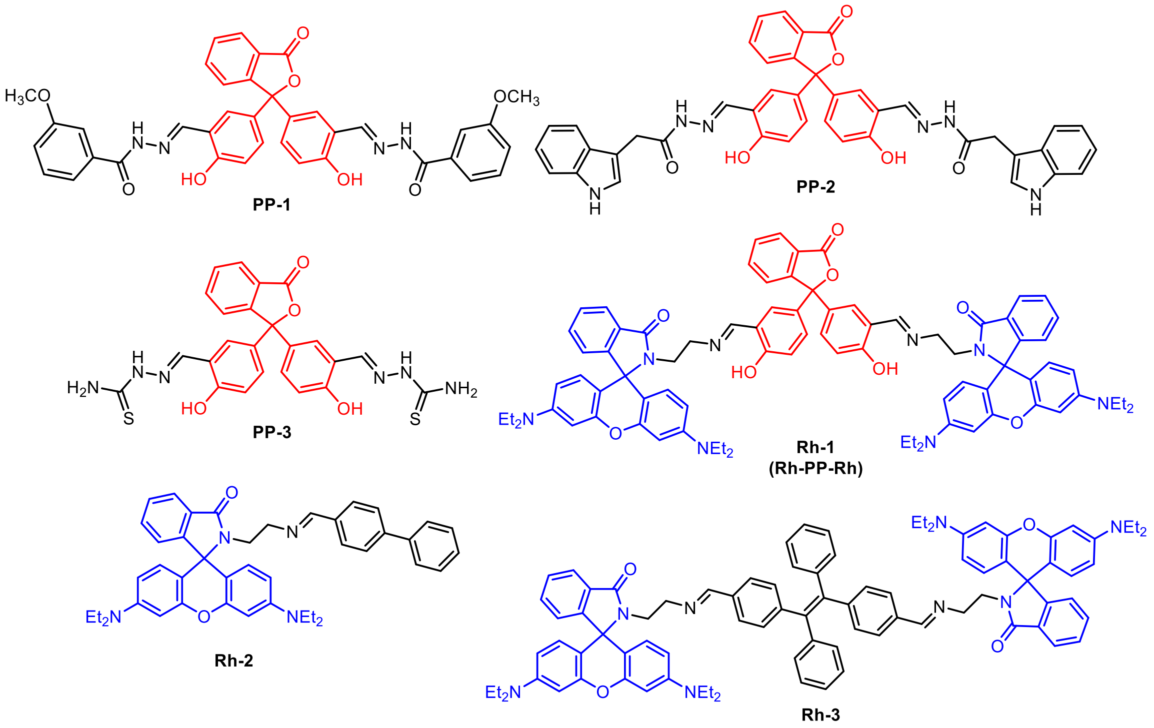

Scheme 15

The interaction of the newly synthesized phenolphthalein and rhodamine derivatives with various ions was comprehensively investigated. Colorimetric, UV-vis/fluorescence spectroscopy and theoretical calculations were employed to elucidate the binding mechanism. Additionally, FT-IR, mass, and ^{1}H-NMR spectroscopy provided further insights. To optimize selectivity and sensitivity, a range of operating conditions were explored, including solvent systems, pH, time, and temperature. These studies revealed specific affinities for certain ions, dependent on the solvent and pH. For instance, probe **PP-1** displayed multi-ion interaction with cadmium, zinc, and aluminum in EtOH/H_2O (v/v:1/1) at pH 7 (or HEPES buffer). However, at pH 5, **PP-1** selectively interacted with aluminum, and at pH 9, with zinc. Similarly, probe **PP-2** exhibited activity towards zinc ions in EtOH/H_2O (v/v:1/1, pH 7), but displayed specific selectivity for cadmium ions in EtOH/H_2O (v/v:9/1, pH 9). Unlike **PP-1** and **PP-2**, **PP-3** exhibited a turn-off response towards copper and mercury ions in real water samples across various solvent-to-water ratios. This suggests that **PP-3** is a potential sensor candidate for these metal ions in real-world applications. Notably, the observed behavior highlights the influence of side group diversity on the sensing mechanism. While **PP-1** and **PP-2** possess arene/heteroarene-substituted hydrazine groups, **PP-3** incorporates hydrophilic thiosemicarbazone (TSC) derivatives. These TSC groups likely enhance water solubility and promote aggregation. This suggests that **PP-3** aggregates significantly in water, and this aggregation is disrupted upon interaction with mercury or copper ions. This thesis also explored rhodamine-based organic probes alongside the phenolphthalein derivatives. Compared to phenolphthaleins, rhodamines exhibit a characteristic UV-Vis absorption peak around 520-550 nm, attributed to the open-form rhodamine unit arising from interactions with specific ions. This interaction is further evidenced by a dramatic color change from colorless to purple-violet, making all synthesized rhodamine derivatives suitable for colorimetric detection. Similar to the phenolphthalein probes, environmental conditions (solvent, time, pH) were optimized for the rhodamines. Studies generally revealed interactions leading to ring opening upon exposure to Fe^{2+}, Fe^{3+}, Cu^{2+}, Al^{3+}, and Hg^{2+} ions in organic solvents. Notably, the **Rh-1** (**Rh-PP-Rh**) probe incorporates both phenolphthalein and rhodamine moieties condensed onto a single structure. This unique design makes **Rh-1** particularly interesting in this thesis. Optimization studies of **Rh-1** demonstrated selective interaction with mercury ions in EtOH/H_2O (v/v, from 5/5 to 0/10). Despite sharing structural features like biphenyl and tetraphenylethylene (TPE) groups, **Rh-2** possesses a single rhodamine unit, while **Rh-3** incorporates two. Interestingly, while both probes displayed interactions with multiple ions in pure organic solvents, specific interactions emerged in H_2O, DMSO/H_2O, and EtOH/H_2O mixtures, with the choice of buffer (Tris or HEPES) further influencing selectivity towards aluminum and mercury ions. **Rh-2** exhibited a strong preference for aluminum in DMSO/Tris (1:9 v/v), while in DMSO/HEPES (1:9 v/v), it showed a stronger interaction with mercury and a weaker one with aluminum. In contrast, **Rh-3** displayed specific binding only towards Hg^{2+} ions in both real and pure water samples. Notably, in EtOH/HEPES (v/v, from 7/3 to 6/4) solutions, it selectively interacted solely with Al^{3+} ions. Additionally, time studies play a crucial role in optimizing the interaction. We found that probes-ions interactions reach their peak between 2 and 15 minutes. Consequently, optimization studies were conducted for all synthesized derivatives to determine the ideal environmental conditions for quantitative analysis.

Tablo 4.1. The optimization studies of probes

Probes	**Sensing ions**	**Solvent Medium (v/v)**	**pH values**	**Practical application**	**Times (Min.)**
PP-1	Al^{3+}	EtOH/H_2O (1/1)	pH 5	Real water	15.00
	Zn^{2+}	EtOH/H_2O (1/1)	pH 9	Real water	7.00
	Cd^{2+}	EtOH/H_2O (1/1)	pH 7	Real water	15.00
PP-2	Zn^{2+}	EtOH/H_2O (1/1)	pH 7	Real water	1.00
	Cd^{2+}	EtOH/H_2O (9/1)	pH 7	Real water &Smoking	5.00
PP-3	Cu^{2+}	H_2O	HEPES	Real water	2.00
	Hg^{2+}	H_2O	HEPES	Real water	2.00
Rh-1	Hg^{2+}	EtOH/H_2O (1/1)	pH 7	Real water	12.00
Rh-2	Al^{3+}	DMSO/Tris (1/9)	Tris	Real water	15.00
	Hg^{2+}	DMSO/HEPES (1/9)	HEPES	Real water	5.00
Rh-3	Al^{3+}	EtOH/H_2O (1/1)	HEPES	Real water	5.00
	Hg^{2+}	H_2O	HEPES	Real water	5.00

After extensive optimization and studies of interaction kinetics, we investigated probe interactions with various ions under controlled environmental conditions using UV-Vis and fluorescence spectroscopy. Titration experiments were performed under these same conditions to confirm qualitative observations and quantify binding affinities (important for identifying optimal sensor candidates). From the titration and Job Plot analyses, we calculated the LOD, LOQ, and K_a values for each probe-metal interaction. These results suggest that probes with LOD values ranging from 23 nM to 554 nM for Al^{3+} could be effective for detecting aluminum in wastewater samples. Similarly, it was determined that the LOD values for other ions changed from 1.01 mM to 334 nM for Hg^{2+}, from 64 nM to

550 nM for Zn^{2+}, and from 15 nM to 551 nM for Cd^{2+}. Additionally, the LOD value of PP-3 for Cu^{2+} was calculated as 1.56 mM. These values are all below the maximum permissible levels set by the World Health Organization (WHO) for these ions in water, indicating their potential for environmental monitoring. Additionally, calculated LOQ and K_a values complete a comprehensive quantitative analysis of the binding interaction.

Tablo 4.2. The selectivity of the probes in the presence of ions and quantitative characteristics

Probes	**Sensing ions**	**Job's Plot (Probe/ion)**	**LOD (μM)**	**LOQ (μM)**	**K_a values**
PP-1	Al^{3+}	1/2	0.033	0.10	2.68×10^{14} M^{-2}
	Zn^{2+}	1/2	0.064	0.193	6.15×10^{14} M^{-2}
	Cd^{2+}	1/2	0.550	1.67	5.49×10^{15} M^{-2}
PP-2	Zn^{2+}	1/2	0.550	1.66	1.31×10^{17} M^{-2}
	Cd^{2+}	1/2	0.015	0.045	4.23×10^{14} M^{-2}
PP-3	Cu^{2+}	2/1	1.56	4.72	1.94×10^{4} $M^{-1/2}$
	Hg^{2+}	2/1	0.117	0.357	7.98×10^{4} $M^{-1/2}$
Rh-1	Hg^{2+}	1/2	0.334	1.01	9.33×10^{11} M^{-2}
Rh-2	Al^{3+}	1/1	0.554	1.68	1.53×10^{5} M^{-1}
	Hg^{2+}	1/1	0.366	1.11	6.37×10^{4} M^{-1}
Rh-3	Al^{3+}	1/2	0.023	0.070	1.89×10^{14} M^{-2}
	Hg^{2+}	1/2	1.01	3.1	1.30×10^{14} M^{-2}

Beyond basic detection, we investigated the probes' performance in real-world scenarios with mixed metal ions. Pleasingly, the presence of other cations didn't hinder specific metal ion detection (Table 4.3). However, some anions (CN^-, SCN^-, F^-) and the molecule GSH reversed the probe-metal interaction. Interestingly, the reversibility of this interaction varied. The PP-1-Al^{3+} complex could be recycled up to seven cycles using hydroxide ions, while PP-2-Cd^{2+} showed irreversible recycling with CN^- and SCN^-. PP-3-Cu^{2+} couldn't be recycled with common ions but achieved seven cycles with GSH. On the other hand, probe-Hg^{2+} complexes generally recovered with iodine and Rhs-Al^{3+} complexes with CN^-. This reversible binding not only allows probe reuse but also suggests a potential for these complexes as sensors for CN^-, SCN^-, and GSH. Subsequent titration studies with these anions yielded sensitive LOD and LOQ values, demonstrating their promise for target anion and GSH detection. Another feature that an effective sensor candidate must have been that it can be used on real samples. In this context, to assess their real-sample potential, the probes were tested with actual water samples and cigarette smoke for target metal ion detection. These experiments yielded promising results, demonstrating the probes' ability to function in complex matrices.

Furthermore, colorimetric studies were conducted in solvents and on filter paper to evaluate practical usability. These studies provided strong evidence that the probes can be readily applied in field settings. Finally, to understand the binding mechanisms between probes and target ions, theoretical calculations, mass spectrometry, FTIR, and ^{1}H-NMR spectroscopy were employed. The resulting data aligned with observations of similar probe skeletons reported in the literature, providing valuable insights into the interaction process.

Tablo 4.3. The selectivity and reversible switching of the complex in the presence of anions

Complex	Sensing ions	pH value	Cycle (time)	LOD (μM)
PP-1 + Al^{3+}	OH$^-$	pH 5	7	ND
PP-2 + Cd^{2+}	CN$^-$	pH 9	no cycle	0.729
PP-2 + Cd^{2+}	SCN$^-$	pH 9	no cycle	1.44
PP-3 + Hg^{2+}	I$^-$	HEPES	4	ND
PP-3 + Cu^{2+}	GSH	HEPES	7	1.80
Rh-1 + Hg^{2+}	F$^-$	pH 7	4	ND
Rh-1 + Hg^{2+}	I$^-$	pH 7	no cycle	ND
Rh-2 + Al^{3+}	CN$^-$	Tris	6	0.497
Rh-2 + Hg^{2+}	I$^-$	HEPES	5	ND
Rh-3 + Al^{3+}	CN$^-$	HEPES	6	0.738
Rh-3 + Hg^{2+}	CN$^-$	HEPES	4	ND
Rh-3 + Hg^{2+}	I$^-$	HEPES	no cycle	ND

ND: not determined

Overall, this study successfully developed practical and fast organic probes for detecting key environmental pollutants (Al^{3+}, Hg^{2+}, Cu^{2+}, Cd^{2+}, Zn^{2+}, CN$^-$, SCN$^-$), and the biological agent GSH within relevant concentration ranges. These probes demonstrated effectiveness in real samples, paving the way for their potential applications in monitoring both environmental and biological systems.

REFERENCES

Ali, S., Thaku, S .K., Sarkar, A., and Shekhar, S. (2016). Worldwide contamination of water by fluoride. *Environ.Chem. Lett*, 14, 291-315.

Alici, O., and Aydin, D. (2021). A Schiff-base receptor based on phenolphthalein derivate appended 2-furoic hydrazide: Highly sensitive fluorogenic “turn on” chemosensor for Al^{3+}. *Journal of Photochemistry & Photobiology A: Chemistry,* 404, 112876.

Aydin, D., and Alici, M. K. (2021). Phenolphthalein Conjugated Schiff Base as a Dual Emissive Fluorogenic Probe for the Recognition Aluminum (III) and Zinc (II) Ions. *Journal of Fluorescence,* 31, 797-805

Ayoob, S., and Gupta, A. (2006). Fluoride in Drinking Water: A Review on the Status and Stress Effects. Crit. Rev. *Environ. Sci. Technol,* 36, 433-487.

Bayindir, S., and Hussein, A. S. (2024). Off-On–Off Cascade Recognition of Cyanide, Mercury, and Aluminum Using N /5-Monosubstituted Rhodanines.*ACS Omega,* 9, 17602-17615

Bayindir, S., Hussien, A. S., Lafzi, F., and Toprak, M. (2023). he switchable fluorescent detection of mercury, copper, and iodine in real water samples using bola-amphiphilic-tetraphenylethene. *Journal of Molecular Liquids*, 382, 121939.

Bayindir, S., Saracoglu, N. (2016). A facile one-pot method to synthesise 2-alkylated indole and 2, 2′-bis (indolyl) methane derivatives using ketones as electrophiles and their anion sensing ability. *RSC advances,* 6, 72959-72967.

Bernard, V., and Isabelle, L. (2000). Design principles of fluorescent molecular sensors for cation recognition. *Coord. Chem Rev*, 205, 3-40.

Björkman, L., Lundekvam, F., Laegreid, T., Bertelsen, I., Morild, I., and Lilleng, P. (2007). Mercury in human brain, blood, muscle and toenails in relation to exposure an autopsy study. *Environ, Health,* 6, 30.

Chandra, S., Lokesh, K., and Lang, H. (2006) . Lodide recognition by the N,N-bis-succinamide-based dendritic molecule $[CH_2C(O)NHC(CH_2CH_2C(O)OtBu)_3]_2$. *Sensors and Actuators B: Chemical* , 137, 350-355.

Chua, M., Zhou, H., Zhu, Q., Tang, B. Z., and Xu, J. W. (2021). Recent advances in cation sensing using aggregation-induced emission. *Materials Chemistry Frontiers,* 5, 659-708.

Clarkson, T. W., and Magos, L. (2006). The toxicology of mercury and its chemical compounds. *Crit. Rev, Toxicol,* 36, 609-662.

Covington, A. K., and Dickinson, T. (1973). *Physical Chemistry of Organic Solvint Systems,*1-22.

Dinatale, F., Lancia, A., Molino, A., Dinatale, M., Karatza, D., and Musmarra, D. (2006). Capture of mercury ions by natural and industrial materials. *Journal of hazardous materials,* 132, 20-225.

Duygu, A., and Meliha, K. (2021). Phenolphthalein Conjugated Schiff Base as a Dual Emissive Fluorogenic Probe for the Recognition Aluminum (III) and Zinc (II) Ions. *Journal of Fluorescence,* 31, 797-805.

Elkhatat, A M., Soliman, M., Ismail, R., Ahmed, S., Abounahia, N., and Mubashir, S. (2021). Recent trends of copper detection in water samples. *Bull Natl Res Cent,* 45, 218.

Elmas, S. N. K.; Karagoz, A.; Aydin, D.; Arslan, F. N.; Sadi, G.; and Yilmaz, I. (2021). Fabrication and sensing properties of phenolphthalein based colorimetric and turn–on fluorogenic probe for CO_3^{2-} detection and its living–cell imaging application, *Talanta,* 226, 122166.

Erdemira, S., and Kocyigit, O. (2017). A novel dye based on phenolphthalein-fluorescein as a fluorescent probe for the dual-channel detection of Hg^{2+} and Zn^{2+}. *Dyes and Pigments,* 145, 72-79.

Erdemira, S., and Malkondu, S. (2021). Dual-emissive fluorescent probe based on phenolphthalein appended diaminomaleonitrile for Al^{3+} and the colorimetric recognition of Cu^{2+}. *Talanta,* 226, 122166.

Gorchev, H. G., and Ozolins, G. (2004). Guidelines for Drinking-water Quality, 3rd Edition, Who. 1 (2004) 564. H.G. Gorchev, G. Ozolins, Guidelines for Drinking-water Quality, 3rd Edition. *WHO,* 1, 564.

Gunnlaugsson, T., Glynn, M., Tocci, G. M., Kruger, P E., and Pfeffer, F M. (2006). Anion recognition and sensing in organic and aqueous media using luminescent and colorimetric sensors. *Coordination Chemistry Reviews* , 250, 3094-311.

Hussein, A. S., Lafzi, F., Bayindir, S., Kilic, H., and Toprak, M. (2023). A Novle Rhodamine-Phenolphthalein Architecture for Selective Mercury Ion Detection in Media. *Chem Plus Chem,* 89, 202300649.

Hussein, A. S., Lafzi, F., Bayindir, S., and Toprak, M. (2023). The selective turn-on recognition of fluoride ions using 5-aryl-rhodanines: Colorimetric & fluorescent detection. *Journal of Photochemistry and Photobiology A: Chemistry,* 438, 114574.

Hussein, A. S., Lafzi, F., Kilic, H., and Bayindir, S. (2023). Synthesis of Bis-tetraphenylethene as a Novel Turn-On Selective Zinc Sensor. *ACS Omega,* 8, 2543225440.

International Agency for Research on Cancer (IARC). (1993) Beryllium, cadmium, mercury and exposures in the glass manufacturing industry. *IARC, Lyon,* 58.

Jagadhane, K. S., Bhosale, S. R., Gunjal, D. B., Nille, O. S., Kolekar, G. B., and Anbhule, P. V. (2022). Tetraphenylethene-Based Fluorescent Chemosensor with Mechanochromic and Aggregation-Induced Emission (AIE) Properties for the Selective and Sensitive Detection of Hg^{2+} and Ag^{2+} Ions in Aqueous Media: *Application to Environmental Analysis, ACS Omega,* 7, 34888-34900.

Kalcher, K., Kern, W., Piestch R. (1993). Cadmium and lead in the smoke of a filter cigarette. *Sci Total Environ,* 1, (28), 21-35.

Kim, S., Noh, J., Kim, K., Kim, J., Kang, H., Nam, S., Kim, S., Park, S., Kim, C., and Kim, J. (2012). Salicylimine-based fluorescent chemosensor for aluminum ions and application. *J. Inorgnic Chem,* 51, 3597-3602.

Kollur, S. P., Shivamallu, C., Prasad, S. K., Veerapur, R., Patil, S. S., Cull, C. A., Coetzee, J. F., and Amachawadi, R. G. (2021). Recent Advances on the Development of Chemosensors for the Detection of Mercury Toxicity: A Review. *J. Separations,* 8, 192.

Kong, X. U.; Hou, L. J.; Shao, X. Q.; Shuang, S. M.; Wang, Y.; and Dong, C. (2019). A phenolphthalein-based fluorescent probe for the sequential sensing of Al^{3+} and F^{-} ions in aqueous medium and live cells. Spectrochimica Acta Part A: *Molecular and Biomolecular Spectroscopy,* 208, 131–139.

Kong, X. U.; Shuang, S. M.; Wang, S. Y.; and Dong, C. (2022). A novel phenolphthalein-based fluorescent chemosensor for pyrophosphate detection via an Al3+ displacement approach in real samples and living cells. *Spectrochimica Acta Part A: Molecular and Biomolecular Spectroscopy,* 276, 121174.

Kubier, A., Wilkin, R. T., and Pichler, T. (2019). Cadmium in soils and groundwater: a review. Appl. Geochem, 108, 104388.

Lafzi, F., Hussein, A. S., H, Kilic, H., and Bayindir, S. (2023). The thioacetal-modified phenothiazine as a novel colorimetric and fluorescent chemosensor for mercury in aqueous media. *Journal of Photochemistry and Photobiology A: Chemistry,* 444, 114958.

Li, M.; Lv, H. S.; Luo, J. Z.; Miao, J. Y.; Zhao, B. X. (2013). An effective "turn-on" rodamine-based fluorescent chemosensor forCu (II) in living cells. *Sensors and Actuators* B, 188, 1235-1240.

Li, Y., Feng, Z., Peng, Q., Yang, C., He, J., and Li, K. (2019). An AIEgen-based luminescent photo-responsive system used as concealed anti-counterfeit material. *J. Lumin,* 216, 116750.

Liwei, X., Lilei, R., Xuemin, J., Zheng, L., Shaoguang, W., and Dingyi, G. (2020). A selective naphthalimide-based colorimetric and fluorescent chemosensor for "naked-eye" detection of fluoride ion. *Inorg. Chim,* 500, 119207.

Lundquist, P., Rosling, H., Sorbo, B., and Tibbling, L. (1987). Cyanide concentrations in blood after cigarette smoking, as determined by a sensitive fluorimetric method. *Clin.Chem*, 33, 1228-1230.

Maguire, A., and Zohoori, F. V. (2013). Fluoride balance in infants and young children in the UK and its clinical relevance for the dental team. *British Dental Journal,* 214, 587-593.

Maguire, A., Omid, N., Abuhaloob, L., Moynihan, P. J., and Zohoori, F. V. (2012). Fluoride content of ready-to-feed (RTF) infant food and drinks in the UK, Community Dent. *Oral Epidemiol,* 40, 26-36.

Maity, A., Ghosh, U., Dipanjan, G., Mukherjee, D., Maiti, T. K., and Patra, S. K. (2019). A water Soluble Bodipy based 'Off/On' fluorescent probe for the detection of Cd^{2+} ions with high selectivity and sensitivity. *Dalton Trans,* 48, 2108-2117.

Momidia, B., Tekuria, V., and Trivedi, D. (2016). Selective detection of mercury ions using benzothiazole based colorimetric chemosensor. *Inorgan. Chem. Comm,* 74, 1-5.

Monago, C., Uwakwe, A., Dede, E. (2005). Comparative analysis of cyanide content of some tobacco products in Nigeria. *Global Journal of Pure and Applied Sciences,* 11, 487-490.

Morgan, J. C., Byron, M. J., Baig, S. A., tepanov, I. S., and Brewer, N. T. (2017). How people think about the chemicals in cigarette smoke a systematic review. *Journal Behav.* Med, 40, 553-564.

Naila, A., Meerdink, G., Jayasena, V., Sulaiman, A. Z., Ajit, A. B., Berta, G. (2019). A review on global metal accumulators-mechanism, enhancement, commercial application, and research trend. *Environmental Science Pollutıon Research,* 26, 26449-26471.

Nstitute of Medicine (2001). "Zinc". Dietary Reference Intakes for Vitamin A, Vitamin K, Arsenic, Boron, Chromium, Copper, Iodine, Iron, Manganese, Molybdenum, Nickel, Silicon, Vanadium, and Zinc. *Washington, DC: National Academy Press,*501 , 4-21.

Piade, J. J., Jaccard, G., Dolka, C., Belushkin, M., and Wajrock, S. (2015). Differences in cadmium transfer from tobacco to cigarette smoke compared to arsenic or lead. *Toxicol Rep,* 2, 12-26.

Roohani, N., Hurrell, R., Kelishadi, R., and Schulin, R. (2013). Zinc and its importance for human health: An integrative review. *Journal of Research in Medical Sciences*, 18, 144-157.

Rosseland, B. O., Eldhuset, T. D., Staurnes, M. (1990). *Environmental effects of aluminium. Environ Geochem Health*, 12, 17-27.

Shi, X., Wang, H., Han, T., Feng, X., Tong, B., Shi, J., Zhi, J., and Dong, Y. (2012). A highly sensitive, single selective, real-time and “turn-on” fluorescent sensor for Al^{3+} detection in aqueous media. *Journal Mater Chem,* 22, 19296.

Sikdar, A., Roy, S., Haldar, K., Sikdar, S., and Panj, S. (2013). Rhodamine-Based Cu^{2+} Selective Fluorosensor: Synthesis, Mechanism, and Application in Living Cells. *Journal of Fluorescence*, 10895, 013-1169.

Sikdar, S., and Kundu, M. (2018). A review on detection and abatement of heavy metals. *Chembioeng reviews*, 5, 18-29.

Song, F., Liu, H., Gao, Z., Zhu, J., and Kan, C. (2018). Dual-binding pyridine and rhodamine B conjugate derivatives as fluorescent chemosensors for Ferric ion in aqueous media and living cells. *Analyst,* 01, 1-3.

Sukhvinder, D., Manzoor, A., Nancy, S., Gulshan K., Prabhpreet, S., Vijay, L., and Navneet, K., and Subodh, K. (2020). Chemodosimeters for optical detection of fluoride anion. *Coord. Chem. Rev,* 405, 213-218.

Tang, L., Yu, H., Zhong, K., and Gao X, (2019). An aggregation-induced emission-based fluorescence turn-on probe for Hg^{2+} and its application to detect Hg^{2+} in food samples. *RSC Advances*, 40, 553-564.

Tang, Y., Huang, Y., Chen, Y., Lu, L., Wang, C., Sun, T., Wang, M., Zhu, G., Yang, Y., Zhang, L., and Zhu, J. (2019). A coumarin derivative as a "turn-on" fluorescence probe toward Cd^{2+} in live cells. *Spectrochim,* 218, 359-365.

Tapiero, H., Townsend, D., and Tew, K. (2003). Trace elements in human physiology and pathology Copper. *Biomed Pharmacother,* 57, 386-98.

Thakur, A., Bhatta, S. R., Mondal, B., Kakash, D., and Chawla, P. (2018). Naphthalene-glycine conjugate: An extremely selective colorimetric chemosensor for iodide ion in aqueous solution. *Sensors and Actuators B: Chemical*, 267, 617-626.

Toprak, M., Lafzi, F., and Bayindir, S. (2021). Water-ratio directed selective turn-on fluorescence detection of copper and mercury in acetonitrile. *Journal of Photochemistry and Photobiology A: Chemistry,* 418, 113418.

Trevino, K. M., Wagner, C. R., Tamura, E. K., Garcia, J., and Louie, A. Y. (2023). Small molecule sensors for the colorimetric detection of Copper (II): A review of the literature from 2010 to 2022. *Dyes and Pigments*, 214, 110881.

Tsakilas, C. D., Karaivazofou, N. A., Tsotsolis, N. C., Stamatiadis, S., and Smaras, V. (2005). Cadmium uptake by tobacco as affected by liming, N form, and year of cultivation. *Environ. Pollut*, 134, 239-246.

United States Environmental Protection Agency. (2020) U.S. EPA Office of the Federal Register, National Archives and Records, Administration National Primary Drinking Water Regulations Protection of Environment. *United States Environmental Protection Agency*, 40 (25) 141.

Wan, X., Ke, H., Tang, J., Yang, G. (2019). Acid environment-improved fluorescence sensing performance: a quinoline Schiff base-containing sensor for Cd^{2+} with high sensitivity and selectivity. *Environmental Materials Chemistry and Physics*, 199, 8-13.

Wang, P., Chen, K., and Ge, Y. (2019). Peptide-based ratiometric fluorescent probe for highly selective detection of Cd (II) and its application in bioimaging. *Journal Luminesc,* 208, 495-501.

World Health Organization. (2008) WHO Guidelines for Drinking-water Quality (incorporating the 1st and 2nd addenda., Recommendations,3rd ed., WHO, Geneva, 2008, p.1). *World Health Organization*.

World Health Organization. (2011) WHO Guidelines for Drinking-water Quality (4th ed., WHO Geneva, 2011, p. 340). *World Health Organization*.

Xu, Z., Liu, Y., Wang, R., Zhang, J., Cheng, J., Chen, S., and Zhang, D. (2020). AIEE based “turn-on” fluorescent sensor for Al^{3+} ions and induced tetraphenylethene self-assemblies. *Organic Electronics,* 85, 105820.

Yang, Y. K.; Yook, K. J.; Tae J. (2005). A Rhodamine-Based Fluorescent and Colorimetric Chemodosimeter for the Rapid Detection of Hg^{2+} Ions in Aqueous Media. *Journal Am. Chem. Soc*, 127, 16760-16761.

Yu, Y., Lin, L. R., Yang, K. B., Zhong, X., Huang, R. B., and Zheng, L. S. (2006). A fluorescent probe for rapid detection of low-concentration mercury ions and its application in biological cells. *Environmental Materials Chemistry and Physics*, 69, 103-106.

Yuan, Y., Chen, X., Chen, Q., Jiang, G., Wang, H., and Wang, J. (2019). New switch on fluorescent probe with AIE characteristics for selective and reversible detection of mercury ion in aqueous solution. *Analytical biochemistry*, 585, 113403.

Zhang, J., Xu, L., and Wong, W. (2018). Energy materials based on metal Schiff base complexes. *Coordination Chemistry Reviews,* 355, 180-198.

APPENDIX

Ap.1 NMR, Mass and FT-IR spectrums

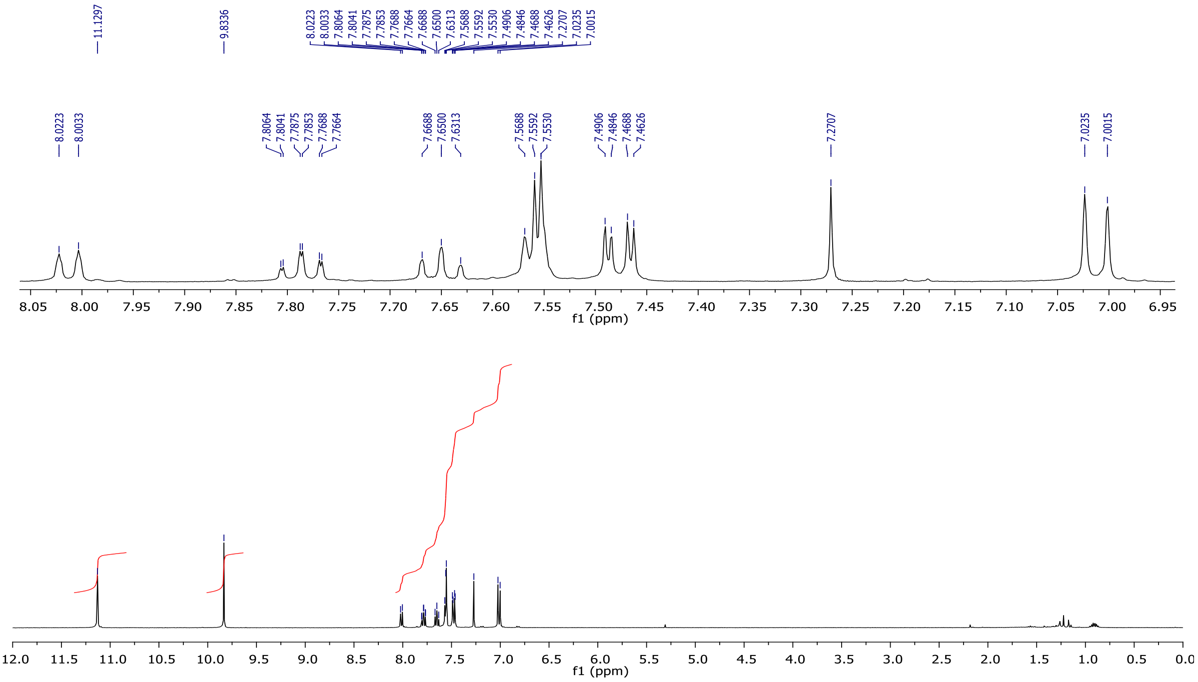

Appx. 1. The ^{1}H-NMR (400 MHz) spectrum of PP-CHO in $CDCl_3$

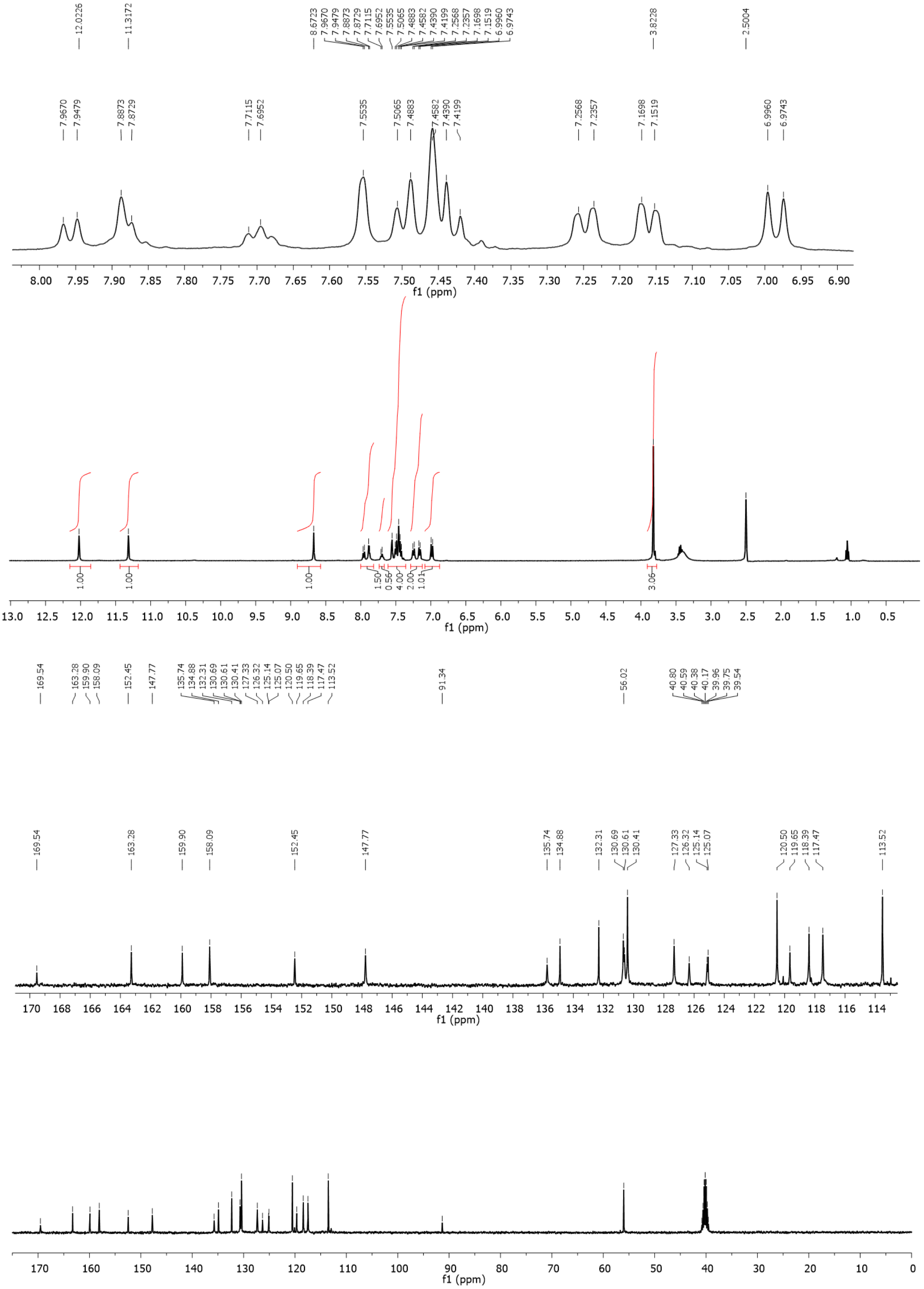

Appx. 2. The ^{1}H-NMR (400 MHz) and APT ^{13}C-NMR (100 MHz) spectrums of **PP-1** in DMSO-d6.

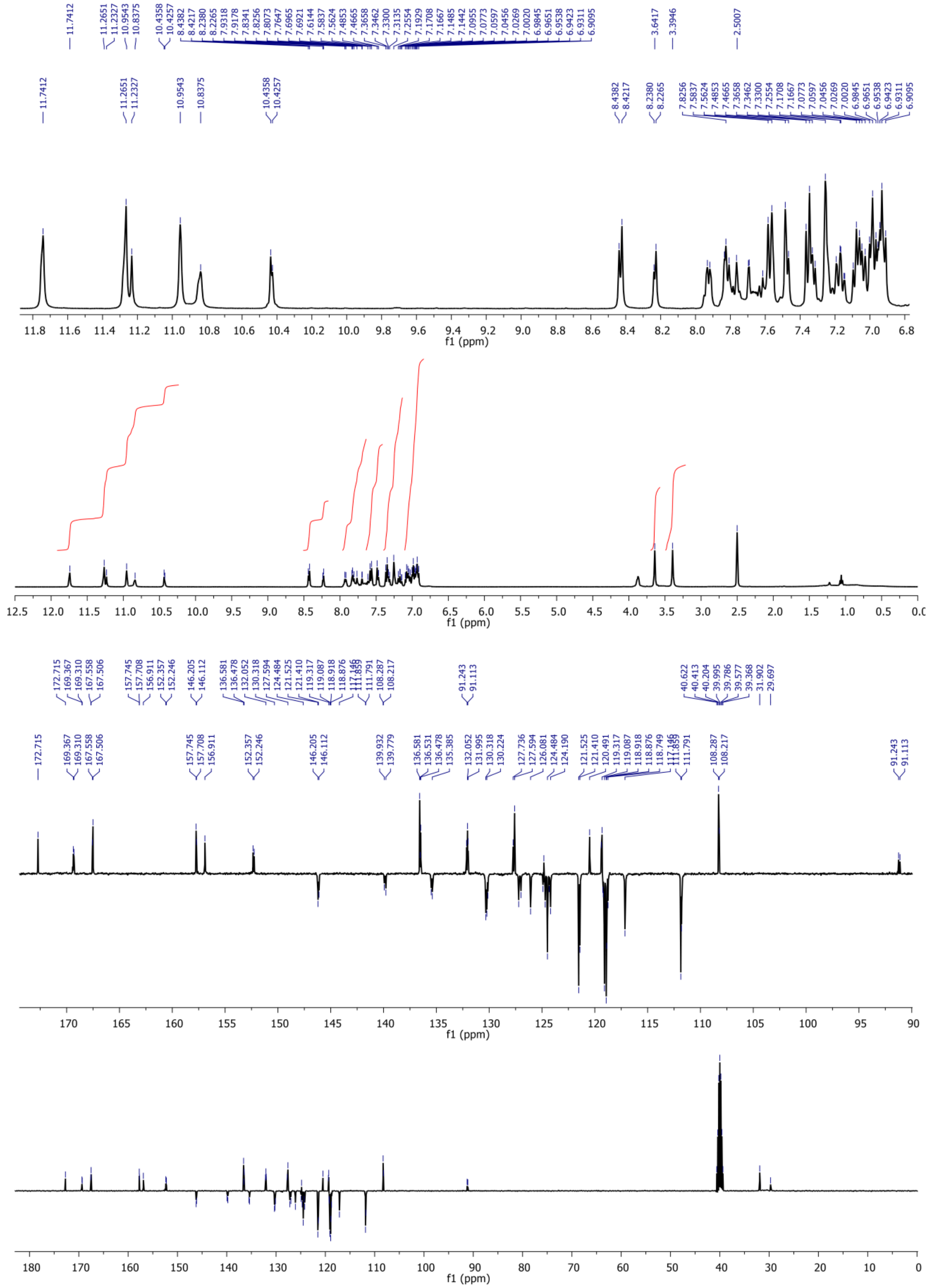

Appx. 3. The ^{1}H-NMR (400 MHz) and APT ^{13}C-NMR (100 MHz) spectrums of **PP-2** in DMSO-d6.

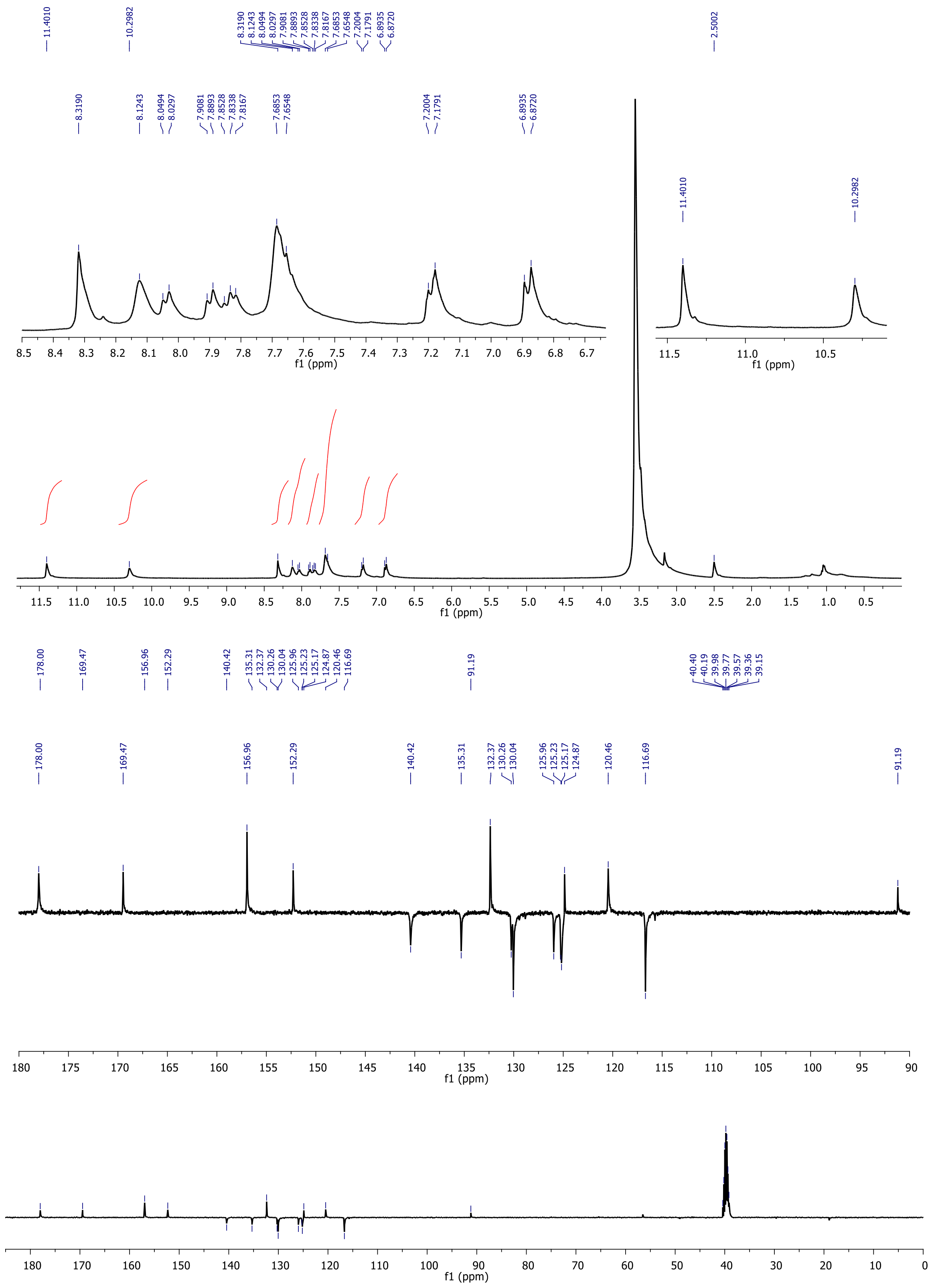

Appx. 4. The ^{1}H-NMR (400 MHz) and APT ^{13}C-NMR (100 MHz) spectrums of **PP-3** in DMSO-d6.

(A)

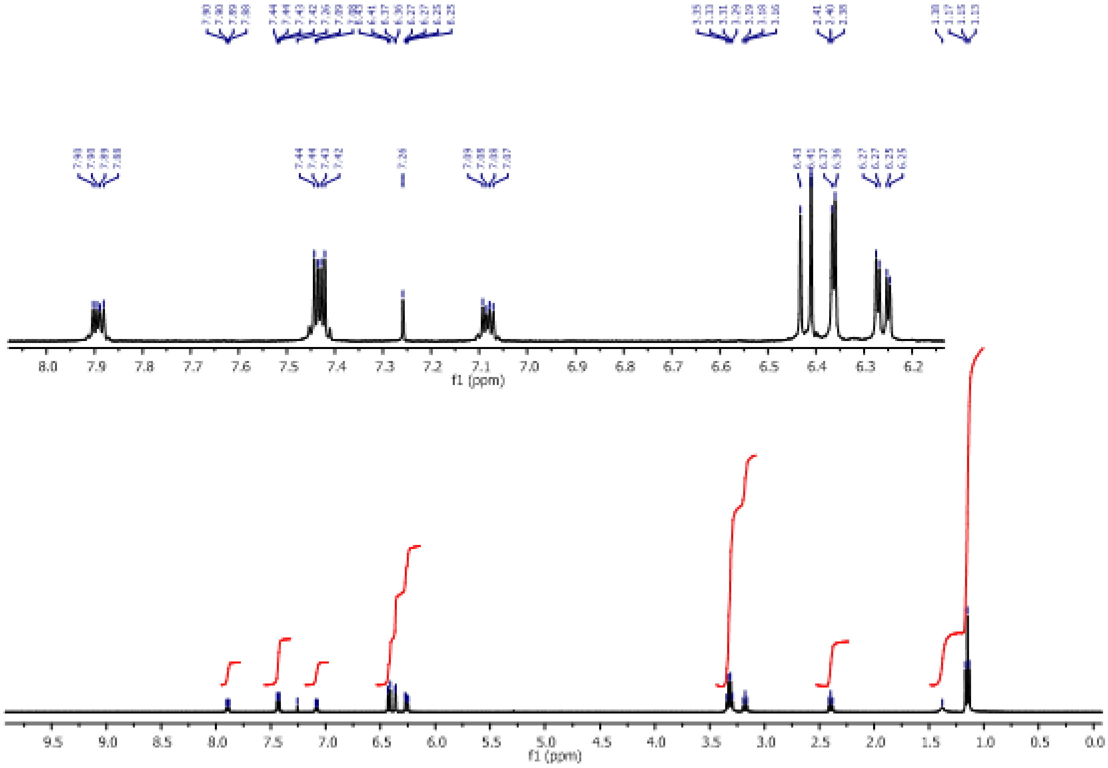

Appx. 5. The ^{1}H-NMR (400 MHz) spectrum of **Rh-NH$_2$** in CDCl$_3$.

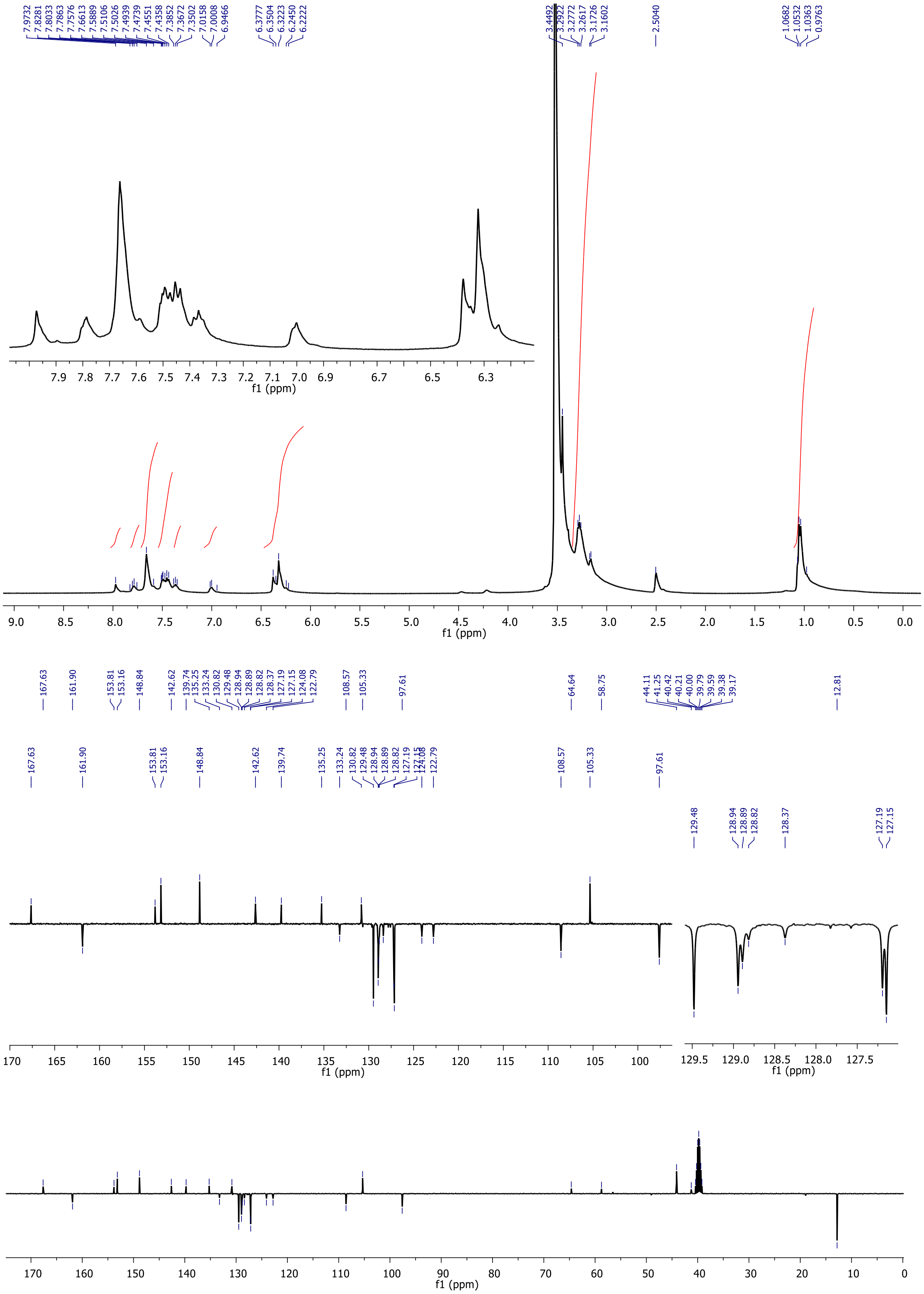

Appx. 6. The ^{1}H-NMR (400 MHz) and APT ^{13}C-NMR (100 MHz) spectrums of **Rh-1** in DMSO-d6.

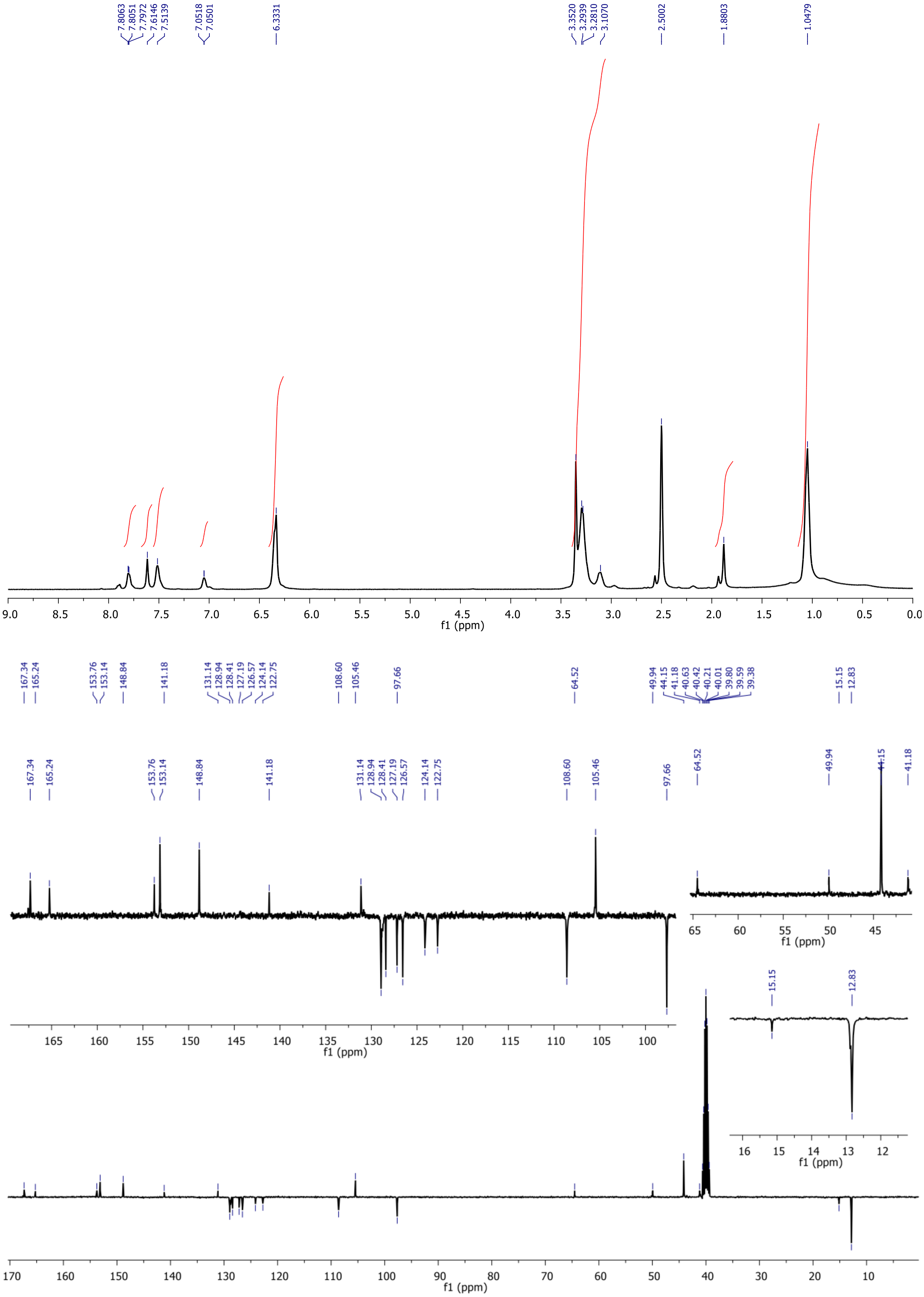

Appx. 7. The ^{1}H-NMR (400 MHz) and APT ^{13}C-NMR (100 MHz) spectrums of **Rh-2** in DMSO-d6.

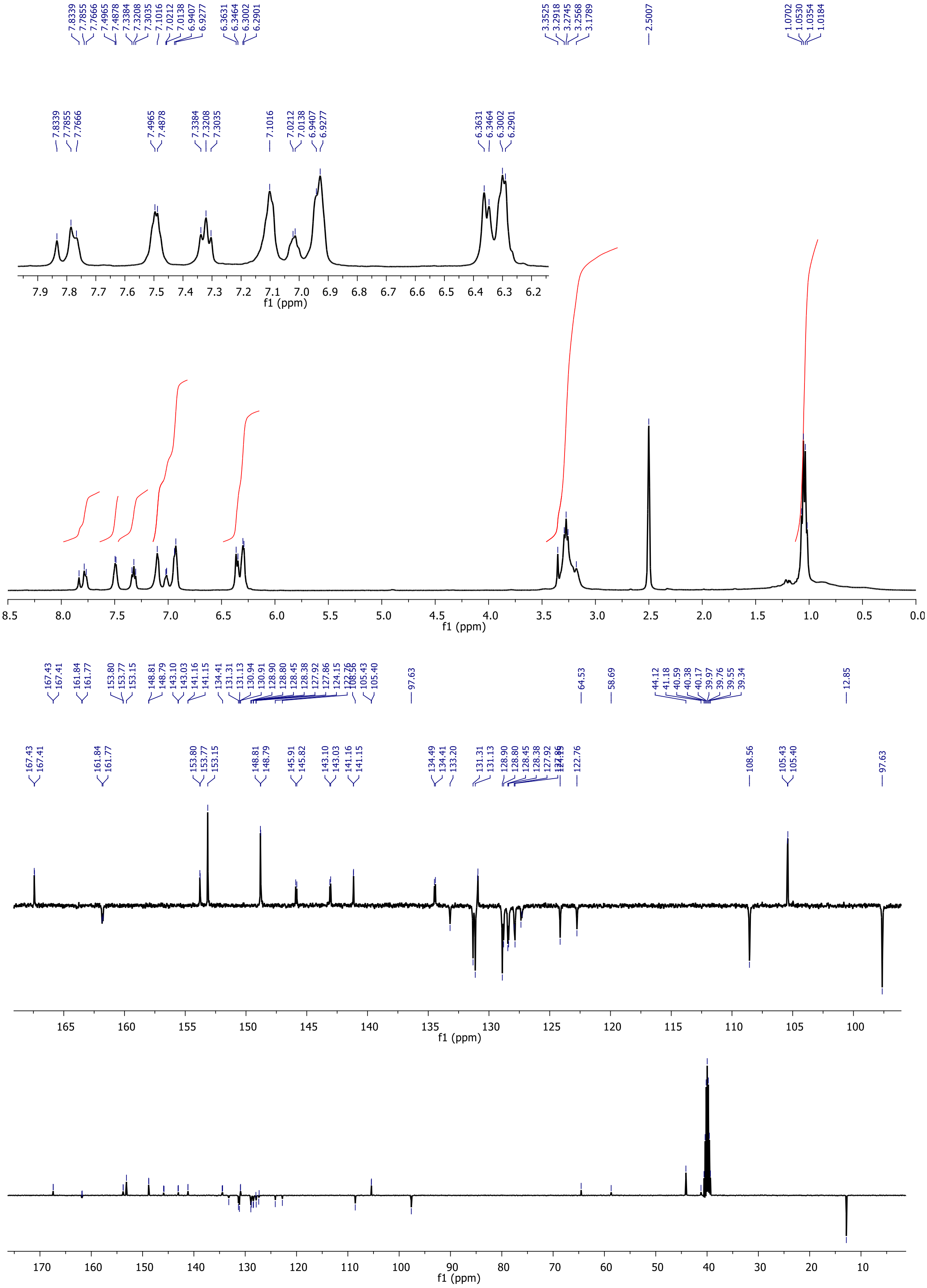

Appx. 8. The ^{1}H-NMR (400 MHz) and APT ^{13}C-NMR (100 MHz) spectrums of **Rh-3** in DMSO-d6.

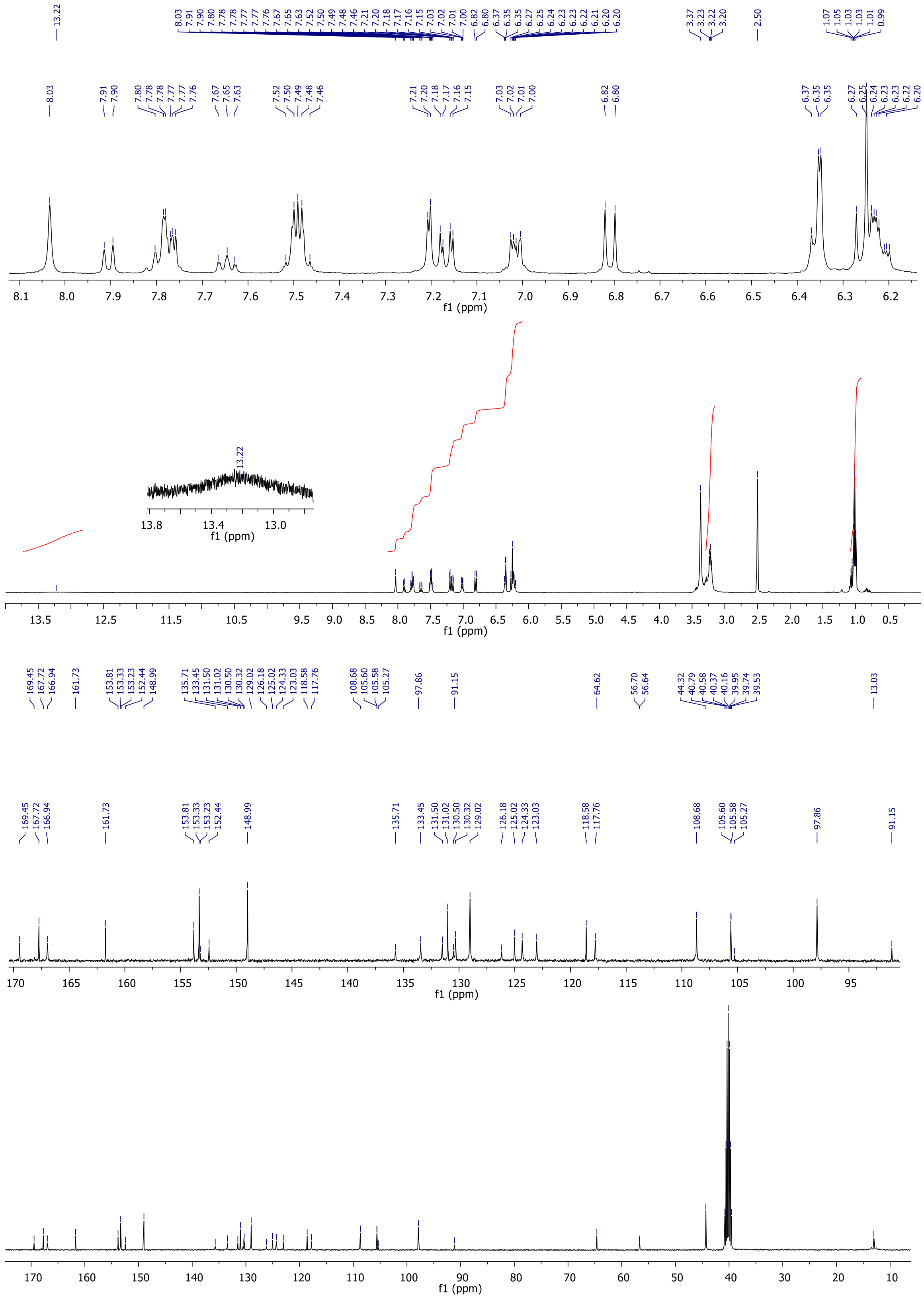

Appx. 9. The ^{1}H-NMR (400 MHz) and ^{13}C-NMR (100 MHz) spectrums of **Rh-PP-Rh** in DMSO-d6.

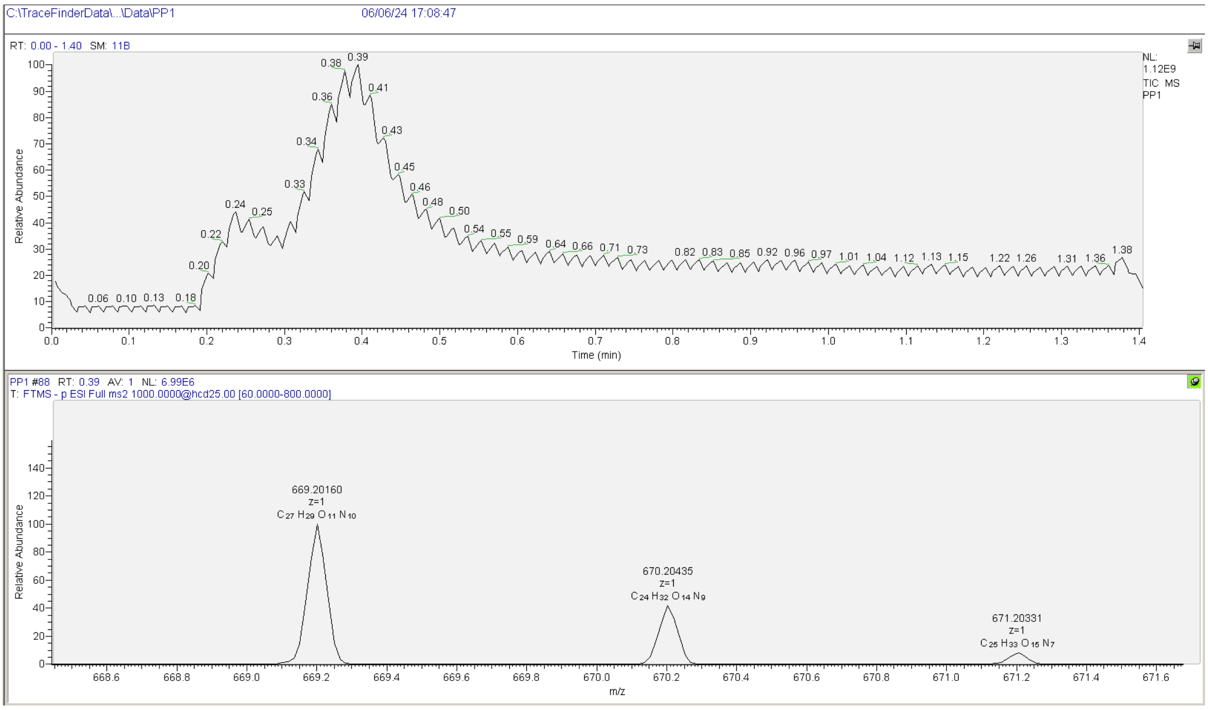

m/z	Intensity	Relative	Charge	Composition
669.20160	6997136.5	100.00	1.00	$C_{38}H_{29}O_8N_4$
670.20435	2937097.5	41.98	1.00	$C_{38}H_{30}O_8N_4$
671.20331	568209.0	8.12	1.00	$C_{38}H_{31}O_8N_4$

Appx. 10A. The HRMS (ESI-TOF) spectrums of PP-1

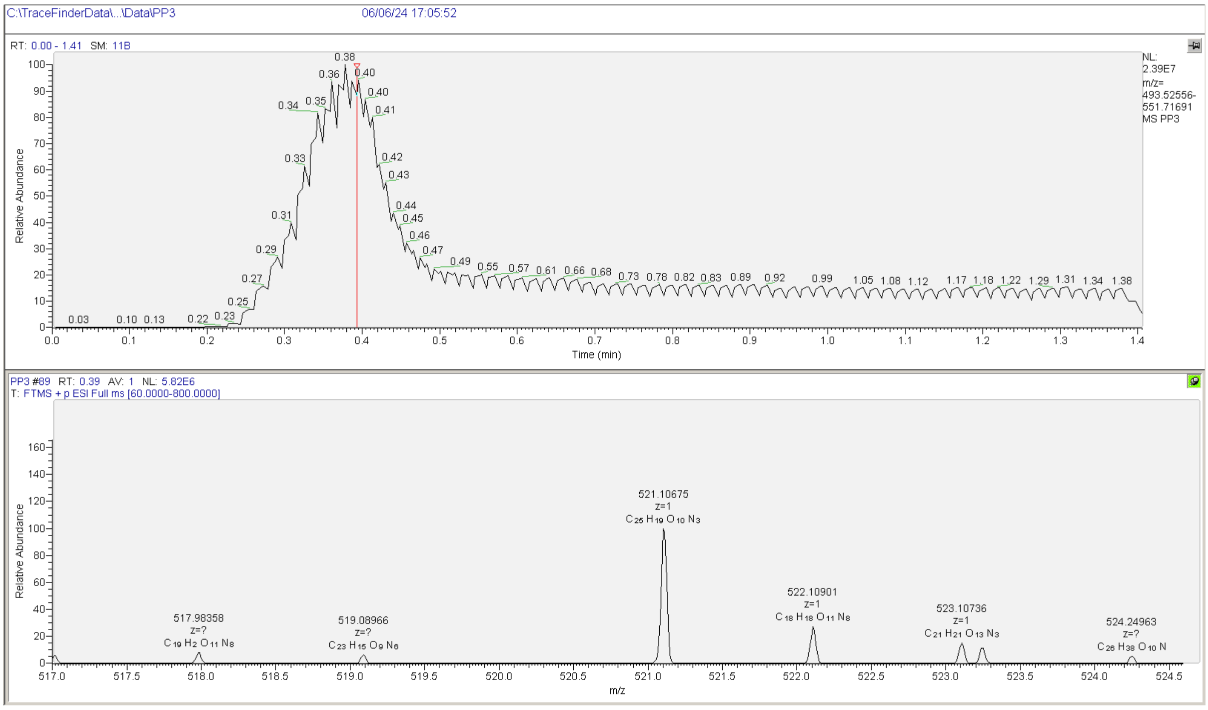

m/z	Intensity	Relative	Charge	Composition
517.01678	348040.4	5.66	1.00	C24 H19 O4 S2 N6
517.98358	498177.0	8.11	0.00	C24 H19 O4 S2 N6
519.08966	371328.3	6.04	0.00	C24 H19 O4 S2 N6
521.10675	6145291.5	100.00	1.00	C24 H21 O4 S2 N6
522.10901	1625230.5	26.45	1.00	C24 H22 O4 S2 N6
523.10736	884710.8	14.40	1.00	C24 H23 O4 S2 N6
523.24561	714138.6	11.62	0.00	C24 H23 O4 S2 N6
524.24963	297725.6	4.84	0.00	C24 H24 O4 S2 N6

Appx. 10B. The HRMS (ESI-TOF) spectrums of PP-2.

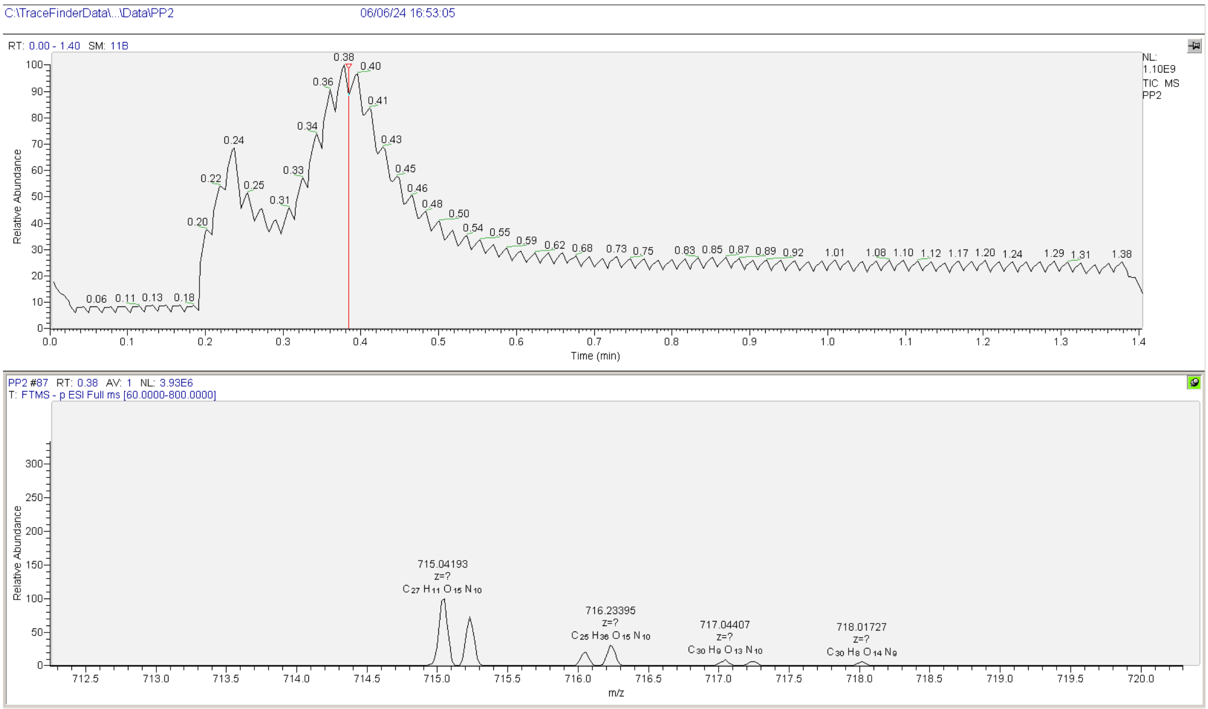

m/z	Intensity	Relative	Charge	Composition
715.04193	4137025.0	100.00	0.00	C42 H30 O6 N6
715.23145	2870115.0	69.38	0.00	C42 H30 O6 N6
716.04761	822367.9	19.88	0.00	C42 H31 O6 N6
716.23395	1264147.9	30.56	0.00	C42 H31 O6 N6

Appx. 10C. The HRMS (ESI-TOF) spectrums of PP-3.

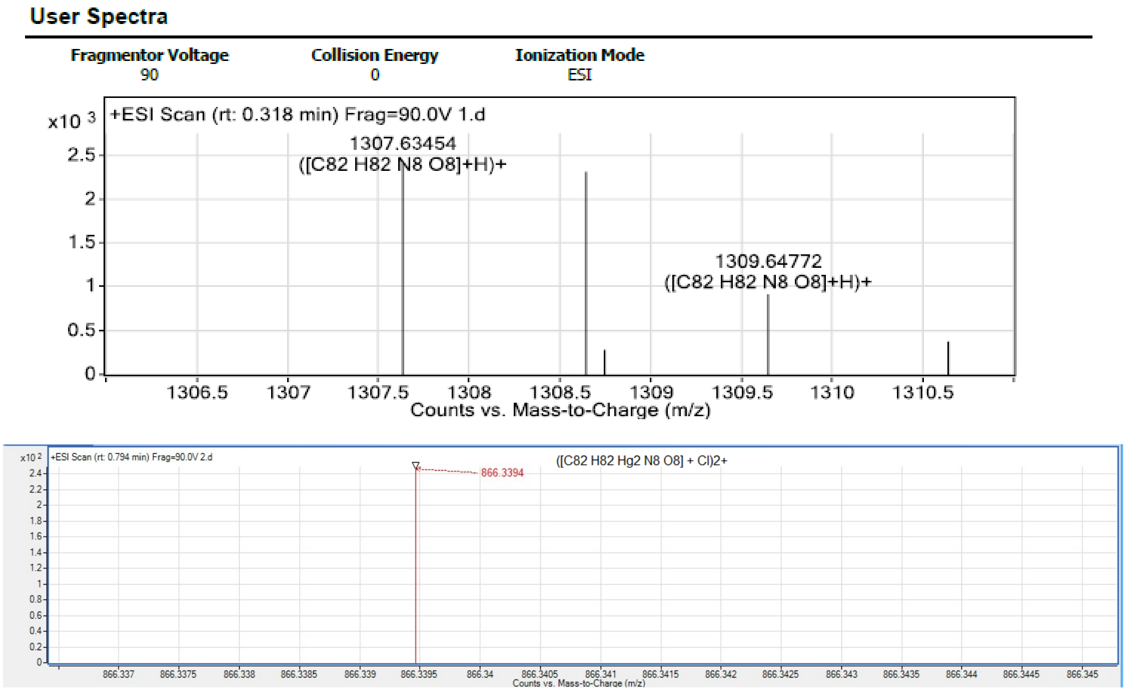

User Spectra

Fragmentor Voltage 90

Collision Energy 0

Ionization Mode ESI

Appx. 10D. The HRMS (ESI-TOF) spectrums of Rh-1 and Rh-1$(Hg)_2$

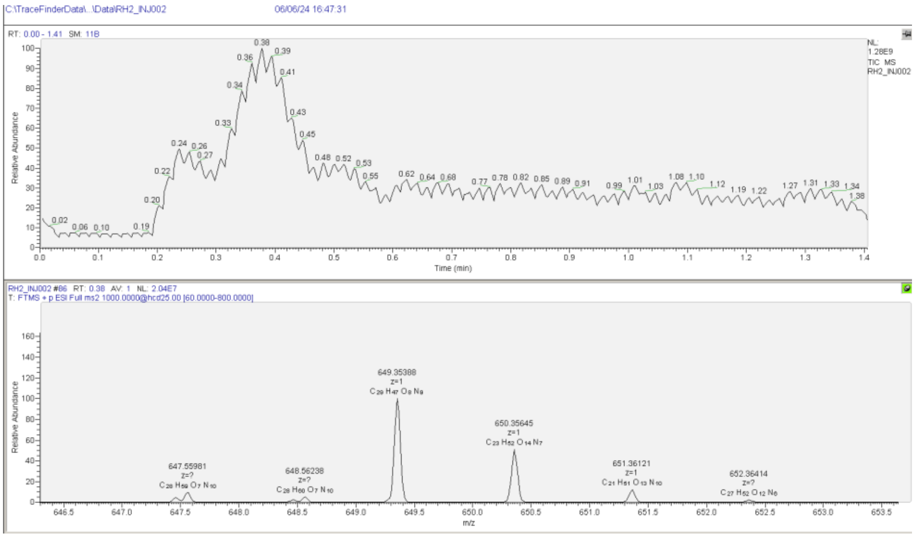

m/z	Intensity	Relative	Charge	Composition
647.45795	923962.6	4.47	0.00	C43 H43 O2 N4
647.55981	2034540.3	9.85	0.00	C43 H43 O2 N4
648.46393	540071.7	2.61	0.00	C43 H43 O2 N4
648.56238	1035098.4	5.01	0.00	C43 H43 O2 N4
649.35388	20663066.0	100.00	1.00	C43 H44 O2 N4
650.35645	10449123.0	50.57	1.00	C43 H445 O2 N4
651.36121	2484167.0	12.02	1.00	C43 H46 O2 N4
652.36414	467322.1	2.26	0.00	C43 H47 O2 N4

Appx. 10E. The HRMS (ESI-TOF) spectrums of Rh-2.

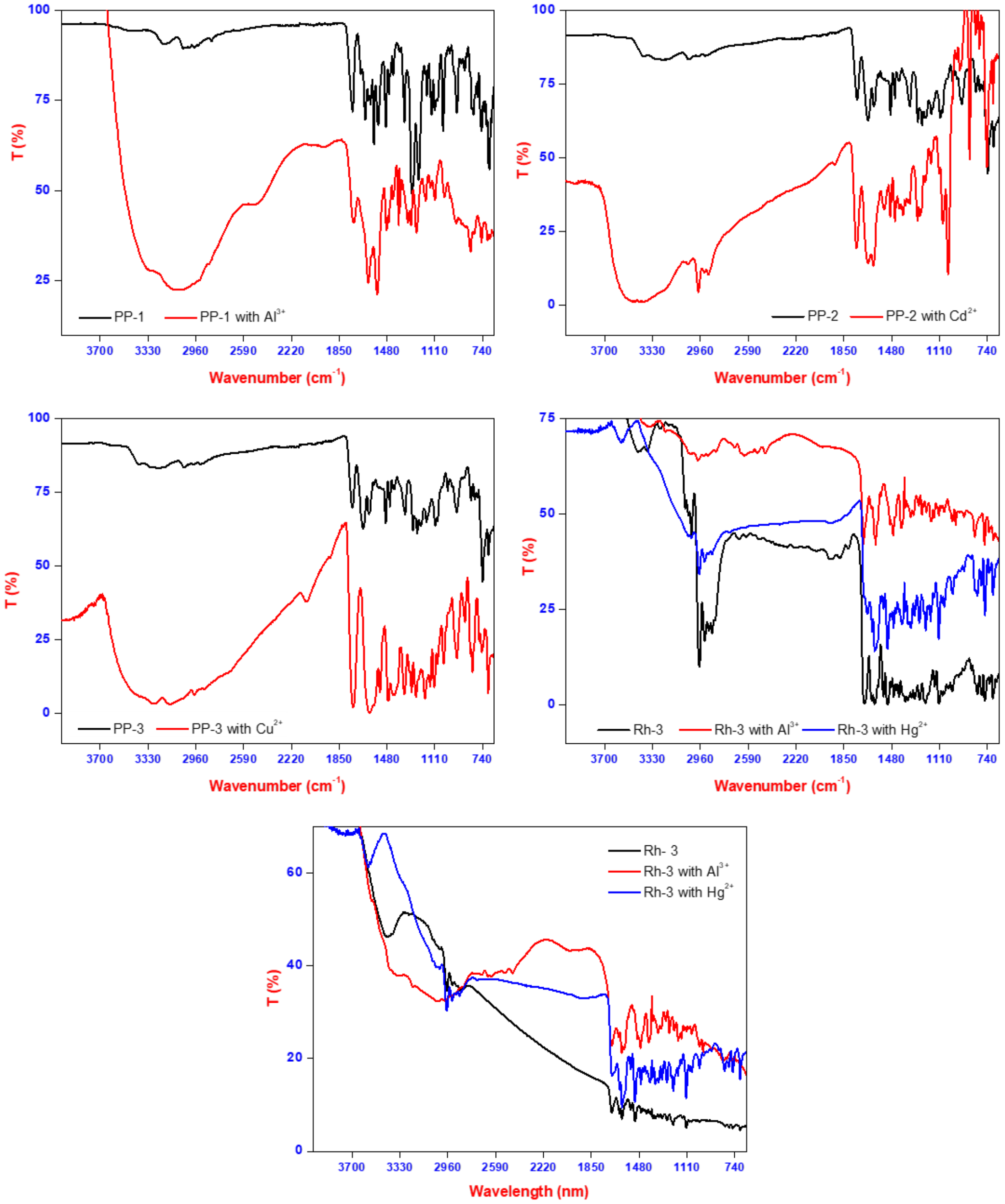

Appx. 11. FT-IR spectras of probes with metals

Ap.2 UV-Vis and Fluorescence spectrums

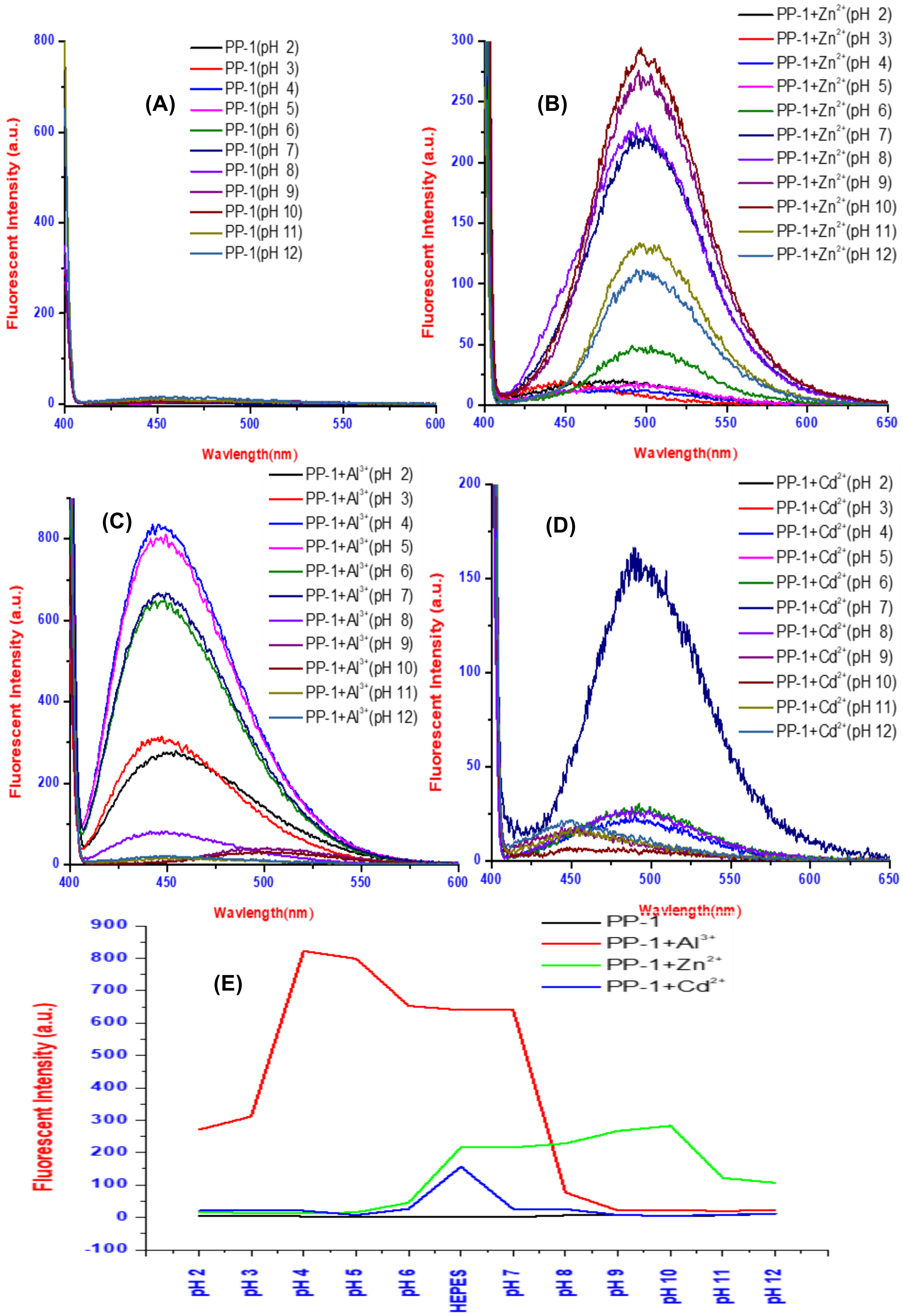

Appx. 12. The fluorescence spectra of PP-1 (**A**) PP-1+Al^{3+} (**B**), PP-1+Zn^{2+} (**C**) and PP-1+Cd^{2+} (**D**) at different pH (3–12) in EtOH: H2O, the pH was modulated by adding HCl or NaOH solution.

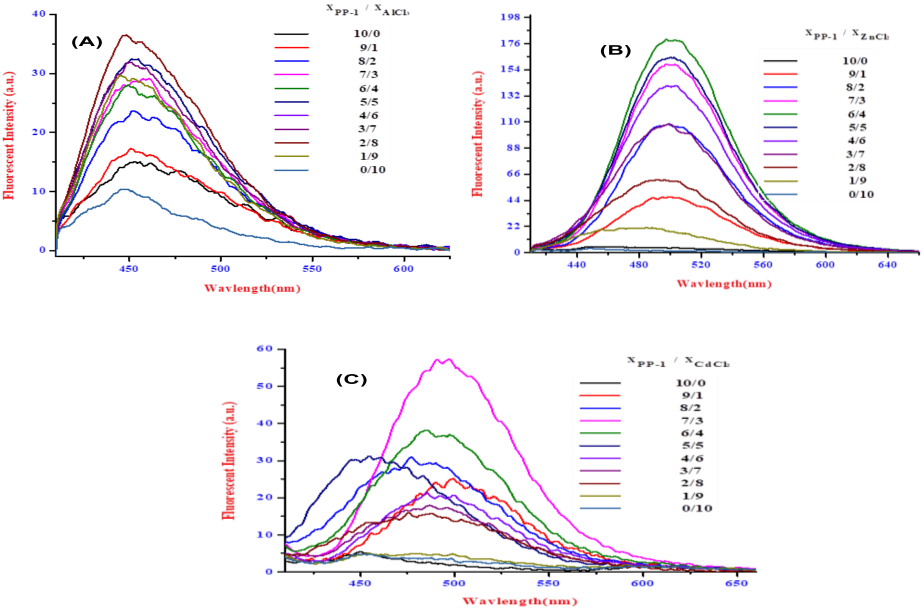

Appx. 13. The Job's plot absorbance spectra of PP-1+Al^{3+} (**A**), PP-1+Zn^{2+} (**B**) and PP-1+Cd^{2+} (**C**) in EtOH/H_2O (v/v:1/1)

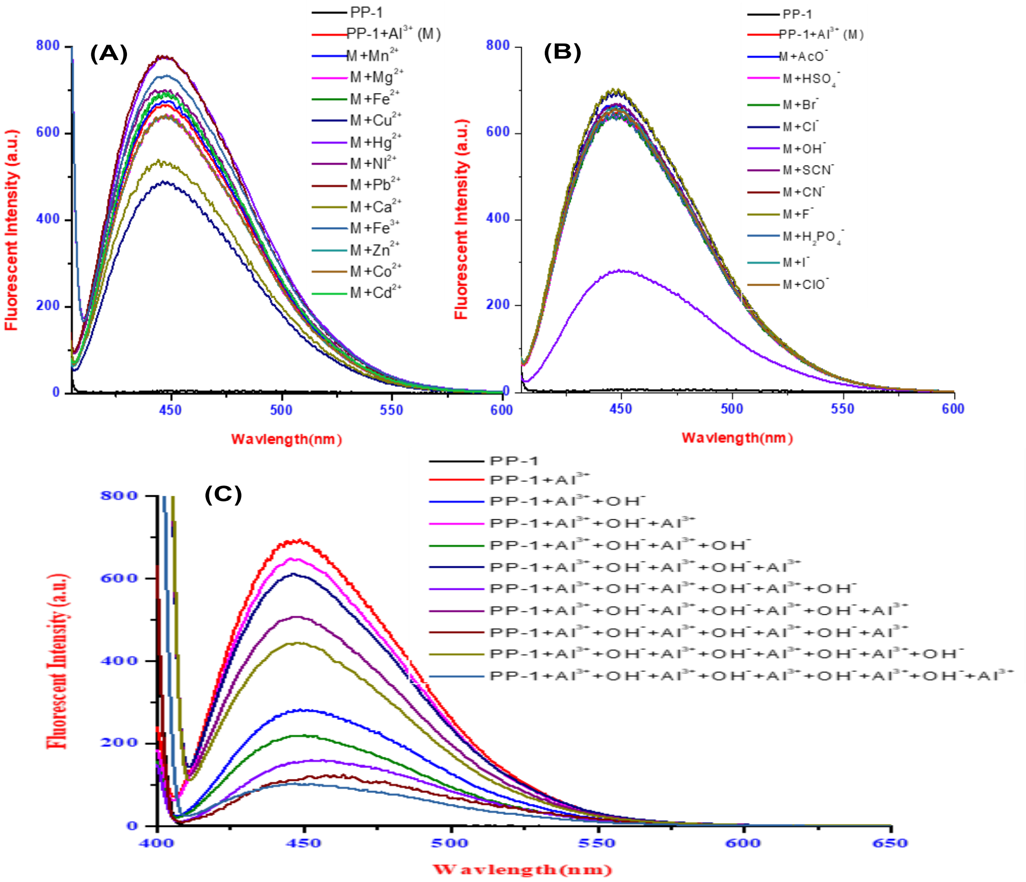

Appx. 14. Fluorescence spectra of PP-1 in the presence of Al^{3+} upon the addition of different ions in EtOH/H_2O (v/v:1/1) (**A**) or (**B**). Reversible switching of the fluorescence spectrum of PP-1upon alternate addition of Al^{3+} and OH^- (**C**).

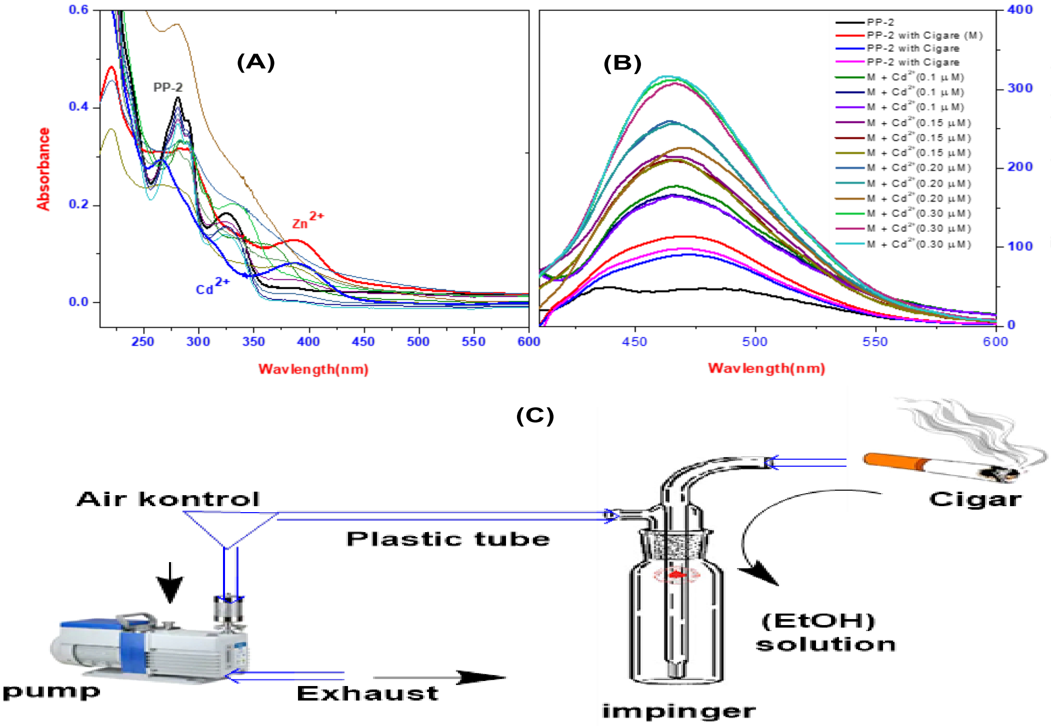

Appx. 15. The UV-Vis (**A**) spectrums of PP-2 in the absence and presence of metal ions in EtOH/H_2O (v/v: 1/1), The fluorescence intensity of PP-2 (**B**) the smoke was collected in a EtOH/H_2O (v/v:9/1) solution in a of the cigarette smoke extract with **PP-2** was then measured upon the addition of Cd^{2+} ions, and (**C**) low-pressure setup.

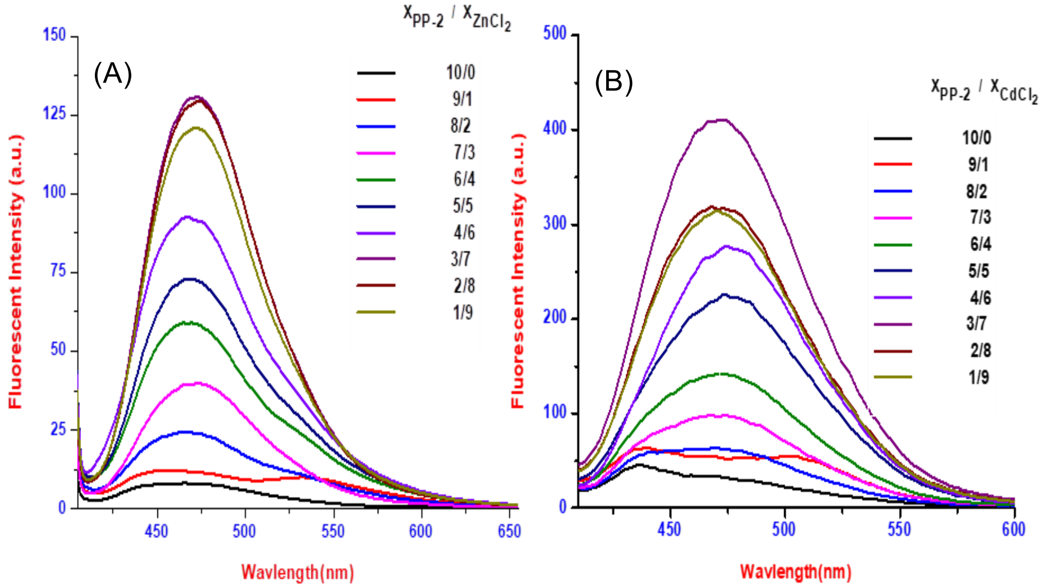

Appx. 16. The Job's plot fluorescence spectra of PP-2 with Zn^{2+} (in EtOH/H_2O v/v: 1/1) and Cd^{2+} (in EtOH/H_2O, v/v:9/1)

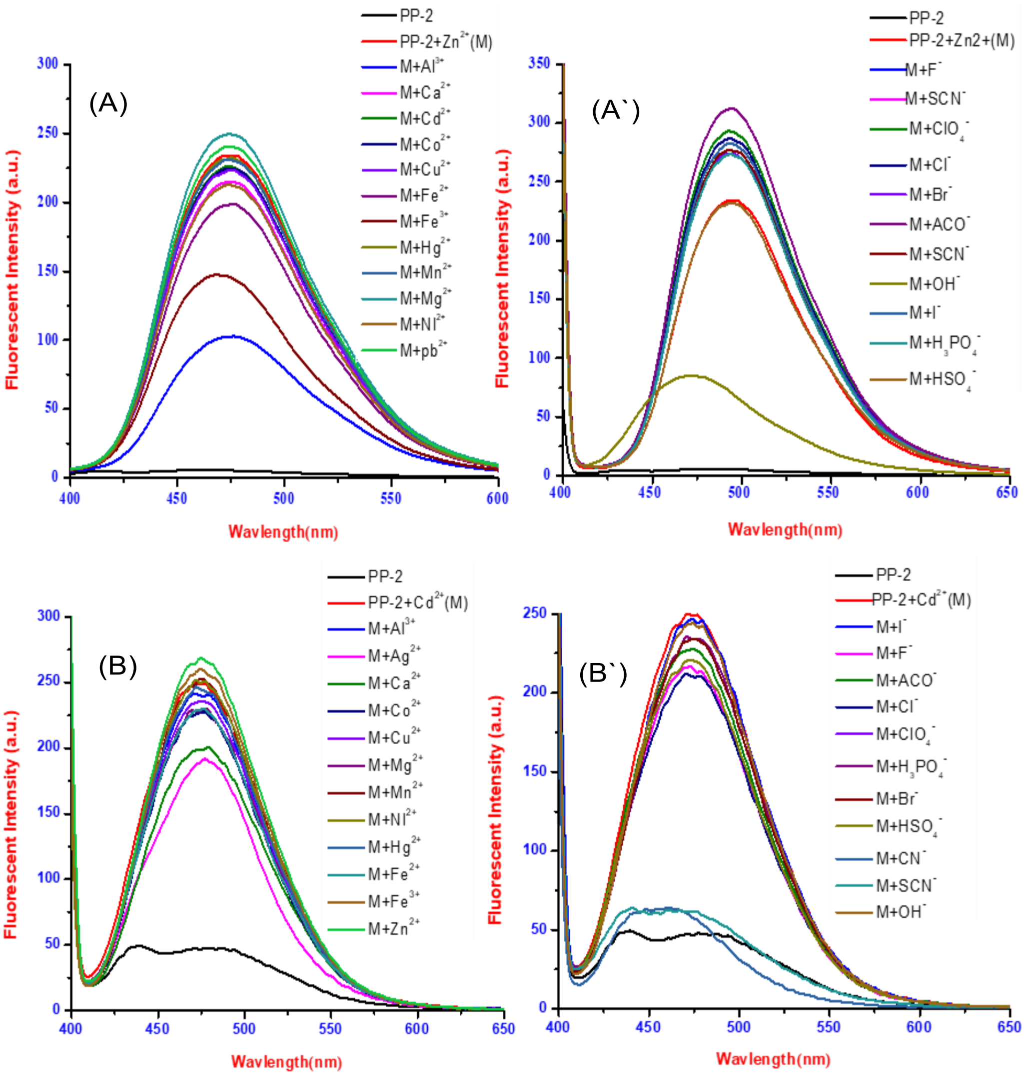

Appx. 16. Fluorescence spectra of PP-2 in the presence of Zn^{2+} upon the addition of different ions in EtOH/H_2O (v/v:1/1) (**A**), (**A`**). and in the presence of $Cd^{2+}$ upon the addition of different ions in EtOH/$H_2O$ (v/v:9/1) (**B**), (**B`**).

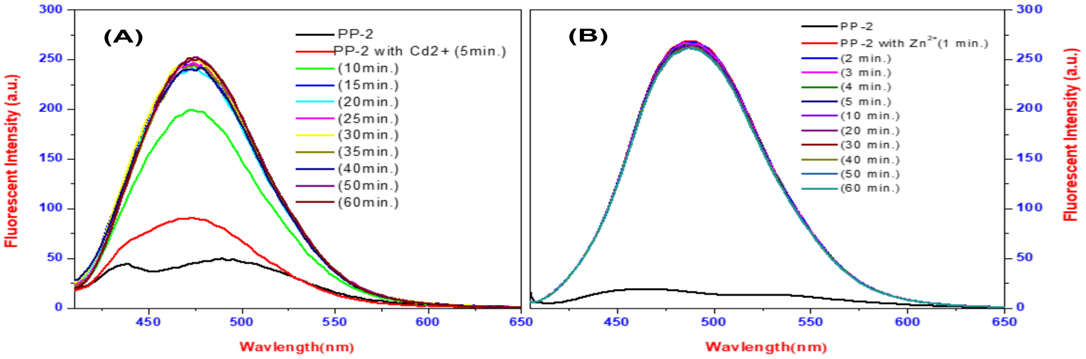

Appx. 17. The fluorescence enhances the profile of the addition of Cd^{2+} and Zn^{2+} to PP-2 in EtOH/H_2O from 0 min. to 60 min. (**A**) and (**B**).

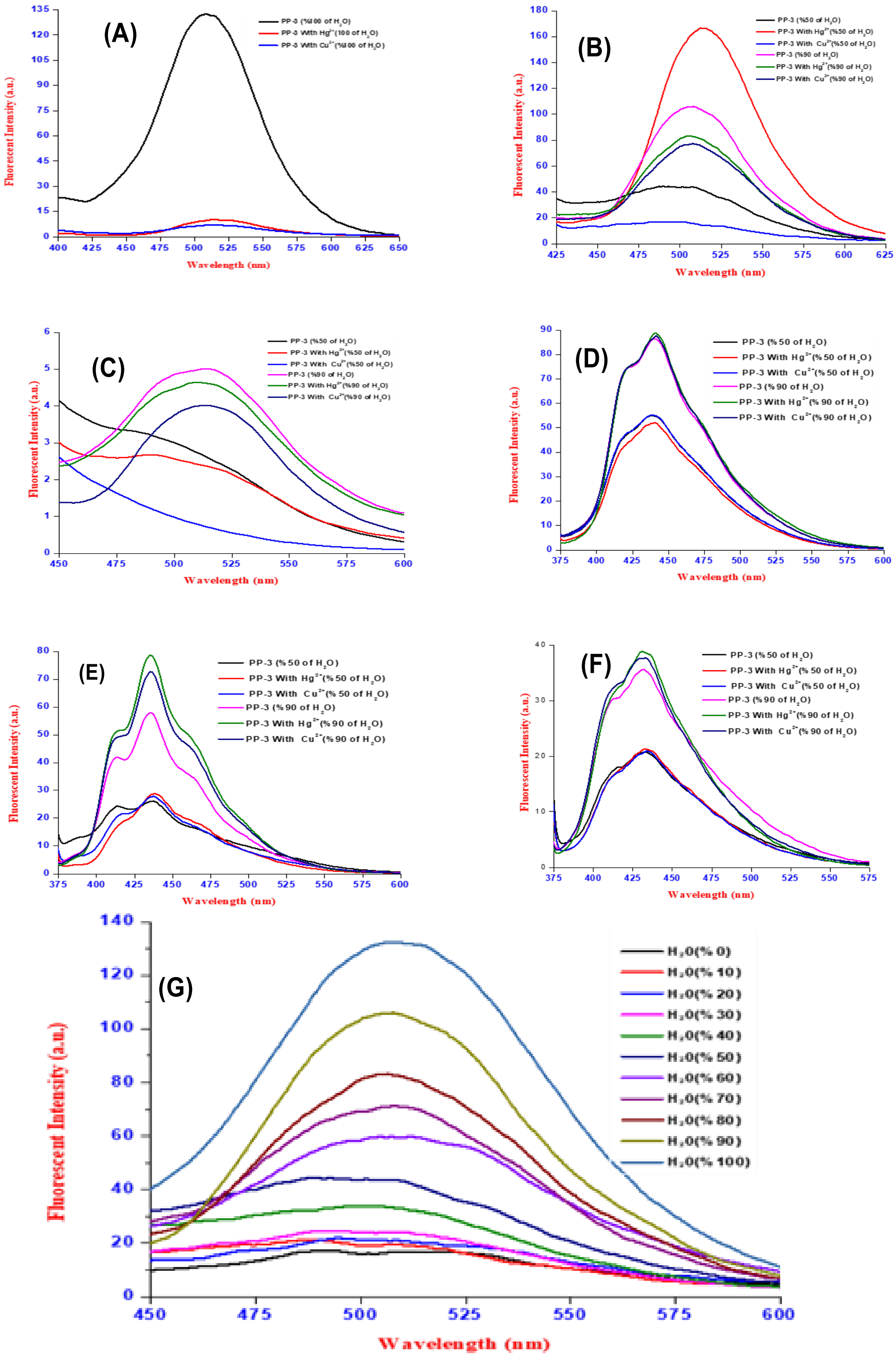

Appx. 18. Fluorescence spectra of PP-3 in a deffrint variety of solvent systems, and fluorescence spectra PP-3 - Hg^{2+} and PP-3 -Cu^{2+} in H2O (**A**), EtOH (**B**), MetOH (**C**), CH_3CN (**D**), THF(**E**) and DMSO (**F**). Fluorescence spectra of PP-3 in EtOH variety H_2O ratios(G).

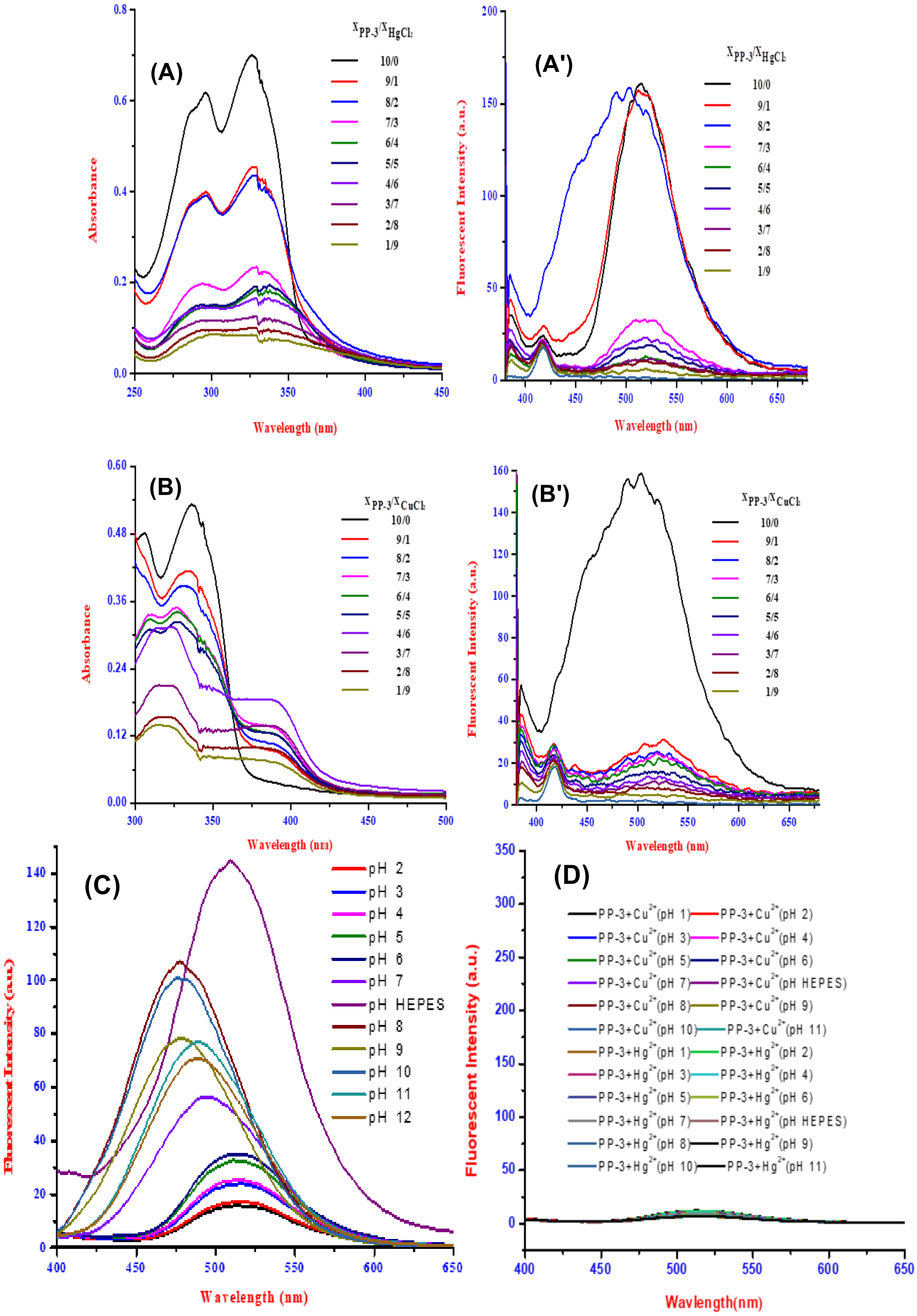

Appx. 19. The Job's plot UV-Vis (**A, B**) spectrums and fluorescence spectra (**A`, B`**) of PP-3 with Hg^{2+} and Cu^{2+} (H_2O). The fluorescence spectra of PP-3 (**C**), PP-3+Cu^{2+}, and PP-1+Zn^{2+} (**D**) at different pH (3–12) in (H_2O), the pH was modulated by adding HCl or NaOH solution

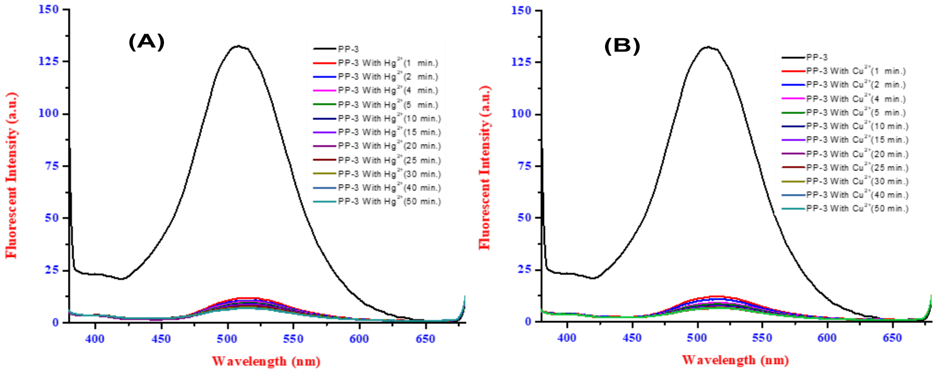

Appx. 20. The fluorescence enhances the profile of the addition of Hg^{2+} and Cu^{2+} to PP-3 in H_2O from 0 min. to 60 min. (**A**) and (**B**).

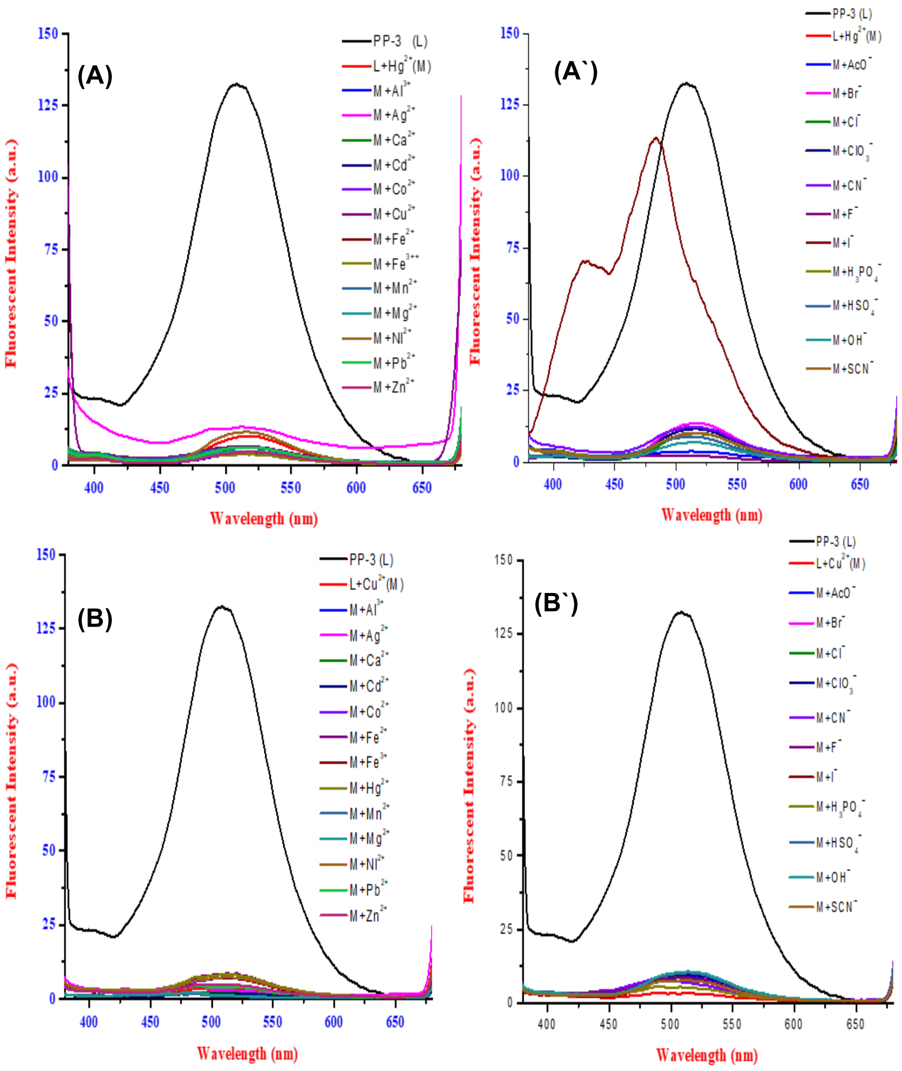

Appx. 21. Fluorescence spectra of PP-3 in the presence of Hg^{2+} and Cu^{2+} upon the addition of different ions in H_2O (**A**), (**A`**) and (**B**), (**B`**).

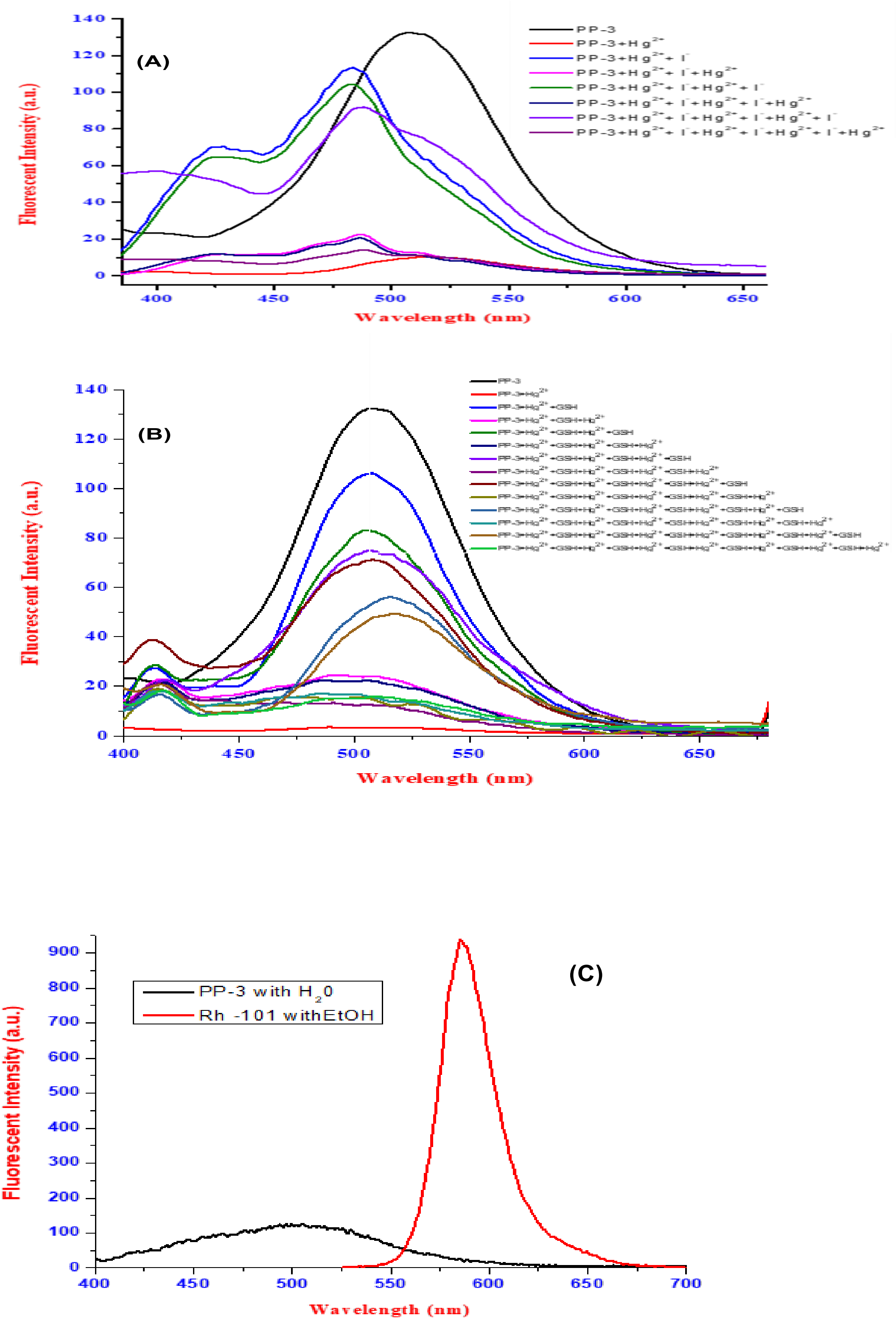

Appx. 22. Fluorescence spectra of PP-3 in the presence of reversible switching of the fluorescence spectrum of PP-3 upon alternate addition of Hg^{2+} or I^{-} (**A**) and Cu^{2+} or GSH(**B**) in H_2O. (**C**) Fluorescence spectra of PP-3 in the H_2O or Rh-101 in the eEtOH.

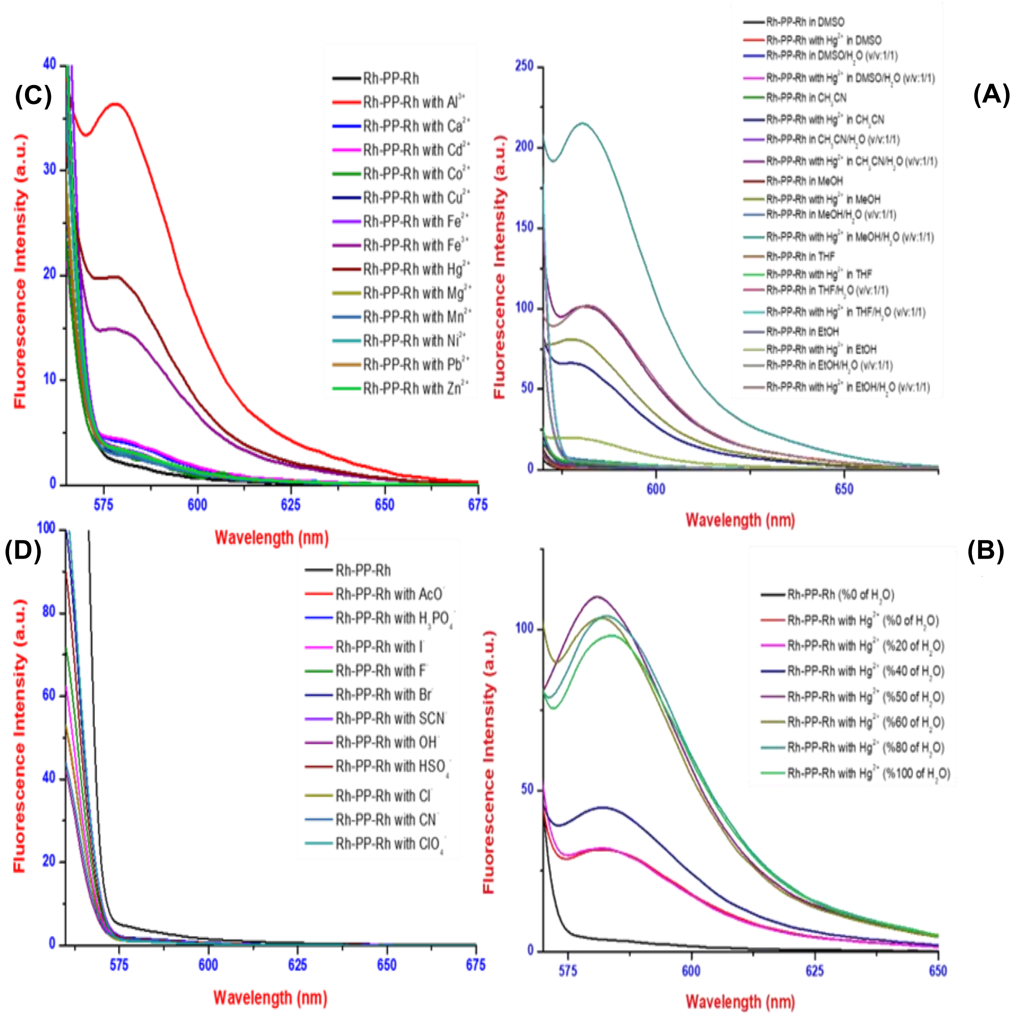

Appx. 23. Fluorescence spectras of (**A**) Rh-PP-Rh / Rh-PP-Rh-Hg^{2+} in variety solvent systems, and (**B**) Rh-PP-Rh-$Hg^{2+}$and Fluorescence spectra of (**C**) Rh-PP-Rh in the presence different metal ions in EtOH, and (**D**) Rh-PP-Rh in the absence and presence of anions in EtOH/H_2O (v/v: 1/1, with HEPES)

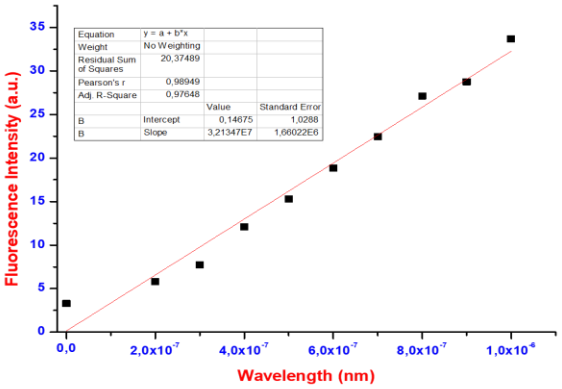

Equation	y = a + b*x		
Weight	No Weighting		
Residual Sum of Squares	20,37489		
Pearson's r	0,98949		
Adj. R-Square	0,97648		
		Value	Standard Error
B	Intercept	0,14675	1,0288
B	Slope	3,21347E7	1,66022E6

Appx. 24. The change fluorescence intensity of the **Rh-PP-Rh** with the increasing concentration of Hg^{2+} (from 0 μM to 1 μM).

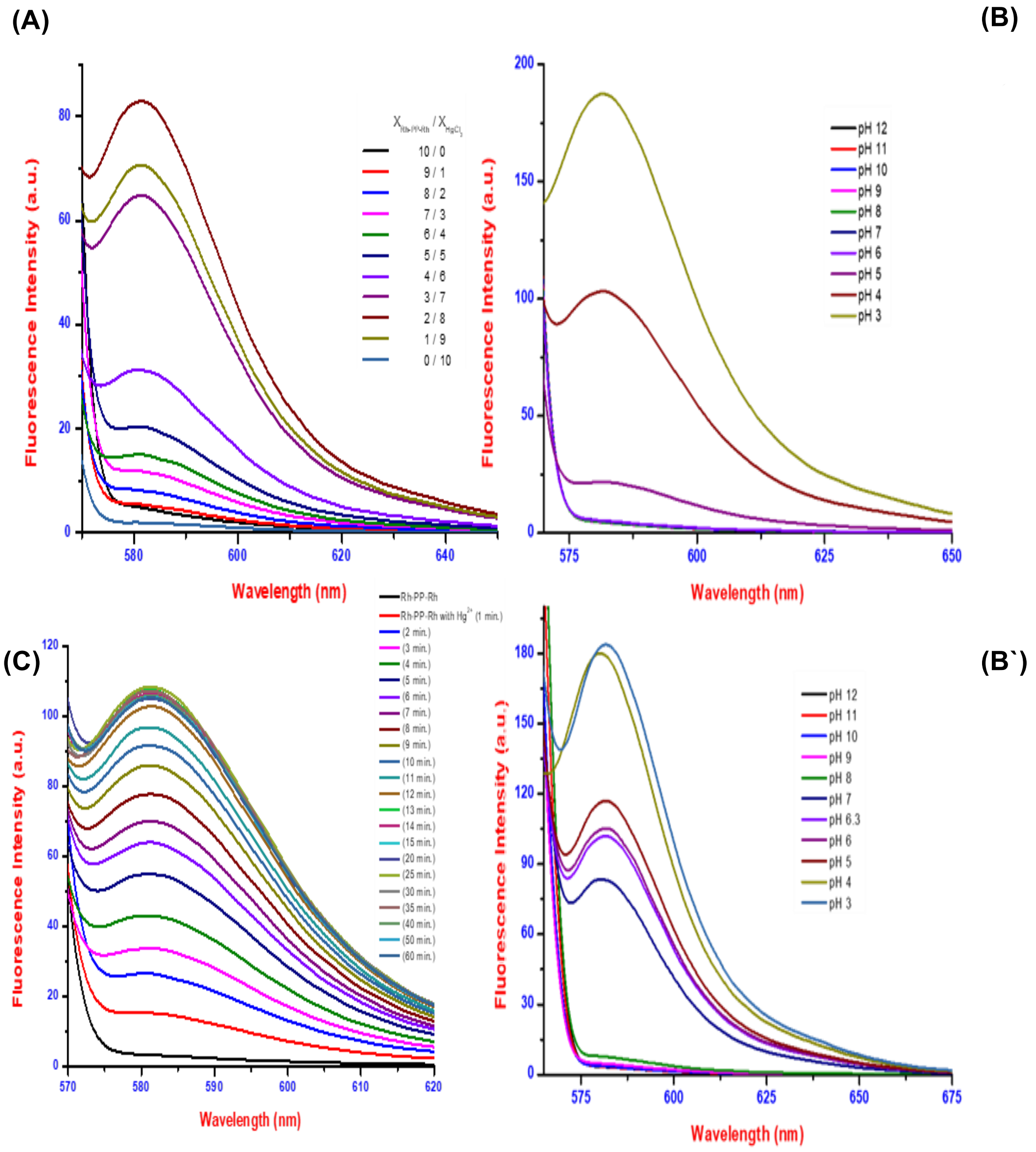

Appx. 25. The Job's plot absorbance spectra of Rh-PP-Rh with Hg^{2+} in EtOH/H_2O (v/v:1/1) (**A**). The fluorescence spectra of Rh-PP-Rh (**B**) and Rh-PP-Rh-Hg^{2+} (**B`**) at different pH (3–12) in H_2O, the pH was modulated by adding HCl or NaOH solution. The addition of Hg^{2+} to Rh-PP-Rh in EtOH/H_2O from 0 min. to 60 min(**C**).

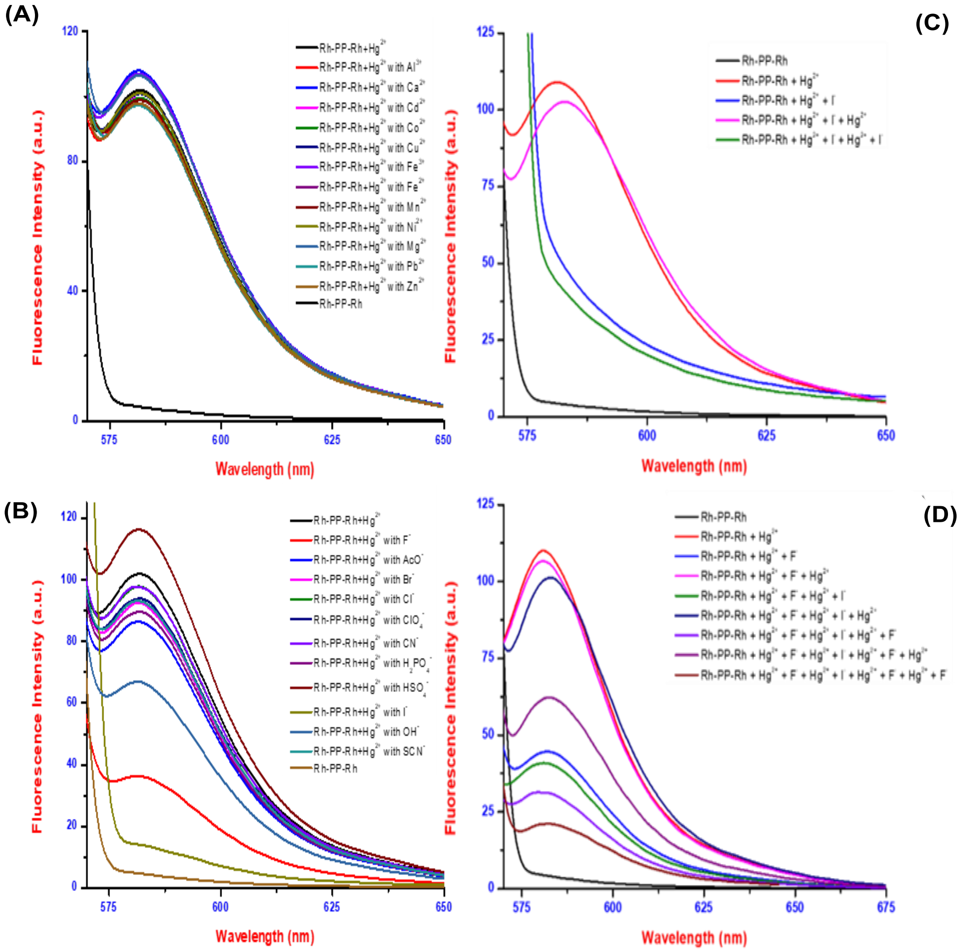

Appx. 26. Fluorescence spectra of Rh-PP-Rh in the presence of Hg^{2+} upon the addition of different ions in EtOH/H_2O (v/v:1/1) (**A**, **B**). Reversible switching of the fluorescence spectrum of Rh-PP-Rh upon alternate addition of Hg^{2+} and I^{-} (**C**) or F^{-} (**D**).

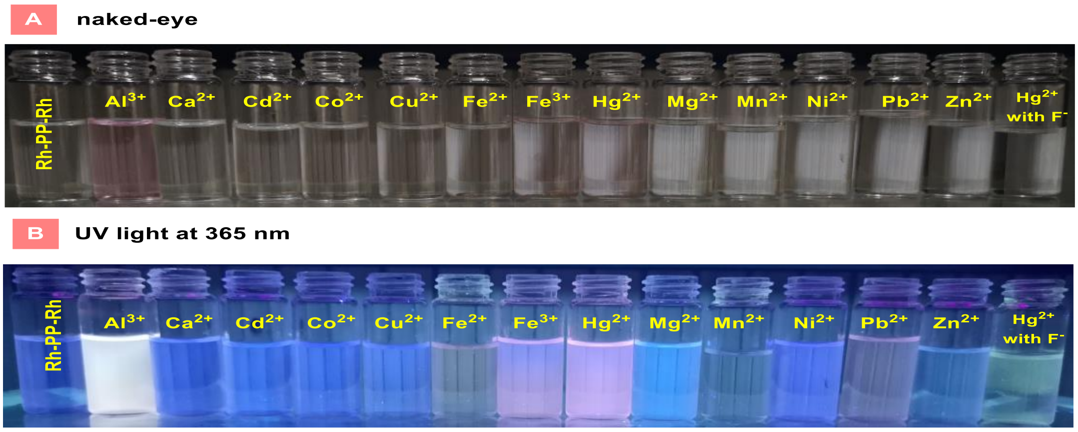

Appx. 27. The naked-eye (**A**) and UV light at 365 nm (**B**) color changes of Rh-PP-Rh in the presence of metal ions in EtOH

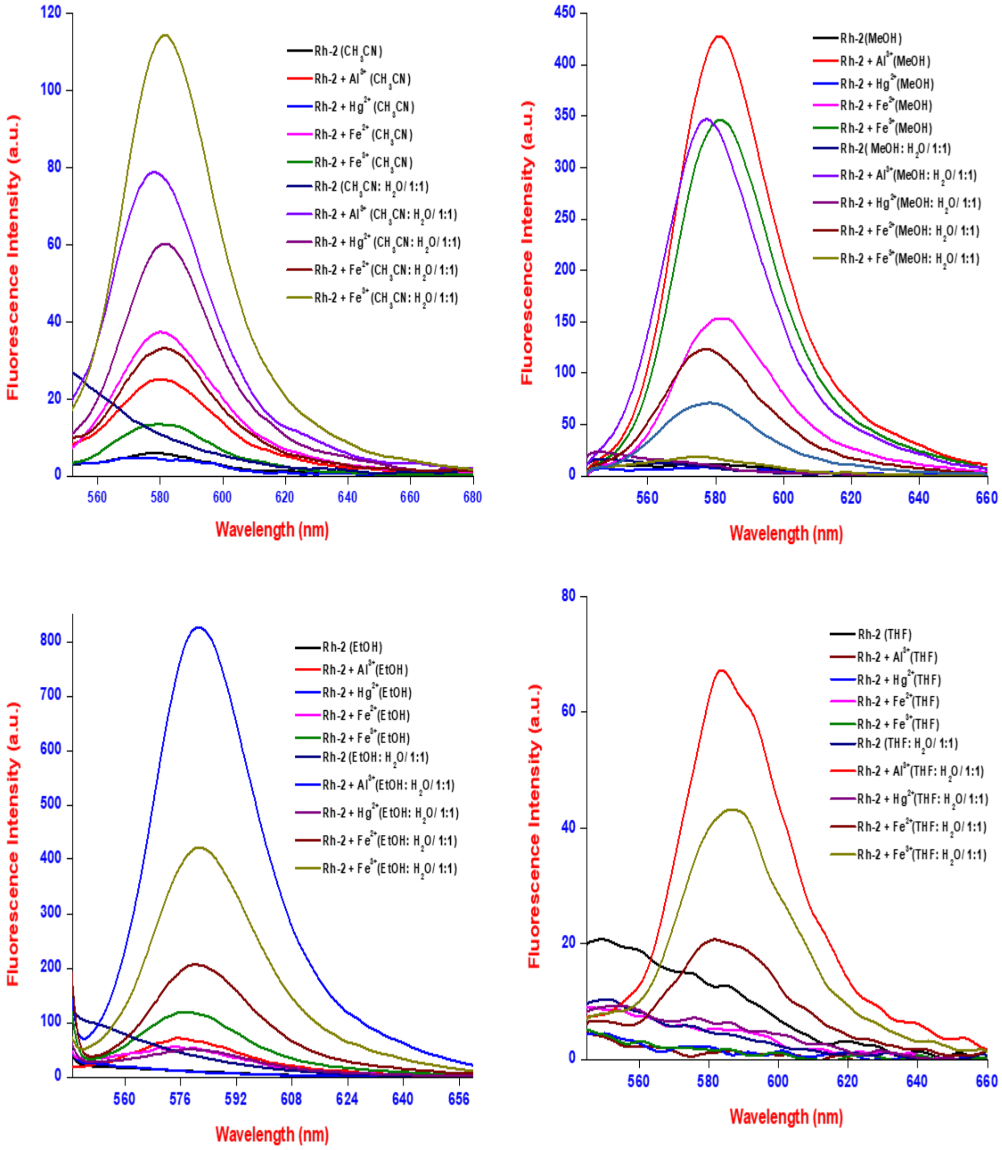

Appx. 28. Fluorescence spectra of Rh-2 / Rh-2-metals in a variety of solvent systems

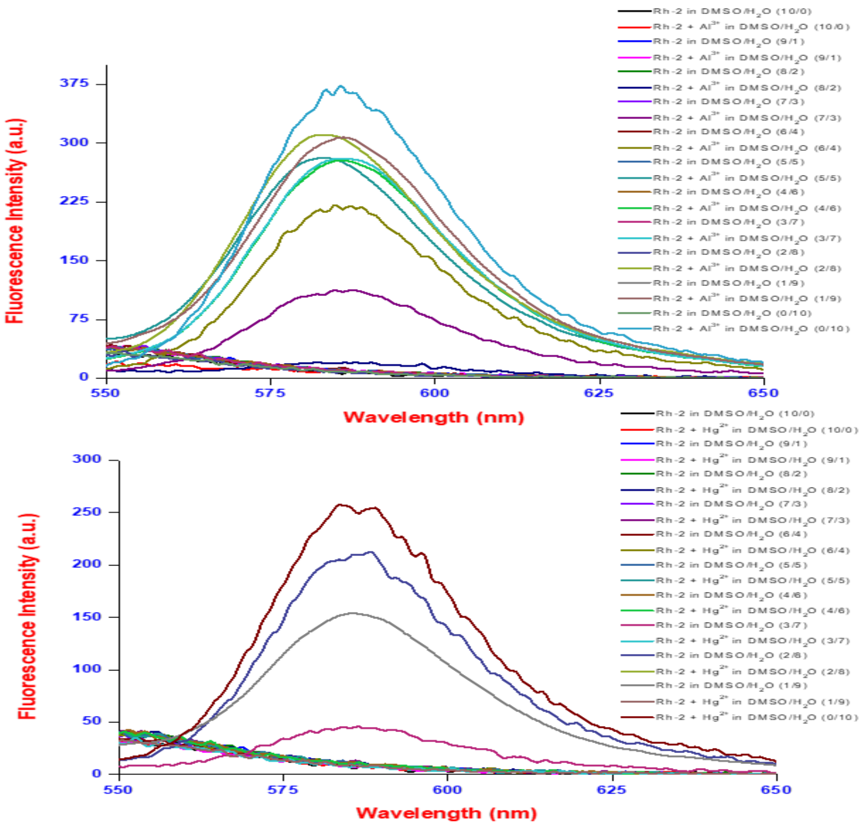

Appx. 29. Fluorescence spectra of Rh-2 / Rh-2-Al^{3+} and Rh-2 / Rh-2-Hg^{2+} in DMSO variety H_2O ratios

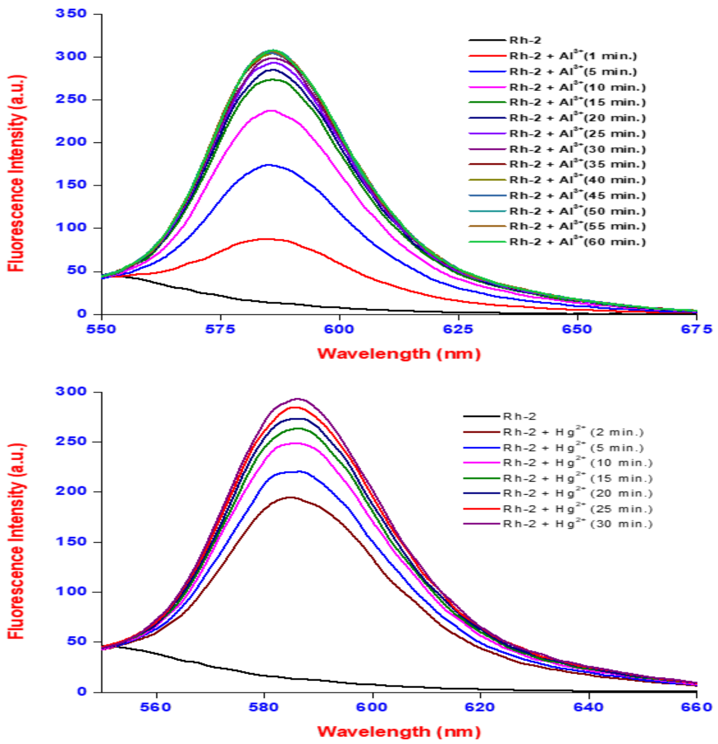

Appx. 30. The fluorescence enhances the profile of the addition of Al^{3+} and Hg^{2+} to Rh-2 in DMSO/Tris and DMSO/HEPES from 0 min. to 60 min.

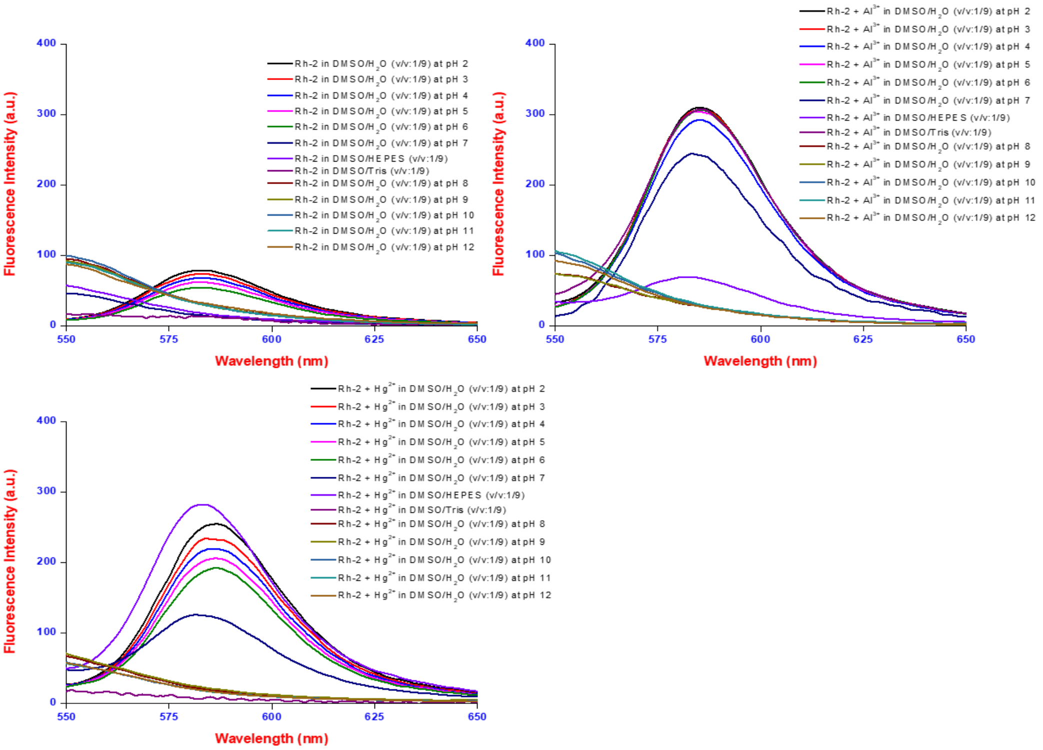

Appx. 31. The fluorescence spectra of Rh-2, Rh-2-Al^{3+}, and Rh-2-Rh-Hg^{2+} at different pH (2–12) in H_2O, the pH was modulated by adding HCl or NaOH solution.

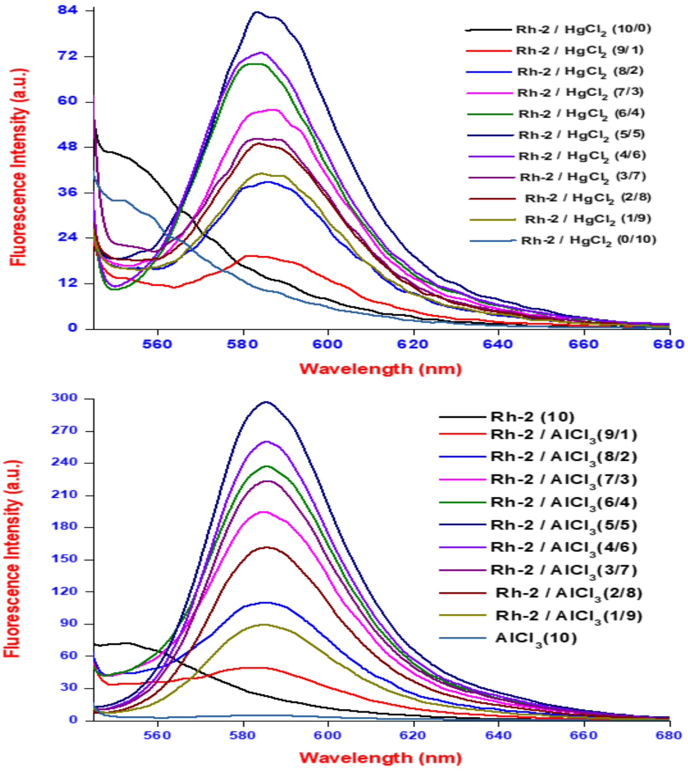

Appx. 32. The Job's plot fluorescence spectra of Rh-2 with Hg^{2+} (in DMSO/HEPES, v/v:1/9) and Al^{3+} (in DMSO/Tris, v/v:1/9)

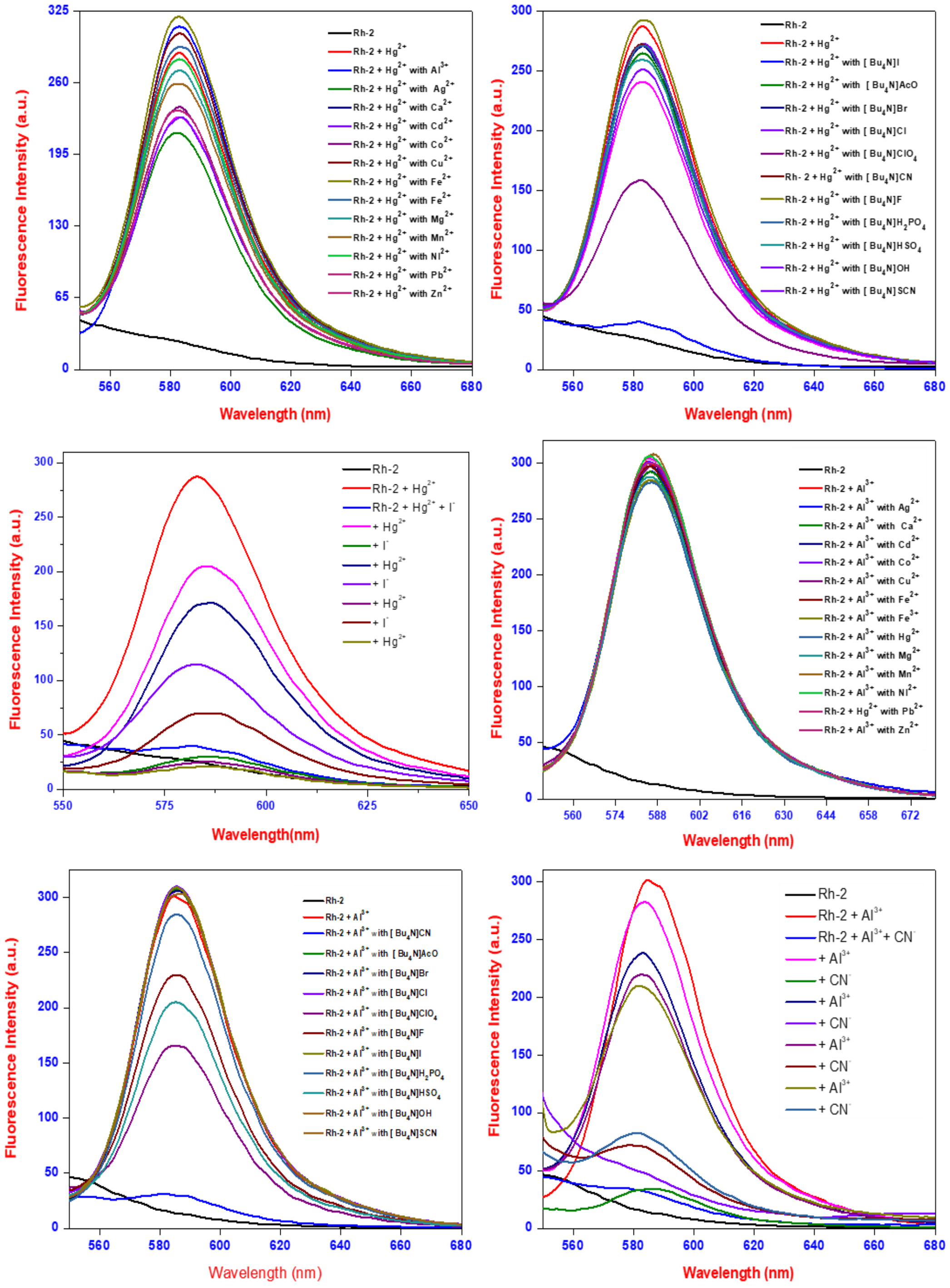

Appx. 33. Fluorescence spectra of Rh-2 in the presence of Hg^{2+}/Al^{3+} upon the addition of different ions, and reversible switching of the fluorescence spectrum of Rh-2 upon alternate addition of Hg^{2+}/I^{-} or Al^{3+}/CN^{-}

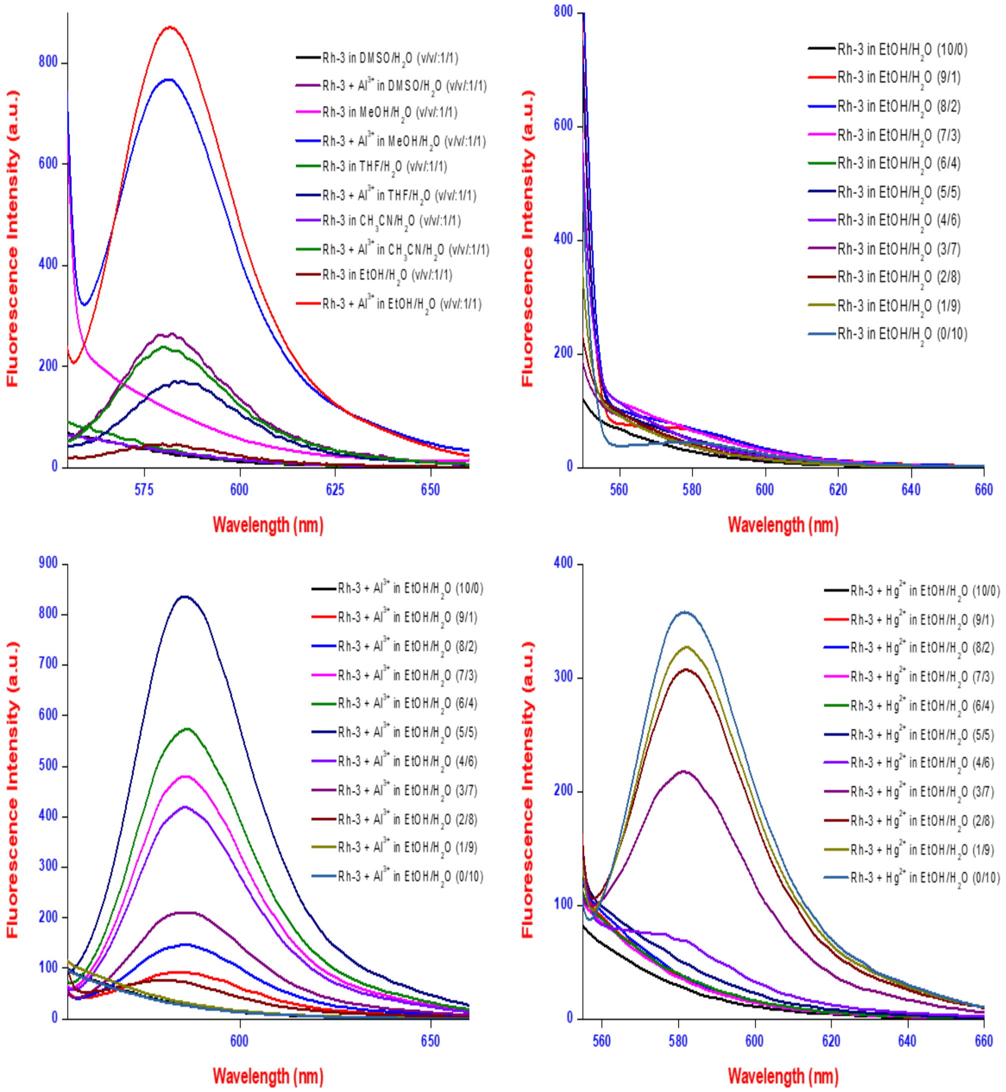

Appx. 34. Fluorescence spectra of Rh-3 / Rh-3-metals in a variety of solvent systems, and fluorescence spectra of Rh-3 / Rh-3-Al^{3+} and Rh-3 / Rh-3-Hg^{2+} in EtOH variety H_2O ratios.

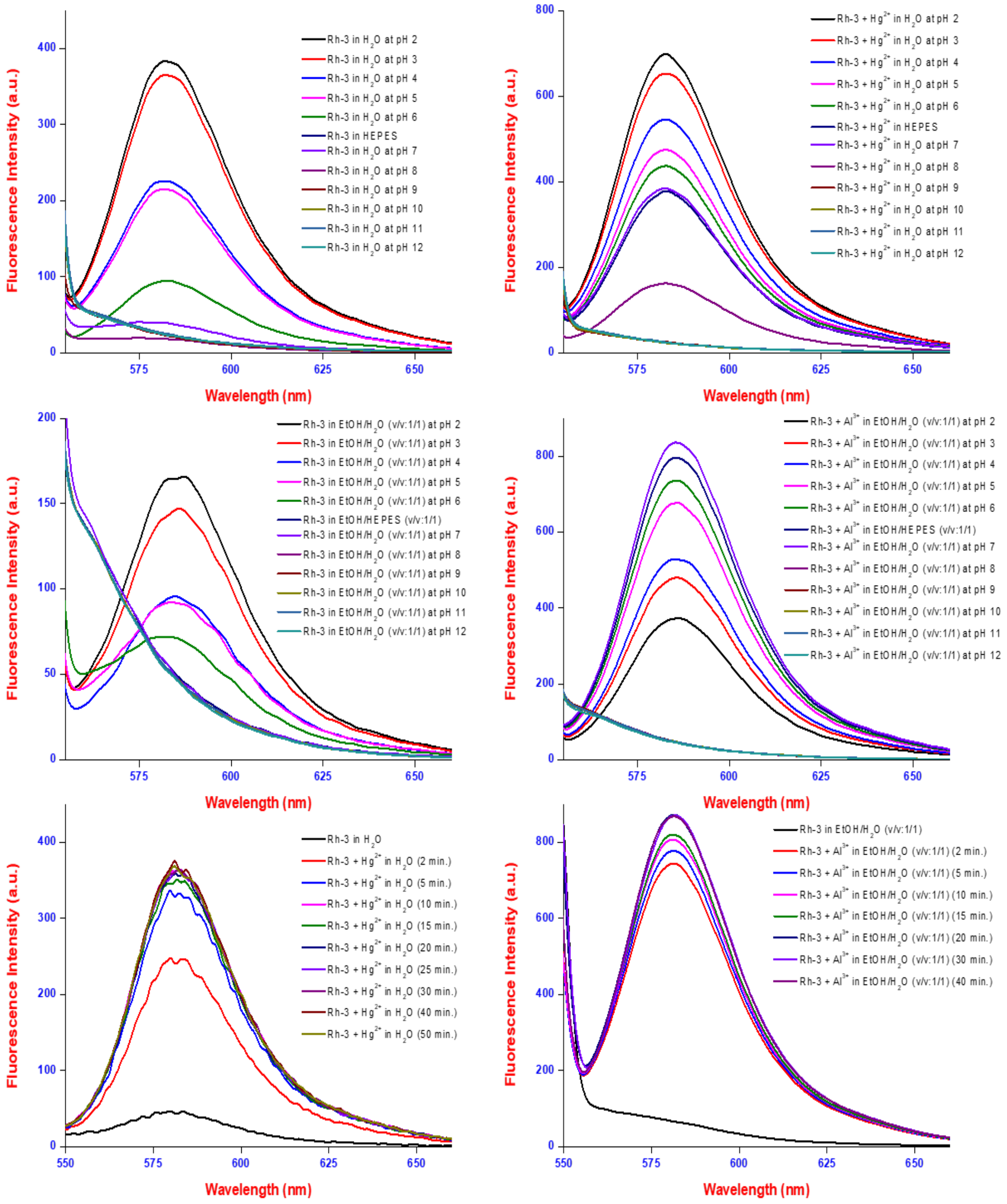

Appx. 35. The fluorescence spectra of Rh-3/Rh-3-Rh-Hg^{2+}/Rh-3-Al^{3+} at different pH (2–12), and the fluorescence enhances the profile of the addition of Hg^{2+}/Al^{3+} to Rh-3 from 0 min. to 60 min. in H_2O or EtOH/H_2O (v/v, 1/1)

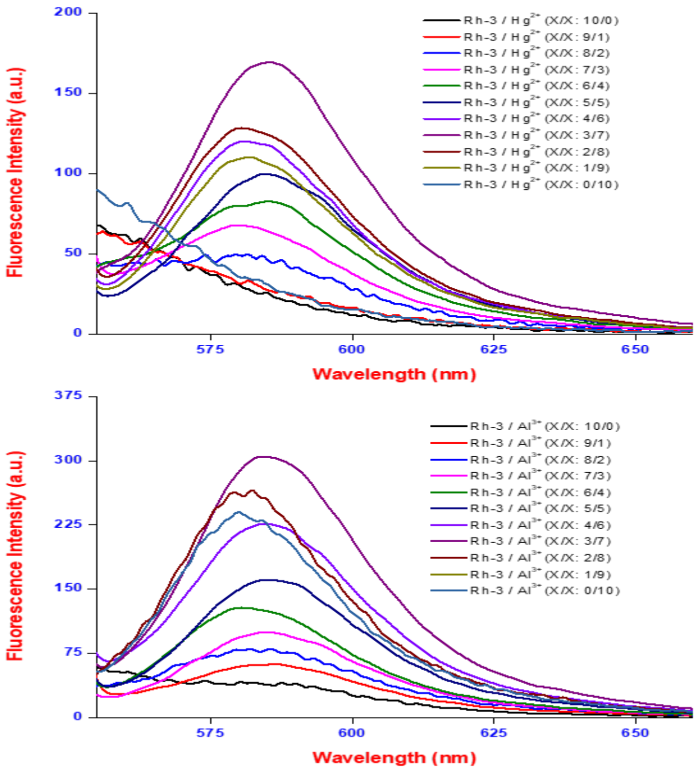

Appx. 36. The Job's plot fluorescence spectra of Rh-3 with Hg^{2+} (in H_2O) and Al^{3+} (in EtOH/H_2O, v/v:1/1)

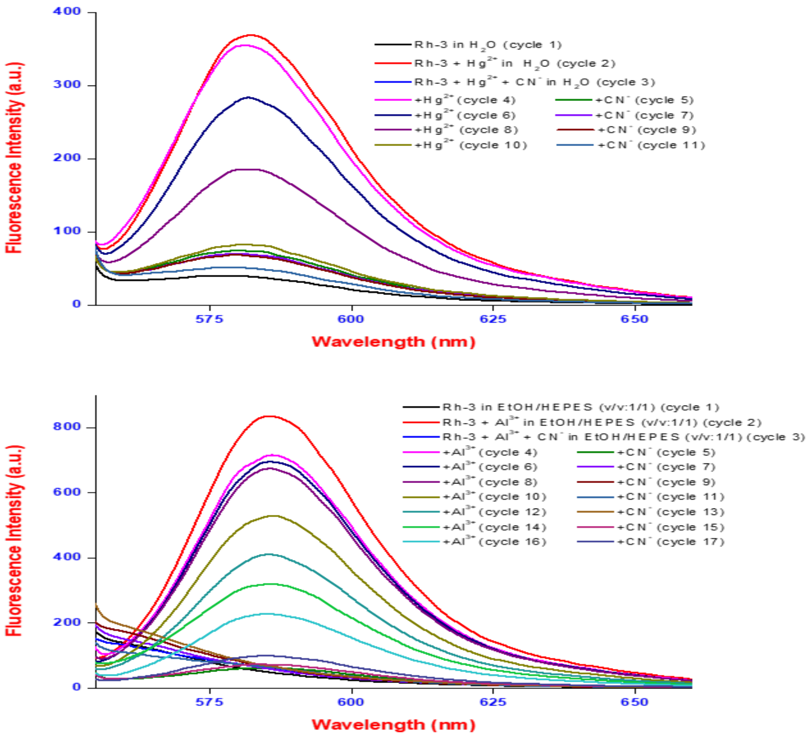

Appx. 37. Reversible switching of the fluorescence spectrum of Rh-3 upon alternate addition of Hg^{2+}/CN^{-} or Al^{3+}/CN^{-}

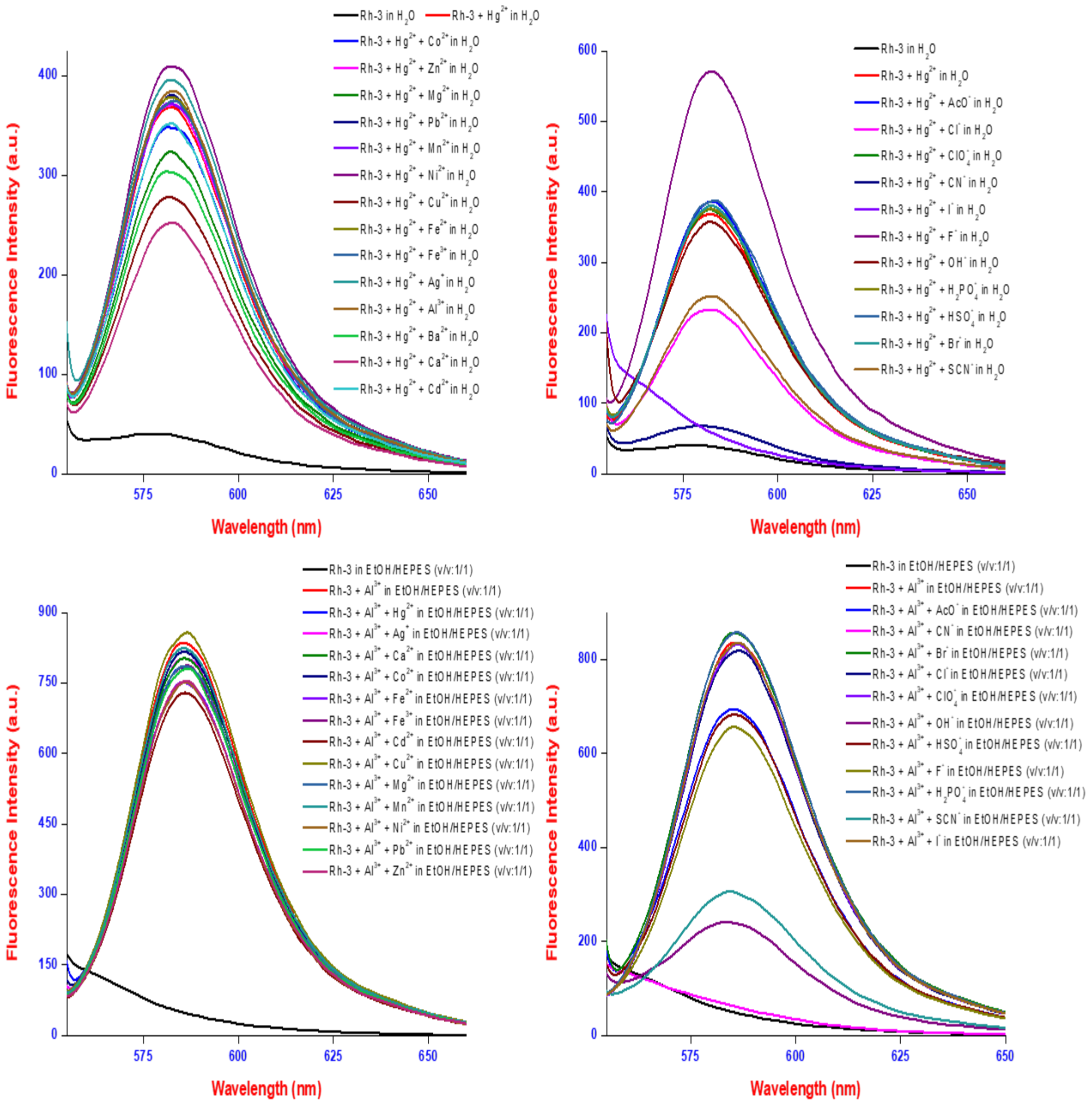

Appx. 38. Fluorescence spectra of Rh-3 in the presence of Hg^{2+}/Al^{3+} upon the addition of different ions